Rotational Seismology and Its Applications in Microseismic Event
Localization

by

Zhenhua Li

A thesis submitted in partial fulfillment of the requirements for the degree of

Doctor of Philosophy

in

Geophysics

Department of Physics

University of Alberta

Abstract

Theory indicates that, to fully describe the ground motions of a particle, translational motions, strain and rigid rotational motions are all needed, where the first includes particle displacement, velocity and/or acceleration and the second includes normal and shear strain. Traditional seismology is based on the measurement of only translational motions and strain whereas rigid rotational motions have been ignored for a long time. This is because current inertial seismic sensors, such as geophones and seismometers, are only sensitive to translational motions and strain; rotational sensors with enough sensitivity are not widely available. The recent development of rotational sensors makes the combined analysis involving all three types of motions possible. The main contribution from rotational motions is that they directly provide information about the spatial gradients of wavefields, which have been used by geophysicists to improve current geophysical techniques, such as wavefield separation, reconstruction, ground roll removal and moment tensor inversion. In this thesis, we investigate the possibility of involving spatial gradient information in waveform based microseismic event localizations.

Microseismic event localization, as an essential task of microseismic monitoring, can provide important information about underground rock deformation during hydraulic fracturing treatments. Microseismic event localization using time reversal extrapolation is one of the most powerful waveform based localization methods that back-propagates seismic recordings to source locations and avoids the need of picking individual first arrivals. The latter could be challenging for data with a low signal-to-noise ratio (SNR), such as the one obtained during microseismic monitoring, whereas time-reversal extrapo-

lation can enhance the SNR of source images through stacking. In this thesis, we propose two new representation theorem based time-reversal extrapolation schemes such that wavefields and their spatial gradients are jointly analyzed for an improved microseismic source image, namely acoustic and elastic approaches. Pressure wavefields and particle velocities correspond to wavefields and spatial gradients in the acoustic scheme and likewise, particle velocities and rotational rate wavefields in the elastic scheme. With newly proposed focusing criteria, the source location and origin time of a microseismic event are determined automatically.

However, all time-reversal extrapolation schemes suffer from high computational costs because this technique is based on solving discrete two-way wave equations using the finite difference or finite element method. We propose a reduced-order time-reversal extrapolation scheme using proper orthogonal decomposition which can be used for the real-time microseismic event localization.

Preface

This dissertation is submitted for the degree of Doctor of Philosophy in Geophysics at the University of Alberta. The research described herein is original, and neither this nor any substantially similar dissertation was or is being submitted for any other degree or other qualification at any other university.

A version of **chapter 2** has been published as Li, Z. and van der Baan, M., 2017, Tutorial on rotational seismology and its applications in exploration geophysics, Geophysics, 82(5), W17-W30,doi: 10.1190/geo2016-0497.1. I was responsible for code development, data analysis, figure preparation and manuscript writing.

A version of **chapter 3** has been published as Li, Z. and van der Baan, M., 2016, Microseismic event localization by acoustic time reversal extrapolation, Geophysics, 81(3), KS123-KS134, doi: 10.1190/geo2015-0300.1. I was responsible for code development, data analysis, figure preparation and manuscript writing.

A version of **chapter 4** has been accepted as Li, Z. and van der Baan, M., 2017, Elastic passive source localization using rotational motion, Geophysical Journal International. I was responsible for code development, data analysis, figure preparation and manuscript writing.

Acknowledgements

Foremost, I would like to express my sincere gratitude to my supervisor Dr. Mirko van der Baan for his continuous support throughout my PhD study and research with his patience and immense knowledge. He could always make difficult concepts easy to follow which helped me significantly in obtaining a solid understanding of the problems quickly. And his positive motivation and enthusiasm has strongly encouraged me to take geophysical research as my life-time career.

I would also like to thank my co-supervisor, Dr. Mathieu Dumberry, who supported me through mathematical perspective.

I would like to thank my parents, Yuejin Li and Yanfen Wang and my wife, Siwen Wei, who gave me their strongest moral support throughout the past five years, without whom I would never finish my PhD.

Special thanks to the members of my supervisory and candidacy committee for their insights and feedback: Dr. Lawrence H. T. Le, Dr. Bruce R. Sutherland and Dr. Mauricio D. Sacchi.

I would also like to thank my colleagues and friends at the University of Alberta for their direct or indirect supports and in particular all the students and staff of the Microseismic Industry Consortium.

For Chapter 2, I would like to thank Everhard Muyzert, David Aldridge, Shuki Ronen for their great suggestions. In addition, we would like to thank Jim Gaiser for his discussion on VSP applications, David Aldridge for permission to reproduce his AVO results, Stefanie Donner for discussions on moment tensor inversion and Robert Brune for many comments and suggestions in the process of publishing chapter 2, as well as reviewers Heiner Igel, Ohad Barak,

Contents

List of Tables

List of Figures

xiii

xiv

List of Abbreviations

1D	One-dimensional
2D	Two-dimensional
3D	Three-dimensional
3-C	three-component
ARQRd	Adaptive randomized QR decomposition
AVO	Amplitude versus offset
$f - k$	Frequency-wavenumber
PDE	Partial differential equation
POD	Proper orthogonal decomposition
QRd	QR decomposition
SNR	Signal-to-noise ratio
SVD	Singular value decomposition
VSP	Vertical seismic profile

Chapter 1

Introduction

1.1 Background

Microseismic monitoring involves the acquisition of continuous seismic data for the purpose of locating and characterizing seismic activity induced by human activities, such as mining and hydraulic fracturing (Van der Baan et al., 2013). In the mining industry, microseismicity is often acquired to monitor in-situ stress changes around tunnel walls, preventing possible explosive rock failure (Maxwell, 2009). The most common application of this technology in the hydrocarbon industry is to monitor hydraulic fracturing treatments for increasing oil and gas production. During this process, high pressure fluid is injected into a treatment well (Figure 1.1). When the effective pressures overcome the rock strength, cracks are created in the formation, leading to microseismic emissions. Sensors are deployed in the borehole or on the surface (Figure 1.1) to detect resulting wave motion. Accurate microseismic event locations aid in understanding reservoir development, estimating simulated rock volumes and determining future drainage strategies (Maxwell, 2009).

In this thesis, we introduce an event localization technique based on the representation theorem involving a new type of measurements - rotational motion.

1
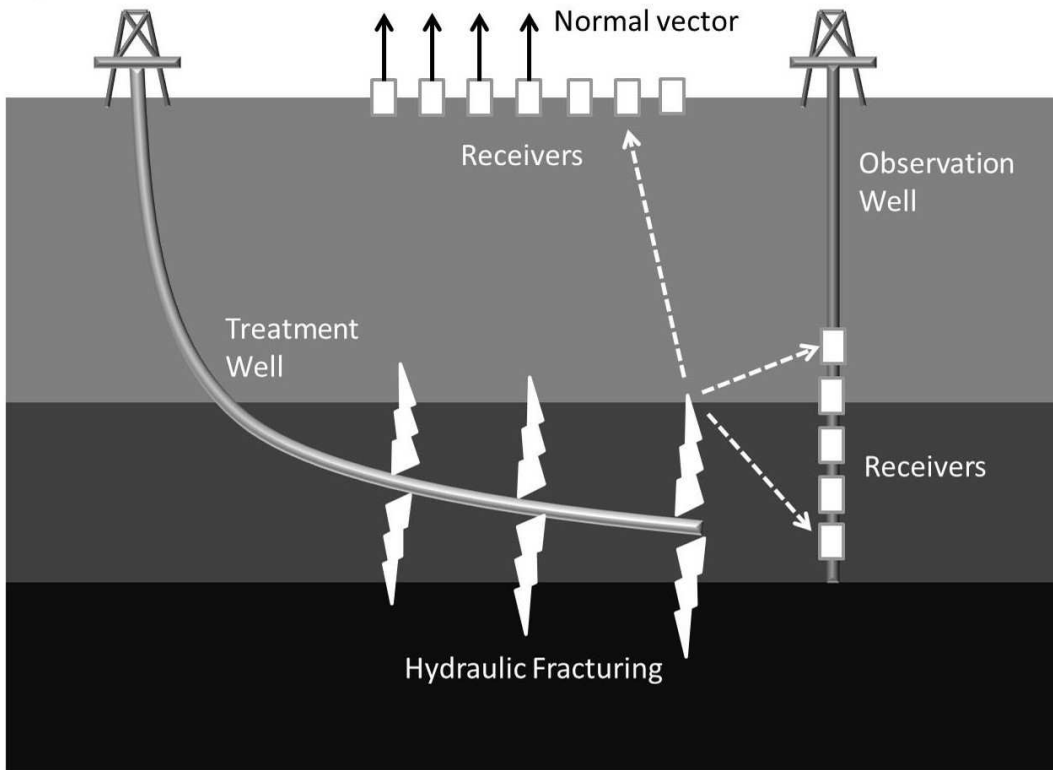
Figure 1.1: Sideview of the hydraulic fracturing process. High pressure fluid is injected through a treatment well, creating fractures in the surrounding rock. Emitted microseismic waves (white dashed lines) are recorded by receivers (white squares) on the surface and/or in the observation well. Observed waveforms are used to locate the microseismic events. The surface array has its normal vector pointing upward to the sky.

1.1.1 Rotational seismology

In classic seismology, for a solid body, general motion of particles is divided into three kinds: translational motion (along x, y, z axis), rotational motion (around x, y, z axis) and deformation (Bath, 1979, Lee et al., 2009a).

Rotational seismology is concerned with measuring and analyzing rotational particle motion. Such motion has been ignored for a long time, with a widespread belief that rotational motions are insignificant and negligible (Richter, 1958, Lee et al., 2009a). Also there is a lack of instruments with required sensitivity.

Recently, new instruments have been developed that directly measure the rotational motion in vertical and horizontal directions. Those measurements indicate that, for far field earthquakes with small ground deformation, observed rotational motion agrees well with simulated results (Igel et al., 2007, Suryanto et al., 2006),while for near field or strong earthquakes (Takeo, 1998), observed rotational motion is one or two orders of magnitude larger than the theoretical expectation.

In other words, rotational motion is not only significant but can also aid in our understanding of the earth. Moreover, measurements from rotational instruments agree with predictions of rotational motion from arrays of translational instruments, providing confidence in both the rotational instruments and the theoretical predictions (Huang, 2003, Lee et al., 2009a).

The potential of rotational seismology has been realized gradually by engineers and geophysicists. Much research points to the necessity of recording rotational motion of particles (Aki and Richards, 2002). Takeo and Ito (1997) estimate the rotational strain tensor and the spatial variation of slip velocity through observed rotational ground motion. These quantities will be large when there are spatially rapid changes caused by slip on the fault and/or the generation of fractures. Graizer (2005) point out that rotational ground motion should be recorded in order to reduce its possible contamination to signals recorded by horizontal components of traditional 3-component sensors in strong or near-field earthquakes. Otherwise, it will result in long period errors, especially for residual displacement calculation. Pham et al. (2009) show that P-SH scattering could explain observed rotational motion in P-wave coda which in

turn could be used to constrain crustal scattering properties.

Moreover, the importance of rotational seismology also attracts the attention of the oil and gas industry. I give a detailed review of rotational seismology and several possible applications in **chapter 2**.

1.1.2 Methods for Microseismic event localization

Broadly speaking, microseismic event localization methods are categorized into two types: travel-time based and waveform-migration based methods. Travel-time based event localization methods were most commonly applied to locate the hypocenter and the origin time of an earthquake in global seismology, including grid search (Aldridge et al., 2003) and double difference approaches (Zhang and Thurber, 2003,Castellanos and Van der Baan, 2013), in which either P- or S-wave arrivals or both are picked before further processing. However, event picking can often be a challenging and time-consuming task for low quality data (Artman et al., 2010). Both mispicks and missing picks negatively influence event locations (Kocon and Van der Baan, 2012, Castellanos and Van der Baan, 2013, Castellanos and Van der Baan, 2015). However, due to its fast calculation speed and easy implementation, these type of methods are widely used for microseismic event localization.

Migration based methods

Migration based methods avoid arrival time picking, possibly rendering them more suitable for low signal-to-noise ratio data (Artman et al., 2010).

Emission tomography is one of the simplest forms, in which travel-time tables are created for each possible grid location. A semblance analysis over the forward predicted travel-times then yields potential microseismic event locations (Duncan and Eisner, 2010). In this method, a 3D grid volume is created in which each grid represents a possible microseismic event location. Then time shifts that correspond to the travel time from each possible location to all receivers are applied to the microseismic records followed by semblance analysis of the time-shifted microseismic records. The grid point with the highest semblance energy can be considered as the most likely possible event location

(Duncan et al., 2008, Duncan and Eisner, 2010, Chambers and Kendall, 2008).

An alternative approach is called time-reversal extrapolation (Fink et al., 2000). Reverse time extrapolation has been applied for earthquake source imaging (McMechan, 1983, McMechan, 1985). This method is similar to reverse time migration (RTM) (McMechan, 1983, Whitmore, 1983, Baysal et al., 1983). In traditional RTM, the receiver-side particle displacement (or particle velocity) wavefield is injected into a smoothed velocity model, followed by application of an imaging condition. The smoothed velocity model effectively removes reflections during backpropagation which may cause artifacts in images. RTM has been used for earthquake fault imaging (McMechan, 1985), thus showing promise for determining event hypocenters.

For microseismic event localization, it is the same procedure but with reflection data replaced by transmission data. This procedure can be described under the framework of the adjoint-state method, where it turns into a minimization problem (Fleury and Vasconcelos, 2013, Tarantola, 1984). A least-square misfit function $\boldsymbol{J}$, defined as

$$\boldsymbol{J} = ||\boldsymbol{d}(\boldsymbol{r}, \boldsymbol{r}^s, t, t_0) - \boldsymbol{d}^{rec}(\boldsymbol{r}, t)||^2 \tag{1.1}$$

is minimized by calculating the *Fréchet* derivatives with respect to the source parameters (Tarantola, 1984), i.e. the source location $\boldsymbol{r}^s$ and the origin time t_0, where in equation 1.1 $\boldsymbol{r}$ are the receiver locations, $\boldsymbol{d}$ is the simulated particle displacement fields given an estimated source location and an origin time, $\boldsymbol{d}^{rec}$ are the observed data, $|| \cdot ||^2$ is the L^2 norm. The recorded direct wavefield is seen as a perturbed wavefield $\delta\boldsymbol{d}$ due to a perturbation source $\delta\boldsymbol{S}(\boldsymbol{r}^s, t_0)$. To determine the perturbation source, the data misfit $|\boldsymbol{d}(\boldsymbol{r}, \boldsymbol{r}^s, t, t_0) - \boldsymbol{d}^{rec}(\boldsymbol{r}, t)|$ is back-propagated into the velocity model (Tarantola, 1984, Tromp et al., 2005), using

$$\boldsymbol{d}^\dagger(\boldsymbol{r}', t) = \oint G^\dagger(\boldsymbol{r}', \boldsymbol{r}, t) * S^\dagger d\boldsymbol{r} \tag{1.2}$$

where $\boldsymbol{d}^\dagger$ is the back-propagated particle displacement wavefield, $\boldsymbol{r}'$ is an arbitrary observation point on the back-propagation image, $G^\dagger$ is the adjoint of the particle displacement (velocity) Green's function from receivers at $\boldsymbol{r}$, $S^\dagger$ is

called the waveform adjoint source, representing the time-reversed data misfit. With an accurate velocity model, the back-propagated wavefield collapses at the source location. However, if only a particle displacement or velocity wavefield is used, artifacts will appear on the borehole back-propagation image.

In this thesis, I will introduce enhanced microseismic event localization methods using the spatial gradient of the wavefields through the acoustic and elastic representation theorems. Detailed derivation can be found in Chapter 3 and 4.

1.2   Motivation and contribution

Microseismic event localization is the most important task for microseismic monitoring. Accurate event locations directly reveal geometry and the propagation directions of stimulated fractures, which further provides valuable information about geomechanical processes during production. With this information, a better production strategy could possibly be determined for future usage. Most of the current localization methods merely use travel time information, obtained from P- and S-wave first arrival pickings. However, picking can be inaccurate especially when the SNR is too low that the arrivals can not be identified easily.

Moreover, waveforms of microsesimic data contain important information about the types and orientations of fractures, which necessitates the involvement of full waveforms in microseismic event localizations. Also, the semblance of microseismic recordings in migration process yields a higher SNR source image which may help in identifying microseismic events with small magnitudes. Time-reversal extrapolation has been proven to be a promising waveform-migration based method for locating earthquakes and microseismic events. Traditionally, only a single type of wavefield is used in this method which may still lead to biased source locations when the microseismic data have very low SNR.

Representation theorems indicate that both particle velocities/displacements and their spatial gradients should be used for more accurate event locations. In the acoustic case, wavefields are pressure and the spatial gradients are related

6

to particle velocities, whereas in the elastic case, wavefields are particle velocities and the spatial gradient are related to rotational motion. So in this thesis, we investigate enhanced time-reversal extrapolation based on representation theorems.

The main contributions of this thesis can be summarized as:

• introduce the basic theory of rotational seismology and several possible applications in the field of exploration geophysics.

• derive time-reversal extrapolation using acoustic and elastic representation theorems for microseismic event localization.

• propose two focusing criteria based on the Hough transform and energy flux to automatically determine event locations and origin times.

• propose a time-reversal extrapolation scheme based on the model order reduction technique to greatly speed up calculations in the field with the aim of obtaining event locations in real time.

1.3   Thesis structure

Chapter 2   introduces the basic theory of rotational seismology, including its mathematical description and physical meaning, followed by an introduction of current instruments that may be suitable for exploration purpose. Theory and measurements show that rotational rate recordings can provide information about the spatial gradient of particle velocities which is usually not included in exploration geophysics. Then several applications are discussed to illustrate that the combination of the wavefields and their spatial gradients could improve current seismic processing methods.

Chapter 3   derives a time reversal extrapolation scheme based on an acoustic representation theorem which combines the pressure field and its spatial gradient for microseismic event localization. The chapter also provides a theoretical proof that the proposed method can remove ghost focuses which normally exist if only a single type of data is used. Then a focusing criterion based on the Hough transform is proposed to evaluate the magnitude of the back-propagated source image in order to automatically determine the loca-

tion and origin time of each microseismic event. Two examples are shown to illustrate the good performance of the proposed method.

Chapter 4 is the extension of **chapter 3** to the elastic case. We first derive a general elastic representation theorem using the second-order wave equations in a homogeneous medium. An elastic time-reversal extrapolation scheme is constructed based on the theorem which combines both particle velocities and rotational motions. With the new scheme, P- and S-waves can be back-propagated into the medium separately. We choose to simply back-propagate S-wave recordings since S-waves are usually dominant in microseismic monitoring. We also propose an improved focusing criterion that evaluates the energy flux of the back-propagated source image, with which the locations and origin time are determined.

Chapter 5 introduces a real-time time-reversal extrapolation scheme based on model order reduction. To perform this scheme, high fidelity simulation is done first with a pre-defined velocity model and all resulting wavefields are vectorized and saved into a large matrix. An adaptive randomized QR decomposition is applied to the matrix to get an orthonormal basis which is used to construct an order-reduced system. The system is small enough to run in real-time, such that a complete work flow is proposed for continuous microseismic event localization.

Chapter 6 presents the concluding remarks of this research thesis.

Chapter 2

Tutorial on rotational seismology and its applications in exploration geophysics [1]

Traditionally, seismological interpretations are based on the measurement of only translational motions, such as particle displacement, velocity and/or acceleration, possibly combined with pressure changes; yet theory indicates that rotational motions should also be observed for a complete description of all ground motions. The recent and ongoing development of rotational sensors renders a full analysis of both translational and rotational ground motion possible.

In this tutorial, we first explain the basic mathematical theory related to rotational motion. And then we briefly introduce several instruments used to directly measure the rotational ground motion which may be applicable for exploration geophysics. Finally, several applications of rotational motion in exploration geophysics are introduced, namely 1) P- and S-wavefield separation, 2) wavefield reconstruction, 3) ground roll removal, 4) microseismic event localization and reflection seismic migration by wavefield extrapolation, and 5)

---

moment tensor inversion. The cited research shows that in particular the information on the spatial gradient of the wavefield obtained by rotational sensors is beneficial for many purposes. This tutorial is meant to (1) enhance familiarity with the concept of rotational seismology, (2) lead to additional applications and (3) fast track the continued development of rotational sensors for both global and exploration geophysical usage.

2.1 Introduction

In classical linear elastic theory, general motion of solid particles is divided into three kinds (Figure 2.1): pure translational motion (along x, y, z axis), rigid rotational motion (around x, y, z axis) and deformation (Bath, 1979, Aki and Richards, 2002, Lee et al., 2009b). Pure translational motion and rigid rotational motion are only related to the relative change in the position of solid particles, whereas deformation implies relative change in the shape of solid particles. Deformation is also known as strain in classic seismology, including volumetric/normal strain and symmetric shear strain; strain is the most fundamental component in the elastic wave equation. Particle motion includes 12 degrees of freedom, including 6 degrees of strain, 3 degrees of pure translations and 3 degrees of pure rotations. Traditional exploration seismology studies pure translational motion and deformation measured by three-component (3-C) particle displacement (velocity) sensors (geophones) and/or pressure changes with hydrophones.

In this tutorial we will use the term 'particle displacement(velocity)' sensors for the traditional sensors such as geophones and seismometers following Barak et al. (2014), instead of the term translational sensors as used by Igel et al. (2015) to differentiate this type of sensor from rotational ones. The term 'particle displacement(velocity)' sensor refers to geophones and such which measure both translational motion and deformation (strain) around a point, whereas the term 'translational' sensor implies only constant shifts in positions are captured.

The rotational motion has been theoretically discussed since the 1950s (Lee et al., 2009b). However, not until recently has such motion been measured by
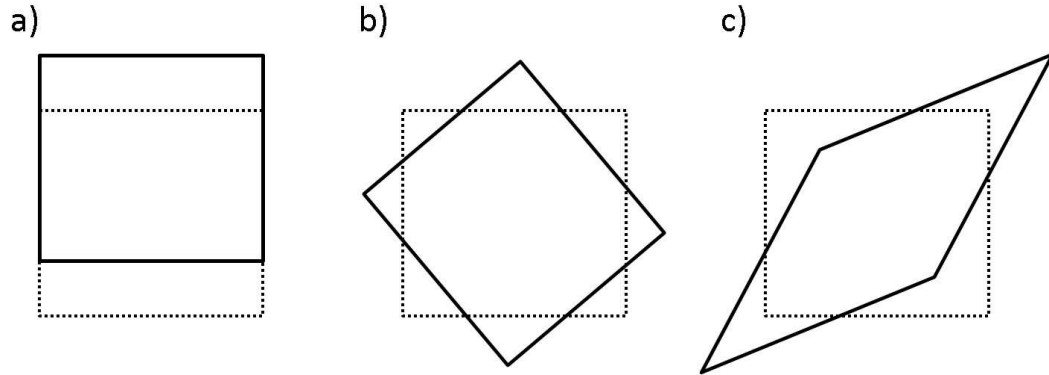
Figure 2.1: Three types of motions for solid particles in classic elasticity. a) translational motion; b) rigid rotational motion; c) deformation. Dots: Original body; solid line: new body shape. Only a) translational motion and c) deformation are detected by current three-component particle displacement(velocity) sensors whereas b) rigid rotational motion is ignored.

earthquake seismologists due to the lack of rotational sensors with sufficient sensitivity and bandwidth for geophysical usage (Lee et al., 2009b). Rotational sensors have existed for at least three decades; yet their development for geophysical applications has been intensified since ring laser gyroscopes first directly measured rotational ground motion from teleseisms (Mcleod et al., 1998; Pancha et al., 2000; Igel et al., 2005; Schreiber et al., 2006; Dunn et al., 2009; Schreiber et al., 2009a). We will describe various existing and proposed sensors in the following sections.

In this tutorial, we introduce the concept of rotational motion and possible applications for exploration geophysics. Complementary articles can be found in the special issue on Rotational Seismology and Engineering Applications of the Bulletin of the Seismological Society of America in May 2009 (Lee et al., 2009b) and the special issue on Advances in rotational seismology: instrumentation, theory, observations and engineering of Journal of Seismology in October 2012. A more general review in the fields of global seismology and engineering applications is by Igel et al. (2015).

2.2   Rotational Motion

In classical infinitesimal elasticity, to completely describe particle motion, we need translational motion, strain deformation and rigid rotation (Van Driel et al., 2012). The spatial gradient of particle velocity is composed of strain deformation and rigid rotation, representing particle deformation. Traditional three-component displacement receivers can only measure translational motion and strain deformation along three orthogonal directions. Rigid rotation has been ignored for a long time (Lee et al., 2009a). Recently, the development of new instruments provides an opportunity to directly record and study the rigid rotational rate in vertical and horizontal directions (Lee et al., 2012). Because rotational rate measurements also include information on the spatial gradient of particle velocity, it will aid in representation theorem based reverse time extrapolation.

Figure 2.2 illustrates the distortions of a random particle during deformation. In Figure 2.2, O is the origin. P is an arbitrary particle in the medium, and vector $\boldsymbol{r}$ shows the spatial position of P. Q is another particle quite close to P, whose spatial position is $\boldsymbol{r} + \boldsymbol{\delta r}$. $\boldsymbol{u}$ describes the displacement field. In our notation, bold symbols indicate vectors. After infinitesimal deformation, P' is the final position of P, expressed as $\boldsymbol{r} + \boldsymbol{u}(\boldsymbol{r})$, and Q' is the final position of Q, expressed as $\boldsymbol{r} + \boldsymbol{\delta r} + \boldsymbol{u}(\boldsymbol{r} + \boldsymbol{\delta r})$. $P'M$ is parallel to PQ, and there is an angle between $P'M$ and $P'Q'$, indicating a rotation occurs during the deformation. Any distortion is liable to change the relative end position of line-element $\boldsymbol{\delta r}$ (Aki and Richards, 2002). If this change is $\boldsymbol{\delta r}$, we express the deformation using their end point P' and Q' as follows,

$$\boldsymbol{\delta u} = \boldsymbol{u}(\boldsymbol{r} + \boldsymbol{\delta r}) - \boldsymbol{u}(\boldsymbol{r}). \tag{2.1}$$

Because $\boldsymbol{\delta r}$ is infinitesimal, we can expand $\boldsymbol{u}(\boldsymbol{r} + \boldsymbol{\delta r})$ as $\boldsymbol{u}(\boldsymbol{r}) + (\boldsymbol{\delta r} \cdot \boldsymbol{\nabla})\boldsymbol{u}$, where $\nabla = \frac{\partial}{\partial x}\mathbf{i} + \frac{\partial}{\partial \mathbf{z}}\mathbf{j}$ in the two dimensional case as in Figure 2.2, and $\mathbf{i}$ and $\mathbf{j}$ are orthogonal unit vectors. Then equation 2.1 can be simplified as $\boldsymbol{\delta u} \approx (\boldsymbol{\delta r} \cdot \boldsymbol{\nabla})\boldsymbol{u}$. Next, according to tensor calculus of continuum mechanics (Ganzales and Stuart, 2008), $(\boldsymbol{\delta r} \cdot \boldsymbol{\nabla})\boldsymbol{u}$ can be written as $\boldsymbol{\delta r} \cdot \boldsymbol{\epsilon} + \boldsymbol{\delta r} \cdot \boldsymbol{\Omega}$, where $\boldsymbol{\epsilon}$ and $\boldsymbol{\Omega}$ are the strain and rotation second order tensor respectively, and $\boldsymbol{\epsilon} = \frac{1}{2}(\boldsymbol{\nabla u} + (\boldsymbol{\nabla u})^T)$;
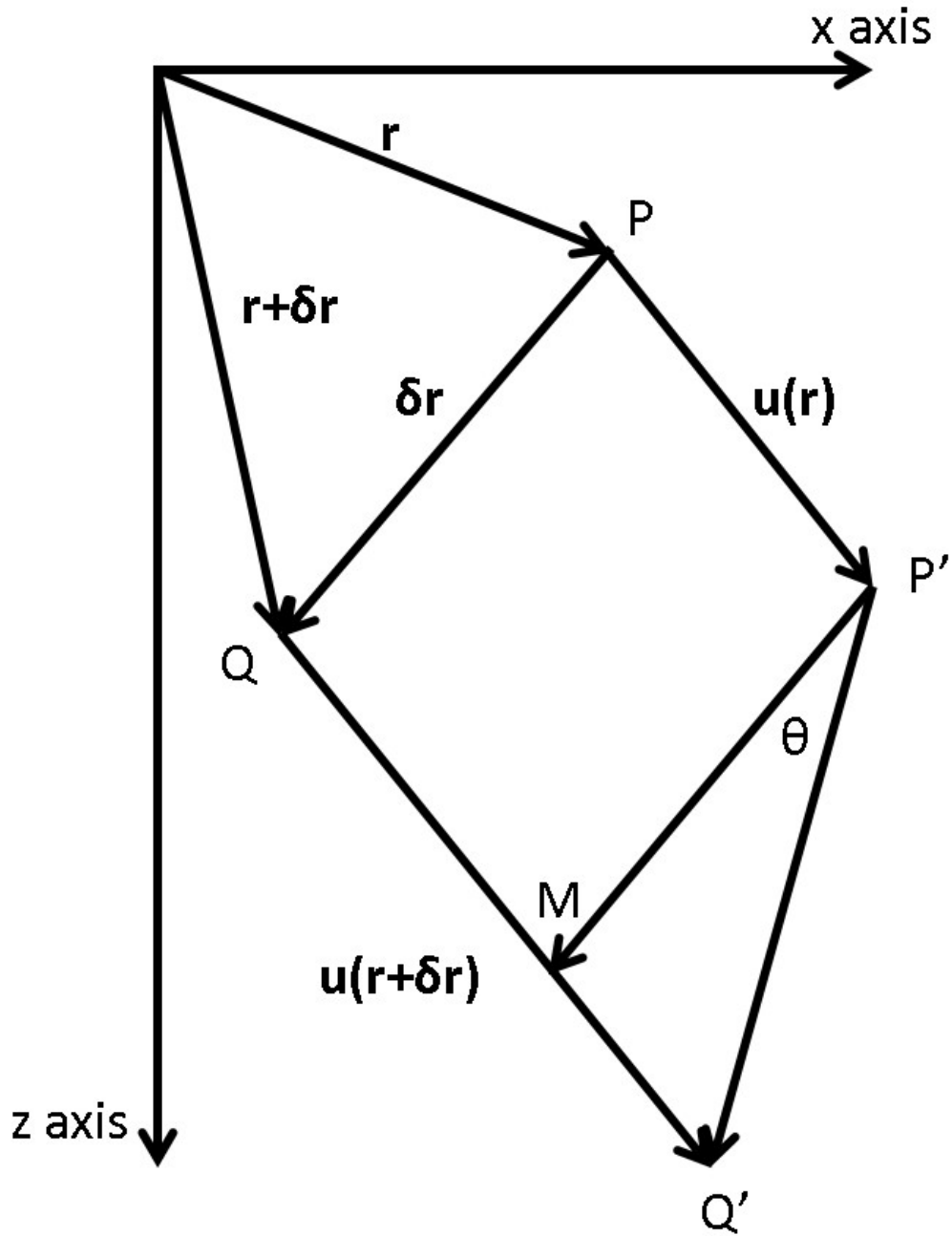
Figure 2.2: Displacement of particle boundary under the assumption of infinitesimal deformations. PQ shows the original status of a particle boundary denoted by $\boldsymbol{\delta r}$. $\boldsymbol{r}$ and $\boldsymbol{r} + \boldsymbol{\delta r}$ are coordinates of points P and Q. Point P goes to P' after deformation denoted by $u(r)$. Similarly, the deformation of Q is $\boldsymbol{u}(\boldsymbol{r} + \boldsymbol{\delta r})$. $P'Q'$ denotes new status after deformation. $P'M$ is parallel to PQ. θ represents the boundary rotation that exists during deformation.

$\boldsymbol{\Omega} = \frac{1}{2}(\boldsymbol{\nabla}\boldsymbol{u} - (\boldsymbol{\nabla}\boldsymbol{u})^T)$. Here we can see clearly the physical meaning of the deformational change, namely as a combination of strain and rotational motion.

The rotational motion of a particle can also be expressed by the curl of the particle displacement,

$$\boldsymbol{\Omega}(\boldsymbol{r},t) = \frac{1}{2}\boldsymbol{\nabla} \times \boldsymbol{u}(\boldsymbol{r},t). \tag{2.2}$$

By applying a time derivative to either side of equation 2.2, we obtain

$$\dot{\boldsymbol{\Omega}}(\boldsymbol{r},t) = \frac{1}{2}\boldsymbol{\nabla} \times \boldsymbol{v}(\boldsymbol{r},t), \tag{2.3}$$

where $\dot{\boldsymbol{\Omega}}(\boldsymbol{r},t)$ is the time derivative of $\boldsymbol{\Omega}(\boldsymbol{r},t)$, also called rotation rate, and $\boldsymbol{v}(\boldsymbol{r},t) = \partial\boldsymbol{u}(\boldsymbol{r},t)/\partial t$, which is the particle velocity vector. Equation 2.3 is important since most rotational instruments used today are measuring rotation rate instead of the rotation itself (Igel et al., 2007, Schreiber et al., 2006).

In Cartesian (x,y,z) coordinates, the components of the rotation vector in an unlimited medium are given by

$$\begin{aligned}
\Omega_x &= \frac{1}{2}\left(\frac{\partial u_z}{\partial y} - \frac{\partial u_y}{\partial z}\right), \\
\Omega_y &= \frac{1}{2}\left(\frac{\partial u_x}{\partial z} - \frac{\partial u_z}{\partial x}\right), \\
\Omega_z &= \frac{1}{2}\left(\frac{\partial u_y}{\partial x} - \frac{\partial u_x}{\partial y}\right).
\end{aligned} \tag{2.4}$$

Equation 2.4 also embodies the principle of array-derived rotational seismology, as the rotational motion can be computed from the spatial derivatives of the particle displacement/velocity wavefield (Suryanto et al., 2006). Analogous to equation 2.2 and 2.3, we can express the rotational motion rate $\dot{\boldsymbol{\Omega}}$ by simply replacing the particle displacement $\boldsymbol{u}$ with the particle velocity $\boldsymbol{v}$ in equation 2.4.

Next we consider plane P- and S-wave propagation in a two dimensional homogeneous isotropic elastic medium (Figure 2.3). When the P-wave arrives, the particle body $ABCD$ becomes $A'B'C'D'$ due to the wave motion. This change can be decomposed into two parts: horizontal displacement (pure translation)
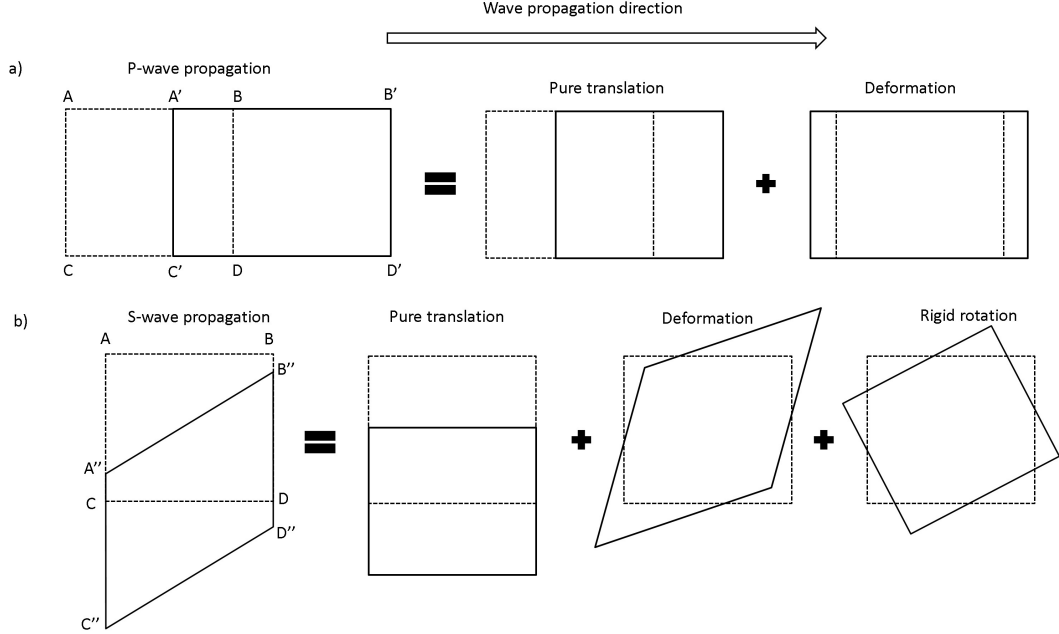
Figure 2.3:   Particle motion for horizontally propagating a) P-wave and b) S-wave. a) P-wave particle motion is composed of longitudinal (here horizontal) displacement (pure translation) and Extension (deformation). b) S-wave particle motion is composed of transversal (here vertical) displacement (pure translation), shear strain (deformation) and rigid rotation. Dots: Original shape of body; solid lines: New shape. Only S-waves generate rotations around a point.

and extension (deformation) (Figure 2.3a). No rigid rotation occurs for plane P-waves in homogeneous, isotropic media. When the S-wave passes, the particle body $ABCD$ becomes $A''B''C''D''$ due to the wave motion, which is composed of vertical displacement (pure translation), shear strain (deformation) and rigid rotation (Figure 2.3b).

Following the definition in Aldridge and Abbott (2009), the plane-harmonic-displacement wavefield $\boldsymbol{u}(\boldsymbol{r}, \boldsymbol{t})$ at position $\boldsymbol{r}$ and time t is generally written as

$$\boldsymbol{u}(\boldsymbol{r}, t) = u\boldsymbol{m}W(t - \frac{\boldsymbol{r} \cdot \boldsymbol{n}}{c}), \tag{2.5}$$

where u is a scalar displacement amplitude, $\boldsymbol{m}$ is the dimensionless unit polarization vector, W is the normalized waveform, with an absolute maximum amplitude of 1, normal $\boldsymbol{n}$ contains the propagation direction of the planar wave which travels with velocity c. The corresponding particle velocity vector $\boldsymbol{v}(\boldsymbol{r}, t)$

15

is

$$\boldsymbol{v}(\boldsymbol{r}, t) = u\boldsymbol{m}\dot{W}(t - \frac{\boldsymbol{r} \cdot \boldsymbol{n}}{c}), \tag{2.6}$$

where $\dot{W} = \frac{\partial W}{\partial t}$.

It follows that the rotation rate $\dot{\boldsymbol{\Omega}} = \frac{1}{2}\boldsymbol{\nabla} \times \boldsymbol{v}$ is given by

$$\dot{\boldsymbol{\Omega}}(\boldsymbol{r}, t) = -\frac{u}{2c}\boldsymbol{n} \times \boldsymbol{m}\dot{W}(t - \frac{\boldsymbol{r} \cdot \boldsymbol{n}}{c}). \tag{2.7}$$

The divergence $\nabla \cdot \boldsymbol{v}(\boldsymbol{r}, t)$ associated with the plane wave is

$$\nabla \cdot \boldsymbol{v}(\boldsymbol{r}, t) = -\frac{u}{c}\boldsymbol{n} \cdot \boldsymbol{m}\dot{W}(t - \frac{\boldsymbol{r} \cdot \boldsymbol{n}}{c}). \tag{2.8}$$

In a homogeneous medium, the propagation direction $\boldsymbol{n}$ of a P-wave is parallel to the polarization $\boldsymbol{m}$, so $\boldsymbol{m} = \pm\boldsymbol{n}$, and $c = v_p$, the P-wave velocity, which means P-waves are rotation free since $\boldsymbol{n} \times \boldsymbol{m} = \boldsymbol{0}$. For S-waves, the propagation direction $\boldsymbol{n}$ is perpendicular to the particle polarization $\boldsymbol{m}$, so $\boldsymbol{n} \cdot \boldsymbol{m} = \boldsymbol{0}$ and $c = v_s$, the S-wave velocity. In other words, for a homogeneous, isotropic, linear elastic medium, rotational motion is entirely embedded in S-waves, which are divergence free. These characteristics can help identify the type of incident elastic wave at position $\boldsymbol{r_R}$ in a homogeneous and isotropic medium (no free surface): (1) rotation rate = 0 and divergence $\neq 0 \Rightarrow$ incident P-wave; (2) rotation rate $\neq 0$ and divergence = 0 $\Rightarrow$ incident S-wave. This is important because theoretically translational motion is not detected by rotational sensors as shown next, indicating a natural separation between P- and S-waves in an isotropic, homogeneous medium. The separation of S and P waves also works in heterogeneous isotropic media.

We create a synthetic example to illustrate differences between particle displacement and rotational motion from a single point source consisting of a force applied in the x-direction. Synthetic sections are computed using a 2D staggered-grid finite difference algorithm (Pitarka, 1999). We use a homogeneous velocity model with a P- and S-wave velocity of respectively 5525m/s and 3320m/s. The source is a Ricker wavelet with a 30 Hz dominant frequency. Figure 2.4 is the snapshot of the x and z components of particle velocity as measured on conventional geophones as well as particle rotational rate at 0.2
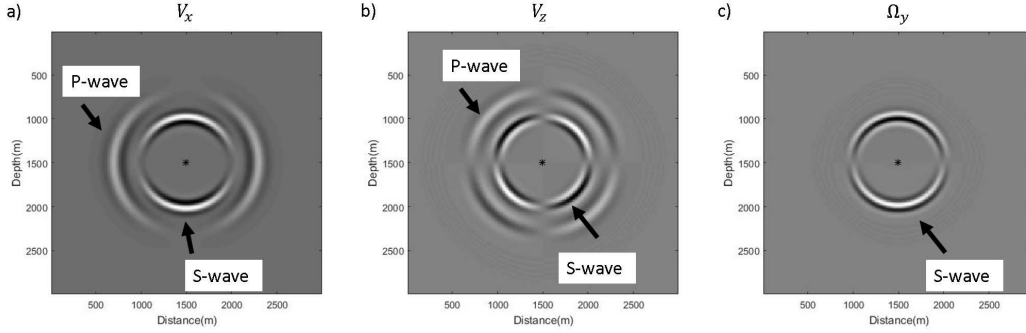
Figure 2.4: Wave propagations due to a single force in the x-direction in a homogeneous, isotropic medium. Snapshots at time = 0.2s for (a) x- and (b) z-components of particle velocity wavefields and (c) rotational rate wavefield along the y-direction. Star: source (point force in the x-direction). Both P- and S-wave are shown on a) and b), whereas only the S-wave is visible in c), indicating that displacement sensors record both P- and S-waves but rotational sensors are insensitive to P-waves in this medium.

second. We see both P- and S-waves in the particle velocity snapshots, whereas there are only S-waves in the rotational rates. The waveform differences between the particle velocity wavefields (Figure 2.4a,b) and the rotational rates (Figure 2.4c) reflect the fact that rotational motion incorporates information from the spatial gradients of the displacement wavefields.

The above example is mainly for conceptual illustration only. In reality, the underground medium always has properties of heterogeneity and/or anisotropy, which shows complex behavior in the generation of particle rotational motion (Pham et al., 2010; Van Driel et al., 2012). In general anisotropic P-waves generate rotational particle motions due to the non-orthogonality of the polarization direction $\boldsymbol{n}$ of quasi-P-wave (qP-wave) and the wave propagation direction $\boldsymbol{m}$ (Crampin, 1981; Pham et al., 2010). Moreover, rotational motion may also be associated with an incident P-wave due to strain-rotation coupling caused by strong near-surface heterogeneity and topography (Van Driel et al., 2012).

2.2.1 Rotation related to the free surface

Broadly speaking free-surface related rotational motions can be divided into those associated with surface waves and those due to incident and converted

17

body waves.

Surface waves

Surface waves include Love and Rayleigh waves. A Love wave in general is an SH wave type with particle motions perpendicular to the propagation direction in a horizontal plane. The particle motion of a Love wave often decrease rapidly with increasing depth. Love waves contribute to rotational motions around a vertical axis in spherically or stratified media.

Rayleigh wave motion needs additional clarification, because its particle motion is the superposition of elliptical motion and rigid-body rotational motion, the latter of which is ignored in the classical definition. For instance, when a Rayleigh wave impinges on a particle, it will cause the particle to both rotate (spin) around its center of mass due to particle deformation as well as orbit along an elliptical path around its original location (Shearer, 2009). It is the rigid-body rotation that is responsible for the horizontal components of recorded rotational motion, rather than the elliptical motion (Lin et al., 2011). We illustrate the differences between elliptical particle motion and rotational motion using a Ferris wheel analogy. Each cabin is orbiting along the red dotted circle without self-spinning (Figure 2.5). No rotational signal will be detected if we place a rotational sensor in the cabin; yet the cabins display elliptical motion since they circulate around a point. The motion of each spoke consists of two parts: self-rotation around its internal centre H and elliptical motion around the centre of the Ferris wheel O. Both motions have the same velocity. Self-rotation is characteristic of a rotational signal which will be detected if a rotational sensor is attached to the spoke. For example, the motion of the spoke OB may be interpreted as an elliptical motion of angle θ_1 around centre O followed by a self-rotation of angle θ_2 around internal centre H, where θ_1 equals θ_2.

It has been shown that, in case of strong or near-field earthquakes, particle displacement measurements from three-component seismometers may be contaminated by rotational motion, in particular tilt, linked to surface waves (Igel et al., 2005; Lin et al., 2011) which must be removed, prior to judicious analysis. In exploration geophysical applications, tilt and rotational contamination

of displacement measurements is unlikely to be an issue; yet measurement of rotational motion associated with surface waves may facilitate ground roll removal, as will be shown later.

Body waves

Rotational motion can also be caused by both P- and S-waves impinging and then converting at the free surface. Here we give a simple derivation of rotational motion generated by an incident plane P- or S-wave near the elastic free surface. This is important for seismic interpretation. As shown in figure 2.6a, PP and PS conversions exist on the free surface in the incident P-wave scenario. An arbitrary particle A is right below the free surface where the up-going and down-going plane waves interfere. Then the complete particle velocity of particle A is a combination of both the up- and down-going plane P-waves and the down-going converted S-wave, expressed as

$$
\begin{aligned}
\boldsymbol{v}_P(\boldsymbol{r},t) &= \boldsymbol{v}_{P-}(\boldsymbol{r},t) + \boldsymbol{v}_{P+}(\boldsymbol{r},t) + \boldsymbol{v}_{S+}(\boldsymbol{r},t) \\
&= \frac{u_{\boldsymbol{p}^-}}{v_p}\boldsymbol{p}^-\dot{W}(t - \frac{\boldsymbol{r}\cdot\boldsymbol{n}_p^-}{v_p}) + \frac{u_{\boldsymbol{p}^+}}{v_p}\boldsymbol{p}^+\dot{W}(t - \frac{\boldsymbol{r}\cdot\boldsymbol{n}_p^+}{v_p}) \\
&\quad + \frac{u_{\boldsymbol{s}^+}}{v_s}\boldsymbol{s}^+\dot{W}(t - \frac{\boldsymbol{r}\cdot\boldsymbol{n}_s^+}{v_s}),
\end{aligned}
\tag{2.9}
$$

where superscript $-$ represents the up-going wave; superscript $+$ represents the down-going wave; $\boldsymbol{p}$ and $\boldsymbol{s}$ are P-wave and S-wave polarization vectors respectively, previously denoted by polarization vector $\boldsymbol{m}$ in equation 2.6, and $\boldsymbol{n}$ is propagation direction; the downgoing scalar displacement amplitude $u_{\boldsymbol{p}^+}$ and $u_{\boldsymbol{s}^+}$ equal the multiplication of the upgoing scalar displacement amplitude $u_{\boldsymbol{p}^-}$ and corresponding PP and PS reflection coefficients R_{pp} and R_{ps}, respectively. On the right hand side, the first two terms represent up-going and down-going P-waves, satisfying the relationships $\boldsymbol{p}^- = \boldsymbol{n}_p^-$ and $\boldsymbol{p}^+ = -\boldsymbol{n}_p^+$ respectively, whereas the third term satisfies $\boldsymbol{s}^+ \cdot \boldsymbol{n}_s^+ = \boldsymbol{0}$, representing the down-going S-wave. Combining these relationships with equation 2.7 and the definition of rotational rate, we write the rotation rate $\dot{\boldsymbol{\Omega}}$ of the particle A as
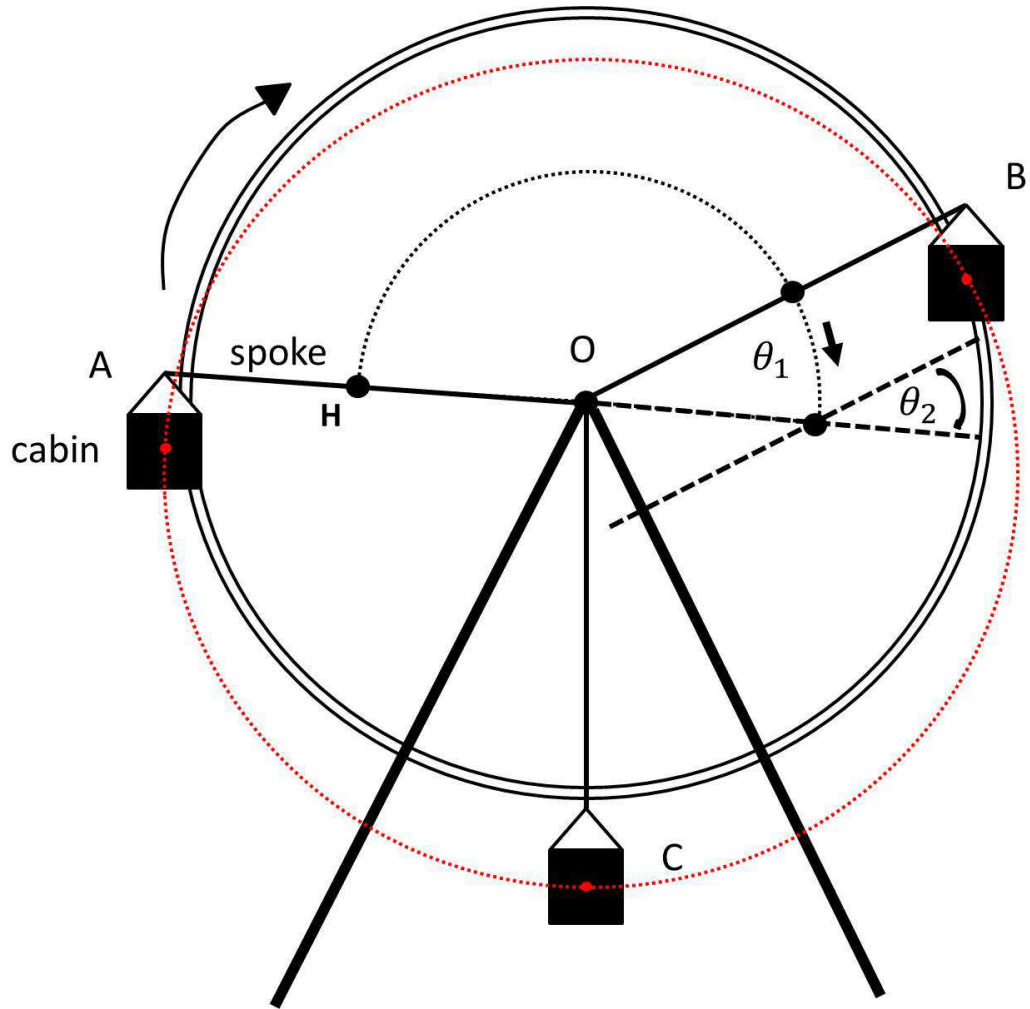
Figure 2.5: A sketch of a Ferris wheel to illustrate the difference between an elliptical motion and a rigid-body rotation. Cabins move clockwise from location A to C along the red dotted path. Large red dot: center of the cabin. The cabins display elliptical motion but are rotation free since up is always up. Because the Ferris wheel forms a ring, the path of the cabins is also circular. O is the centre of the motion path of the spokes. H is the centre of a spoke, denoted by a black dot. The center point H of the spoke displays both self-rotation and elliptical motion. Black dotted half circle: elliptical motion path around centre O. Black dashed lines: spoke locations after motion. θ_1: elliptical motion angle. θ_2: self-rotation angle. In a similar fashion, P-waves can display elliptical polarizations but are rotation free, whereas S-waves can have both. see also Figure 2.3.

$$\dot{\boldsymbol{\Omega}}_{P-}(\boldsymbol{r},t) = \frac{1}{2}\nabla \times \boldsymbol{v}_{P-}(\boldsymbol{r},t) + \frac{1}{2}\nabla \times \boldsymbol{v}_{P+}(\boldsymbol{r},t) + \frac{1}{2}\nabla \times \boldsymbol{v}_{S+}(\boldsymbol{r},t)$$
$$= \frac{u_{\boldsymbol{p}-}}{2v_p}\boldsymbol{n}_p^- \times \boldsymbol{p}^- \dot{W}(t - \frac{\boldsymbol{r}\cdot\boldsymbol{n}_p^-}{v_p}) + \frac{u_{\boldsymbol{p}+}}{2v_p}\boldsymbol{n}_p^+ \times \boldsymbol{p}^+ \dot{W}(t - \frac{\boldsymbol{r}\cdot\boldsymbol{n}_p^+}{v_p})$$
$$+ \frac{u_{\boldsymbol{s}+}}{2v_s}\boldsymbol{n}_s^+ \times \boldsymbol{s}^+ \dot{W}(t - \frac{\boldsymbol{r}\cdot\boldsymbol{n}_s^+}{v_s}) \tag{2.10}$$
$$= \frac{u_{\boldsymbol{s}+}}{2v_s}\boldsymbol{n}_s^+ \times \boldsymbol{s}^+ \dot{W}(t - \frac{\boldsymbol{r}\cdot\boldsymbol{n}_s^+}{v_s}),$$

where the particle rotational motion generated by the incident P-wave on the free surface comes from P-to-S-wave conversion. Similarly, we can get the particle rotational motion by an incident S-wave on the free surface, given by

$$\dot{\boldsymbol{\Omega}}_{S-}(\boldsymbol{r},t) = \frac{u_{\boldsymbol{s}-}}{2v_s}\boldsymbol{n}_s^- \times \boldsymbol{s}^- \dot{W}(t - \frac{\boldsymbol{r}\cdot\boldsymbol{n}_s^-}{v_s}) + \frac{u_{\boldsymbol{p}+}}{2v_p}\boldsymbol{n}_p^+ \times \boldsymbol{p}^+ \dot{W}(t - \frac{\boldsymbol{r}\cdot\boldsymbol{n}_p^+}{v_p})$$
$$+ \frac{u_{\boldsymbol{s}+}}{2v_s}\boldsymbol{n}_s^+ \times \boldsymbol{s}^+ \dot{W}(t - \frac{\boldsymbol{r}\cdot\boldsymbol{n}_s^+}{v_s}) \tag{2.11}$$
$$= \frac{u_{\boldsymbol{s}-}}{2v_s}\boldsymbol{n}_s^- \times \boldsymbol{s}^- \dot{W}(t - \frac{\boldsymbol{r}\cdot\boldsymbol{n}_s^-}{v_s}) + \frac{u_{\boldsymbol{s}+}}{2v_s}\boldsymbol{n}_s^+ \times \boldsymbol{s}^+ \dot{W}(t - \frac{\boldsymbol{r}\cdot\boldsymbol{n}_s^+}{v_s}).$$

where the particle rotational motion generated by the incident S-wave on the free surface comes from the superposition of incident and reflected S-waves. Equations 2.10 and 2.11 imply that both incident P- and S-waves are able to generate rotational motions which are detectable by rotational sensors.

Rotational motion right on the free surface is a special case since the zero traction boundary condition needs to be fulfilled. Assuming a homogeneous and isotropic medium, we have the following free surface boundary condition (Cochard et al., 2006),

$$\frac{\partial u_y}{\partial z} = -\frac{\partial u_z}{\partial y},$$
$$\frac{\partial u_x}{\partial z} = -\frac{\partial u_z}{\partial x}. \tag{2.12}$$

Then, from equation $\dot{\boldsymbol{\Omega}} = \frac{1}{2}\nabla \times \boldsymbol{v}$, the rotation rate vector becomes
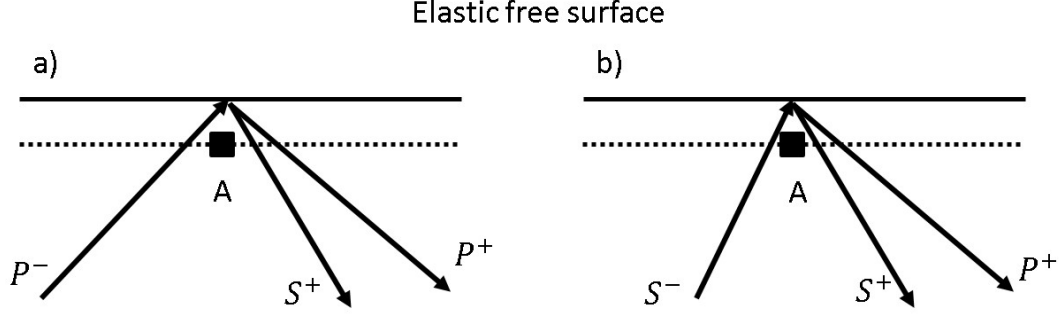
Figure 2.6: Incident P- and S-waves and their corresponding free-surface reflections for illustration of a particle's rotational motion near the free surface. Horizontal solid lines indicates free surface. Black boxes A: an arbitrary particle at a depth (denoted by dashed line) right below the free surface. a) Up-going P-wave (P^-) and reflected down-going P-wave (P^+) and S-wave (S^+). In this case, rotations are due to reflected down-going S-wave (S^+). b) Up-going S-wave (S^-) and reflected down-going S-wave (S^+) and P-wave(P^+). In this case, rotations are due to the superposition of the up- (S^-) and down-going (S^+) S-waves.

$$\dot{\Omega}_x = \frac{\partial v_z}{\partial y},$$

$$\dot{\Omega}_y = -\frac{\partial v_z}{\partial x}, \tag{2.13}$$

$$\dot{\Omega}_z = \frac{1}{2}\left(\frac{\partial v_y}{\partial x} - \frac{\partial v_x}{\partial y}\right),$$

where the horizontal components of rotational motion on the free surface directly represent the spatial gradient of vertical displacement in the horizontal directions. A similar relationship can be obtained for rotational displacement by replacing rotational rate $\dot{\Omega}$ and particle velocity v with rotational displacement Ω and particle displacement u in equation 2.13. This equation is important for the application of wavefield interpolation or reconstruction which is introduced in a later section.

In reality, both rotational rate and particle velocity sensors are normally shallowly buried to be better coupled with the ground. We then can approximate $\dot{\Omega}_x$ and $\dot{\Omega}_y$ in equation 2.13 using the recorded particle velocities assuming

that the buried sensors are adjacent to the free surface.

2.3   Acquisition

In this section we briefly describe several portable rotation sensors with possibilities for exploration geophysical usage. More detailed review and references about other existing instruments for global seismological purpose, such as the ring laser gyroscope can be found in Igel et al. (2015). Information on detailed laboratory and field testing of several commercial rotational sensors can be found in Nigbor et al. (2009) and Lee et al. (2012).

2.3.1   Fiber optic gyroscope

Fiber optic gyroscopes are widely applied in navigation and control of missiles, planes, submarines and unmanned underwater vehicles since they measure pitch, roll and yaw. They are based on the Sagnac effect, where two beams of light traveling in an enclosed fiber-optic loop in opposite directions display interference phenomena. When there are rotational motions, phase changes and beat frequencies can be observed between two counter propagating light beams. The phase shift is proportional to the rotation rate. The equipment sensitivity can be improved by increasing the number of loops (Schreiber et al., 2009b). Also three fiber optic gyroscopes can be assembled together with perpendicular normal vectors, to create a three-component sensor, measuring rotation rate in all directions (Velikoseltsev et al., 2012).

Many field and laboratory tests have shown the ability of fiber optic gyroscope in measuring ground rotations with high sensitivity, wide bandwidth and good stability (Schreiber et al., 2009b; Jaroszewicz et al., 2012; Kurzych et al., 2014). Igel et al. (2015) note that a high performance fiber optic gyroscope has a resolution ranging from 4×10^{-6} to 0.004 rad/s with a bandwidth from 0.01 to 500 Hz. Bernauer et al. (2016) introduces a single component commercial rotational sensor based on an interferometric fiber-optic gyroscope (IFOG). They show the feasibility of application of this sensor for exploration purposes, due to its portability, low power consumption, good time stamping stability

and wide dynamic range. With such encouraging test results, we are expecting a real application of fiber optic rotational sensors for exploration geophysics in a near future.

2.3.2   Electrokinetic sensor

The Electrokinetic sensor is the most widely deployed rotational sensor in the field (Kozlov et al. (2006), Pierson et al., 2016). This type of sensor is based on the molecular-electronic transfer (MET) technique, which constitutes a hollow toroidal dielectric tube fully filled with an electrolyte solution and a conversion cell assembled inside the tube where the solution can freely pass. A voltage difference is applied to the conversion cell to generate a reference electrical current in the solution. An external angular acceleration will generate a convection flow in the tube which leads to a variation of electrical current through the conversion cell. Eventually a voltage change is measured and transformed proportionally into the angular acceleration. More technical details including descriptions of field testing are given by Lee et al. (2012), Egorov et al. (2015) and Zaitsev et al. (2015).

However, drawbacks are their strong dependency on temperature (Bernauer et al., 2012; Lee et al., 2012) and wide variations between individual sensors (Pierson et al., 2016).

2.3.3   Magnetohydrodynamic sensor

The Magnetohydrodynamic sensor is another promising rotational sensor for seismic field applications. These types of sensors generally consist of a conductive liquid in a ring or cylindrical shell, with a static magnetic field applied along the axis of symmetry. When there is rotational motion on the ground, the sensor rotates and the conductive liquid move in the shell relative to the magnetic field due to inertia. A current is then generated in the fluid, whose potential is proportional to the rotation rate. Three-component sensors consist of three orthogonal rings measuring ground rotation in three directions. More technical details including descriptions of field testing can be found in Pierson et al. (2016).

The size of a magnetohydrodynamic sensor is generally of the order of ten centimeters depending on the manufacturer, which is similar to the fiber-optic gyroscope (Pierson et al., 2016). Also, the power consumption is low (Pierson et al., 2016). These features make them attractive for applications in exploration seismology.

2.3.4 Magnetometer

Barak et al. (2015) proposed that rotational data can be derived from Induction-Coil Magnetometer (ICM) recordings. The initial conceptual idea is by Kappler et al. (2006) to explain the coseismic signal detected by the electromagnetic components due to ground rotations. The basic idea is when three orthogonal ICMs are rotating as a result of an incident seismic wave, the projection of the local Earth's magnetic field on the three components of ICMs change, resulting in a change of flux through the coils and consequently the generation of a current. Copper wire is wound around a magnetically permeable core in ICMs. Barak et al. (2015) compute the associated ground rotations then from the measured current and found a good match between derived rotations and measured rotations by a rotational sensor.

Their results are encouraging. However, the method is conditional to stationary magnetic field during experiments.

2.3.5 Microelectromechanical gyroscope

The microelectromechanical gyroscope, known as MEMS gyroscope, is based on measuring Coriolis acceleration (Allen, 2009). This technique has been widely used in civilian purposes, such as mobile phone gesture recognition (Li et al., 2013), automotive crash detection (Mizuno et al., 1999) and hard-drive read-write heads localization (Gola et al., 2003).

The small size, low cost and power consumption of the MEMS gyroscope also make them strong candidates for seismic applications. D'ALessandro et al. (2014) build a seismic network of densely distributed stations in urban area, where each station is a combination of a capacitive accelerometer, a MEMS gyroscope and a magnetometer, all tri-axial. Using this network, they success-

fully recorded the rotational and the translational motion simultaneously from a moderate-magnitude earthquake. Furthermore, D'ALessandro and A'Anna (2014) retrieve the orientations of ocean bottom seismometers and downhole seismic sensors by directly measuring the rotational displacements using integrated low cost MEMS gyroscopes. The above two applications are both based on strong rotational motions. Exploration geophysics, however, requires MEMS gyroscopes with much higher sensitivity to infinitesimal deformations. Projetti et al. (2014) develop a prototype of a new capacitive MEMS rotation sensor (R-MEMS) with low self-noise and high bandwidth which can be used for hydrocarbon-related applications.

2.3.6 Array derived rotations

Seismologists also use arrays of traditional translational seismometers to derive rotational signals (Huang, 2003). This is clearly also an option for applied geophysical applications. In practice, a finite differencing method is applied to calculate ground rotation from particle displacement measurements (Brokevsova et al., 2012; Lin et al., 2012). The second order approximation of the relationship $\dot{\boldsymbol{\Omega}} = \frac{1}{2} \boldsymbol{\nabla} \times \boldsymbol{v}(\boldsymbol{r})$ is often used, given by

$$\dot{\Omega}_x(x,y,z) \approx \frac{1}{2} \left[\frac{v_z(x, y+\frac{dy}{2}, z) - v_z(x, y-\frac{dy}{2}, z)}{dy} - \frac{v_y(x, y, z+\frac{dz}{2}) - v_y(x, y, z-\frac{dz}{2})}{dz} \right],$$

$$\dot{\Omega}_y(x,y,z) \approx \frac{1}{2} \left[\frac{v_x(x, y, z+\frac{dz}{2}) - v_x(x, y, z-\frac{dz}{2})}{dz} - \frac{v_z(x+\frac{dx}{2}, y, z) - v_z(x-\frac{dx}{2}, y, z)}{dx} \right],$$

$$\dot{\Omega}_z(x,y,z) \approx \frac{1}{2} \left[\frac{v_y(x+\frac{dx}{2}, y, z) - v_y(x-\frac{dx}{2}, y, z)}{dx} - \frac{v_x(x, y+\frac{dy}{2}, z) - v_x(x, y-\frac{dy}{2}, z)}{dy} \right],$$

$$(2.14)$$

where (x, y, z) is the spatial coordinate; dx, dy and dz are spatial intervals between adjacent seismometers in each axis. A conceptual instrument has been built according to Equation 2.14, consisting of 6 pairs of single-component geophones. Rotational motion is then computed by differencing the recordings from each pair of geophones (Brokevsova et al., 2012). Its size of roughly a

26

cubic foot excludes commercial use.

Better approximations may be obtained by two enhanced applications of equation 2.14, namely 1) higher-order finite difference to $\dot{\boldsymbol{\Omega}} = \frac{1}{2}\boldsymbol{\nabla} \times \boldsymbol{v}(\boldsymbol{r})$, or 2) an L2 norm inversion based approach, called the Seismogeodetic method (Spudich et al., 1995).

However, the finite differencing approach sometimes faces some critical challenges (Cochard et al., 2006). For example, strain-rotation coupling is a significant nonlinear effect due to strong near-surface heterogeneities and topography near the array area (Van Driel et al., 2012). Array derived rotations in this case are linear approximations of the true rotational motion with possibly large error (Spudich et al., 1995). Another problem comes from noise contamination. Suryanto et al. (2006) first compared array-derived rotations with direct measurements from a ring laser gyroscope. They find that even low levels of noise may considerably influence the accuracy of the array-derived rotations when the minimum requirement of three 3-component sensors is reached. Increasing the number of particle displacement(velocity) sensors enhances the accuracy, but also the cost, in particular since the distance between the sensors has to be considerably smaller than the smallest wavelengths to prevent spatial aliasing.

Muyzert et al. (2012) conduct a small field test using several Electrokinetic rotational sensors and an array of densely distributed geophones installed on a free surface. A relatively good match is shown in figure 2.7 between the directly measured horizontal rotation rate using the rotational sensors (black traces) and the approximated horizontal spatial gradient (blue traces) by differencing the vertical displacements between two adjacent geophones from the field test. The result confirms that on the free surface the horizontal rotation rate equals the spatial gradient of the vertical displacement in the horizontal direction, as shown in equation 2.13.
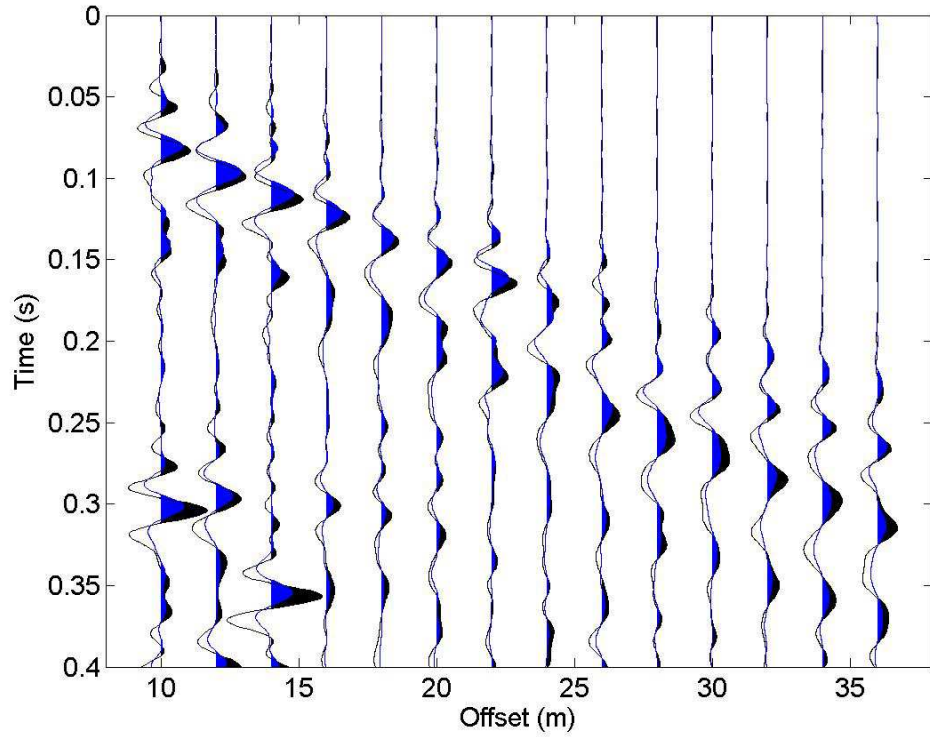
Figure 2.7: Comparison between z-component rotation rate data on the surface obtained from rotational sensors (black traces) and the spatial gradient in the x-direction of the wavefield recorded by z-component velocity sensors (blue traces). A time-squared gain has been applied for visual comparison (Muyzert et al., 2012). A good match exists between the directly measured rotations and reconstructed spatial gradients, indicating that on the free surface the horizontal rotation rate can be approximated by the spatial gradient of the vertical particle velocity.

2.4 Possible applications in exploration geophysics

2.4.1 Collocated observations of rotations and displacements

Traditionally, geophysicists use spatially-distributed arrays of three-component sensors measuring particle velocity or acceleration to determine wave field characteristics such as type (body or surface wave), propagation directions and apparent or true velocities (Figure 2.8a). These sensors measure the wavefield but not its spatial derivatives. The latter may be approximated from the differences between individual sensors.

However, various investigations demonstrate the possibility of a collocated observations of rotations and displacements (si$x$-component sensor) as in Figure 2.8b, and compare predictions with field data (Igel et al., 2005; Aldridge and Abbott, 2009). They show that a combination of a three-component particle velocity seismometer and a three-component rotational sensor in one single point receiver is sufficient to measure the full wavefield and its spatial gradients. The back-azimuth and the S-wave phase velocity can then be accurately calculated even with only one si$x$-component sensor under the assumption of incident plane waves. Collocated displacement and rotational sensors can thus be used for natural separation of P- and S-waves.

The si$x$-component sensor is thus the most elegant solution to capture the full wavefield and its spatial derivatives; yet no such sensor exists currently. The premise of recording the wavefield and its spatial gradients is the basis for most following applications.

2.4.2 Seismic wavefield interpolation

One important application of rotational seismology is seismic trace interpolation in order to remove spatial aliasing. In marine and land seismic acquisition, strong aliasing arises due to a limited number of sensors or large spatial separation between cables or nodes. If the sampling interval is larger than the

a)

Conventional approach: spatially-distributed array
of 3C motion sensors:

b)

New approach: co-located 3-C velocity and 3-C
rotation sensors (a 'six-component' seismometer):

r_R

r_A

n

n

Plane wave $\boldsymbol{w}(t - \frac{r \cdot n}{c})$

P-wave: $\boldsymbol{\Omega}(\boldsymbol{r}_R, t) = 0$

S-wave: $\boldsymbol{\Omega}(\boldsymbol{r}_R, t) \neq 0$
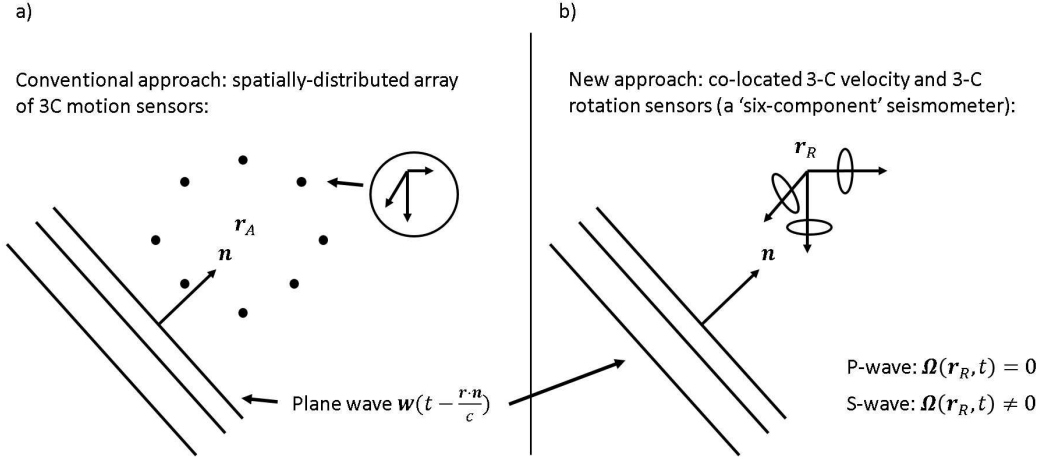
Figure 2.8: Comparison of (a) a circular array (centered at r_A) of 3-component seismometers with (b) a 'point seismic array' consisting of a 3-component displacement sensor co-located with a 3-component rotational sensor at position r_R. A train of plane seismic wave fronts propagates with speed c in the direction of unit vector **n**. Measurement of rotation vector $\boldsymbol{w}(\boldsymbol{r}_R, t)$ identifies the type (P and S) of the incident wave. A single 6-component sensor can determine the back-azimuth and the S-wave phase velocity which traditionally requires measurements by a circular array of 3-component seismometers.

spatial Nyquist interval, aliased replicas of the original signal are generated. Superposition of replicas may appear more than once, generating first-order or higher order aliasing. First-order aliasing means superposition of the original signal and one replica; in higher-order aliasing multiple replicas are superposed. The amount of aliasing is determined by the incident wave frequency and the sampling wavenumber. For a fixed sampling wavenumber, the aliasing order increases with increasing incident wave frequency.

In order to remove aliasing, Linden (1959) proposed a multichannel sampling theorem using the recorded signal and its derivative to interpolate the wavefield. Although originally proposed for signal interpolation in the time domain, it can also be used for spatial interpolation (Vassallo et al., 2010, Muyzert et al., 2012). Rotational sensors can provide such spatial derivatives as they measure the curl of the wavefield.

Vassallo et al. (2010) propose a gradient-based interpolation method for multicomponent data, specifically for marine seismic acquisition. The basic idea is that the whole multichannel wavefield and its derivatives are considered

a linear combination of continuous functions of space and wave number. Next they determine the dominant basis functions iteratively which are then used for wavefield reconstruction at any point in space and time. In each iteration, a new dominant function is determined through minimization of weighted combination of the residual data signals and their gradients, which are then added to the previous iteration, and so on. When the energy of the residuals is sufficiently reduced, the iterations are ended. This way, a combination of continuous functions is determined which is used for wave field reconstruction. In their implementation, no rotation sensors are used to get the derivatives. The derivatives are obtained from differentiation between single sensors.

Muyzert et al. (2012) show the feasibility of using rotation sensors for interpolation of elastic land data. The basic idea of their method is that in the $f-k$ domain, the measured vertical component of wavefield and spatial derivative with respect to the x direction are the linear sum of the aliased and nonaliased wavefields, denoted by u_{al} and u_{na}. A linear inversion then solves for the aliased and non-aliased wavefields. They demonstrate that the combination of the wavefield and its spatial derivative allows for reconstruction of the non-aliased wavefield up to twice the geophone spacing applicable to non-gradient based wavefield interpolation methods. An example is given in Muyzert et al. (2012) (Figure 2.9). In their example, originally the datasets are aliased due to sparse spatial sampling (Figure 2.9a and b). After combining with spatial derivative recordings, nonaliased wavefields are obtained with the help of the interpolation method (Figure 2.9c).

2.4.3 Ground roll removal

In exploration geophysics, ground roll is the general name for both Rayleigh and Love waves which exist in almost all land datasets. These waves travel along the free surface and hold limited information on the reservoir. Ground roll is considered as noise in reflection seismology, since it does not contain information regarding the deep subsurface. Part of the standard seismic processing flow is to remove it. Two different approaches involving rotational recordings for ground roll removal are proposed by Edme et al. (2013) and Barak et al.
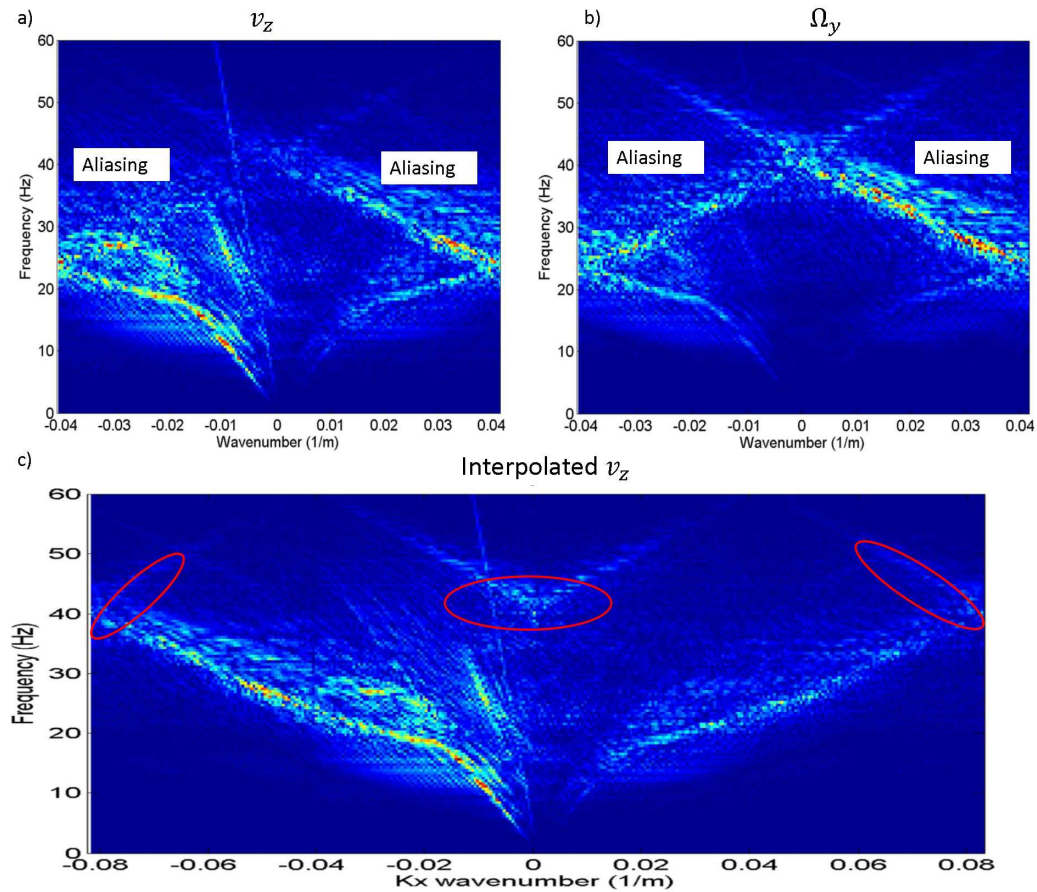
Figure 2.9: (a) and (b) The $f-k$ spectra with strong aliasing for the wavefield v_z and its spatial derivative with respect to the x direction. c) The $f-k$ spectra after dealiasing. (Muyzert et al., 2012). By combining the recorded wavefield and its spatial derivative, spatial aliasing is greatly reduced. Red circles show remaining aliased signal. Note extended wavenumber scale for interpolated wavefield v_z.

(2014).

Edme and Muyzert (2013) derive from equation 2.13 and verify using field data that on the free surface, recordings of horizontal rotational rate can be approximated by the slowness-scaled vertical component of particle acceleration recordings, as

$$
\begin{aligned}
\dot{\Omega}_x &= -p_y A_z = -\frac{\partial V_z}{\partial y}; \\
\dot{\Omega}_y &= p_x A_z = \frac{\partial V_z}{\partial x};
\end{aligned}
\tag{2.15}
$$

where $p_x = \partial t_T / \partial x$ and $p_y = \partial t_T / \partial y$ are the local horizontal slownesses and t_T is the travel time of the surface wave under consideration; $A_z = \partial V_z / \partial t_T$ is the vertical component of acceleration. Equation 2.15 implies that slowly propagating waves (typically ground rolls), are amplified whereas fast propagating waves (typically body waves) are weakened in rotational recordings. Thus the derived horizontal rotational data provide a noise model for the ground roll (Edme and Muyzert, 2014). Then the ground roll is removed by using an adaptive subtraction of the noise model from the vertical component geophone data. A real data example is shown in Figure 2.10, where ground-roll removal is clearly visible by comparing datasets before and after applying their proposed method (Edme et al., 2013).

Barak et al. (2014) use a different approach. They select a portion of the six-component data that contain ground roll energy. They use singular value decomposition to identify the 6C polarization of the ground roll, and then search for similar polarizations in the entire dataset. Where the data have similar polarization to the ground roll, the first eigenimage is weighted down. This results in an attenuation of the ground roll energy on all six components.

2.4.4 Time-reversal extrapolation

Wavefield extrapolation is a fundamental step of many wave equation based migration algorithms. The inclusion of both the wavefield and its spatial gradients holds promise for both reflection seismic imaging as well as microseismic imaging (Li and Van der Baan, 2016, Vasconcelos, 2013).
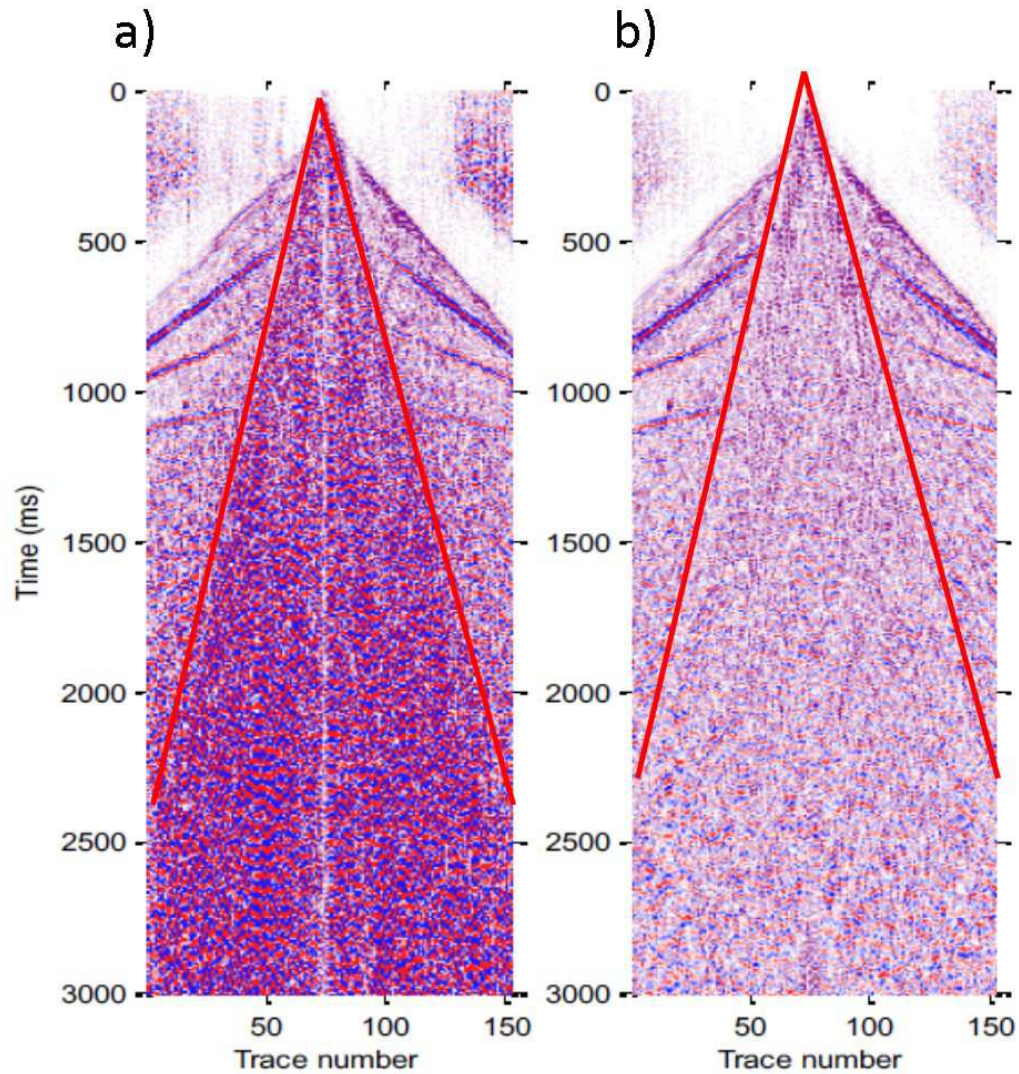
Figure 2.10: Comparison of real data before and after ground-roll removal. (a) Real data acquired in United Arab Emirates before ground-roll removal. Ground-roll denoted by the area within the two red lines, which is a low-velocity, low-frequency and high-amplitude coherent noise generated by surface waves. (b) With the use of rotational motion information, ground-roll is removed significantly. (Edme et al., 2013).

Event localization is a fundamental step in microseismic monitoring. Broadly speaking, event localization methods can be categorized into two types: travel-time based and migration based methods. The travel-time based localization methods require event picking, which can often be challenging for low quality data. Migration based methods avoid picking by backward propagating the microseismic energy to the hypocentre location.

Reverse time migration (Whitmore, 1983, McMechan, 1983) can be used for microseismic source localization by extrapolating the observed three-component particle displacement/velocity field back in time using the wave equation. Eventually, the backward propagating energy will collapse at the source location assuming the velocity model is accurate. Li and Van der Baan (2016) demonstrate that using the combination of the wavefield and its spatial gradient enhances quality of the location images by suppressing focusing artefacts. For acoustic wavefield imaging this is achieved by using both pressure (hydrophone) and particle-velocity data (Li and Van der Baan, 2016), whereas both particle-velocity and rotational sensors are used for elastic wavefield imaging (Li and Van der Baan, 2015). Figure 2.11 is an acoustic example in a homogeneous medium comparing the event localization image for three data combinations, all with strong noise contaminations. Estimated source location is selected using a maximum magnitude criterion. When we use only one type of data, a ghost event appears on the extrapolated source image (focusing points on the left in Figure 2.11a,b), due to the lack of directivity of seismic wave equations. Only the true event location remains present when combining both pressure and particle velocity recordings (Figure 2.11c). Moreover, the estimated source location is the same as the true source location when using both pressure and its spatial gradient (right panel in Figure 2.11c), whereas the estimated location is away from the true location when either pressure or its spatial gradient is used (right panels in Figure 2.11a and b). This demonstrates that the source localization based on the combination of both pressure and its gradient is more stable than the one using only a single type of data. Although their work deals explicitly with microseismic event localization, the inclusion of spatial gradient information is likely to enhance the performance of wave-equation based reflection imaging too, for instance, by reducing the influence of spatial aliasing or

aperture-related artefacts.

2.4.5 Moment tensor inversion

Seismic moment tensor is a useful mathematical tool to represent a seismic point source (Aki and Richards, 2002). The point source is a simplification of a seismic event, such as an earthquake due to natural fracturing (Jost and Herrmann, 1989) or microseismicity due to human activities (Eyre and Van der Baan, 2015). The seismic moment tensor is written as

$$\boldsymbol{M} = \begin{pmatrix} M_{xx} & M_{xy} & M_{xz} \\ M_{yx} & M_{yy} & M_{yz} \\ M_{zx} & M_{zy} & M_{zz} \end{pmatrix}, \tag{2.16}$$

where each element is a force couple used to describe the source mechanism. The diagonal elements represent normal strain changes whereas the off-diagonal elements represent shear strain changes. Each pair of off-diagonal elements M_{ij} and M_{ji} (i, $j = x, y, z$ and $i \neq j$) form balanced double-couples. The moment tensor can help seismologists understand the seismic event magnitude, fracture type and fracture orientation (Jost and Herrmann, 1989, Eyre and Van der Baan, 2015).

Traditionally, moment tensor inversion is performed using particle displacement recordings from an array of sensors on the surface or inside boreholes, according to equation 5 in Jost and Herrmann (1989)

$$d_n(\boldsymbol{r}, t) = M_{pq} * [\partial_q G_{np}(\boldsymbol{r}, t) * s(t)], \tag{2.17}$$

where the Einstein convention is used of summation over repeated indices; $d_n(\boldsymbol{r}, t)$ is the n-component of the particle displacement recordings from a receiver located at $\boldsymbol{r}$; M_{pq} is a scalar form of the moment tensor; $G_{np,q}(\boldsymbol{r}, t)$ is the scalar form of the spatial gradient of the n-component of the Green's function of either body waves or surface waves; $s(t)$ is a wavelet in time domain; $*$ denotes the temporal convolution. Traditional Moment tensor inversion often suffers from some critical problems, such as the lack of an accurate velocity model, a
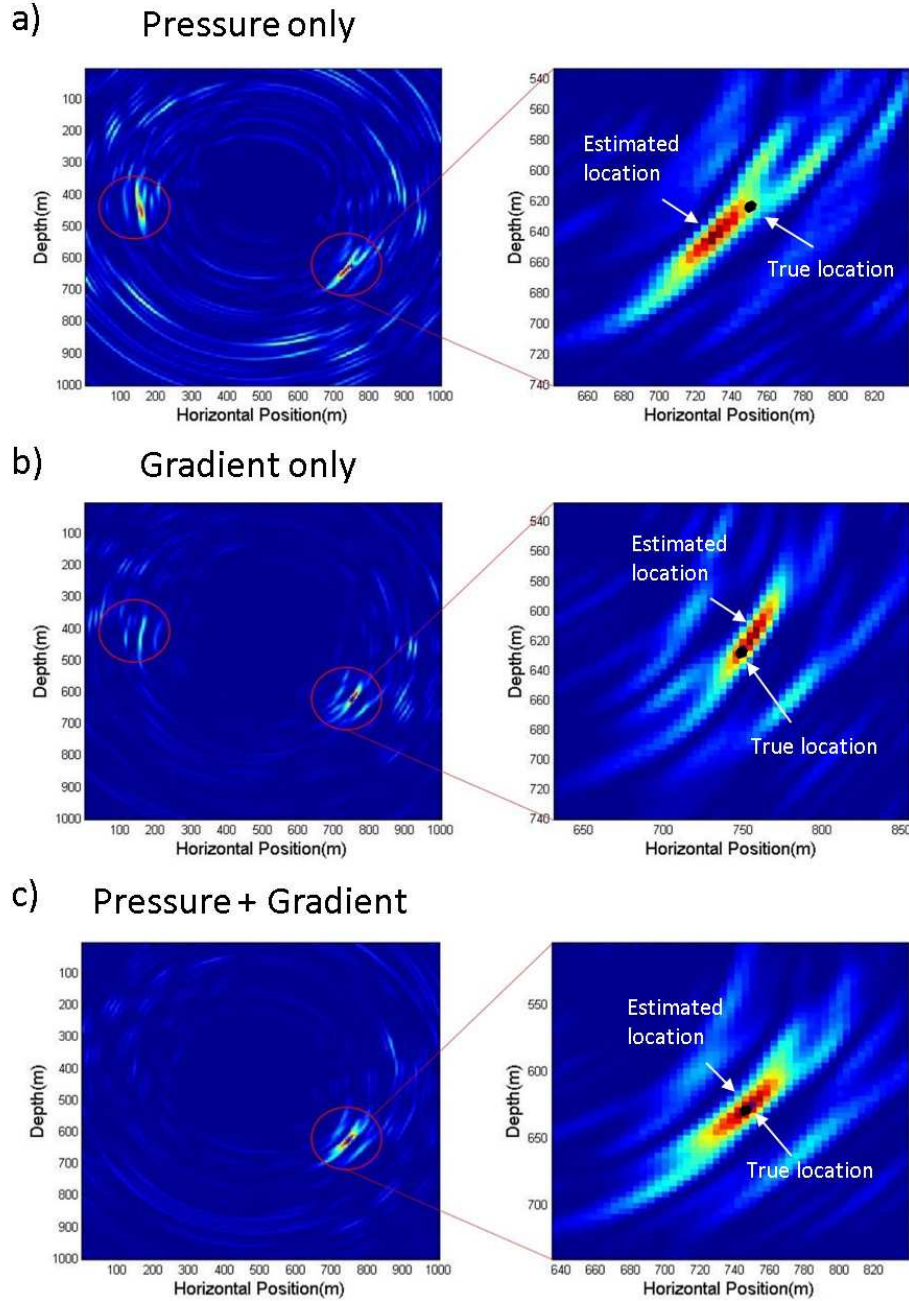
Figure 2.11: Comparison of the event image obtained by time-reversal extrapolation of three data combinations, namely pressure recordings only, particle velocity recordings only and both pressure and particle velocity recordings (gradient). Small black dots in right column shows true microseismic event location. Hot colors are high amplitudes. Estimated and true event locations are denoted using the white arrows. With either (a) pressure or (b) spatial gradient only, back-propagated energy focuses at both ghost (left most circles) and near true locations (right most circles). (c) With the combination of pressure and spatial gradient data, the ghost event is canceled and the estimated event location coincides with the true location.

sparse distribution of sensors with limited coverage and extremely low SNR especially for surface-array recorded microseismicity. All these problems lead to the non-uniqueness and inaccuracy in inverted source mechanisms (Bernauer et al., 2014). Study shows that a joint inversion of rotational and particle displacement data can better constrain earthquake moment tensor solutions (Bernauer et al., 2014; Donner et al., 2016; Reinwald et al., 2016).

Bernauer et al. (2014) compare the results using two combinations of synthetic recordings in a Bayesian probabilistic finite source inversion, namely 1) 20 stations of particle velocity recordings only; 2) ten particle velocity and ten rotational recordings at the same locations as before. They found that the source properties are much better constrained when using both rotational and particle velocity data. Similarly, Donner et al. (2016) get an improved estimation of moment tensors and centroid depth for a shallow, medium-sized strike-slip earthquake at a regional distance using the combination of particle velocity and rotational recordings of surface waves, compared to results using particle velocity recordings only.

The benefit from adding rotational recordings can be shown by a rotational moment tensor relationship, derived by taking half the curl of the equation 2.17, given by

$$\Omega_l(\boldsymbol{r}, t) = \frac{1}{2} M_{pq} [\epsilon_{lkn} \partial_k \partial_q G_{np}(\boldsymbol{r}, t) * s(t)], \tag{2.18}$$

where $\Omega_l(\boldsymbol{r}, t)$ is the l-component of rotational recordings. This equation could be used as an extra constraint in the moment tensor inversion including the rotational motions. On the free surface, the spatial gradient information provided by rotational recordings, which cannot be directly obtained from traditional 3-C displacement recordings (Bernauer et al., 2012), are added to the traditional moment tensor inversion as new a priori, with which an improved result can be expected.

2.4.6 Other possible applications

Another intriguing application may be in vertical seismic profile (VSP) data that are not acquired on the free surface or seabed. Pham et al. (2010) demonstrate theoretically and numerically, that rotational motions of qP-waves in

homogeneous anisotropic elastic media can be significant, which could be used to extract these rock properties. They compute maximum peak rotation rates as a function of Thomsen parameters ϵ and δ^* (Thomsen, 1986), and find a general trend in that the peak qP rotation rates are higher with increasing values of ϵ and δ^*. It is especially worth mentioning that the rotation rates simulated under two realistic scenarios, namely (1) a magnitude 0 microseismic event at a 1km hypocenter distance and (2) a magnitude 7.0 earthquake at a 100km epicenter (Figure 2.13), indicate that the qP rotation rates even in weak anisotropic materials are in the order of μrad/s, which are significant enough to be detected by current instruments (Bernauer et al., 2009, Wassermann et al., 2009). The possibility of using qS-waves to constrain the Thomsen parameter γ is also of interest (J. Gaiser, personal communication, 2016).

Moreover, numerical tests show that rotational motion is also subject to amplitude variations with offset (AVO), as shown in Figure 2.12 (D. F. Aldridge, personal communication, 2016). The model is a 25m thick sandstone with 25% porosity, saturated with different percentages of CO_2. When increasing the content of CO_2 from 25% (Figure 2.12a) to 75% (Figure 2.12b), differences in AVO response increase significantly emphasized by the red circles in the figure. These numerical results imply that rotational AVO may hold substantial information on the subsurface geological properties which supplements traditional displacement based AVO analysis.

Finally, readers are referred to a review paper by Igel et al. (2015) for some other seismological and engineering applications, including velocity tomography and structure response to strong earthquakes.

2.5   Discussion

All of the measurements mentioned in this tutorial can be interpreted by linear elasticity under assumption of infinitesimal strain (Igel et al., 2015), which is justified in exploration geophysics. However, the assumption of infinitesimal strain may not be valid for the source area of a large earthquake or a medium with microstructure (Lee et al., 2009b; Igel et al., 2015). In these cases, the micropolar elasticity is introduced for a more accurate description of particle
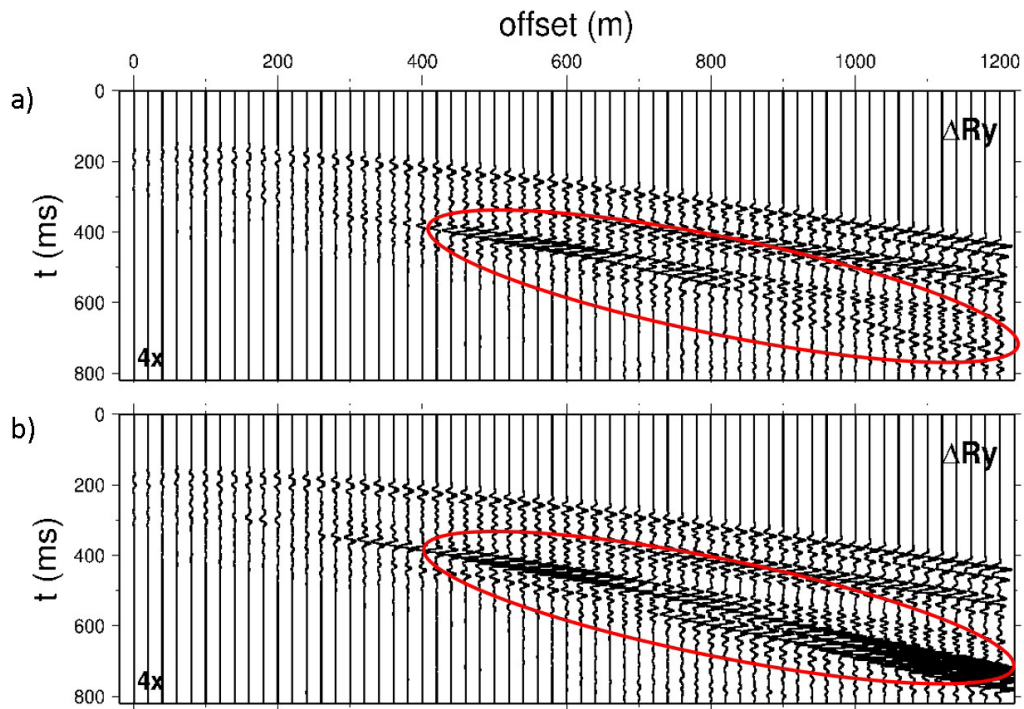
Figure 2.12: Amplitude differences of rotational recordings vary with offset due to variations in CO_2 content. Red circles emphasize significant amplitude changes. Top: 25% CO_2. Bottom: 75% CO_2. (personal communication with D. F. Aldridge, 2016)
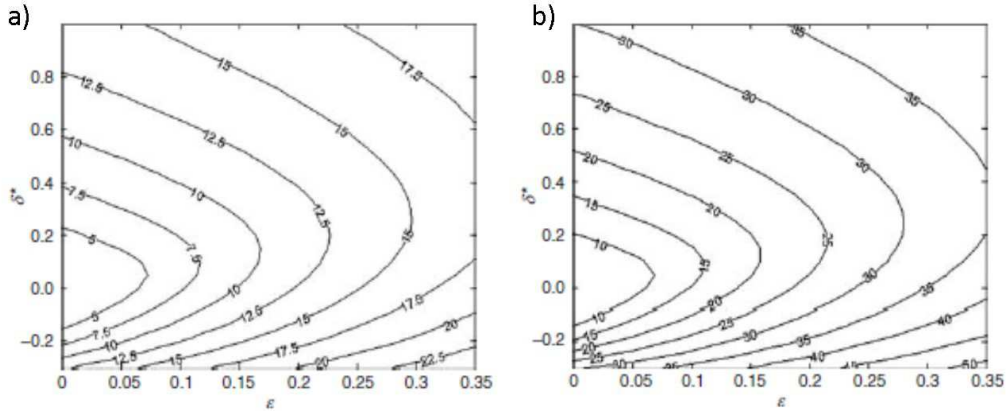
Figure 2.13: The maximum peak rotation rate caused by qP-waves in a full space TI medium as a function of the Thomsen parameters ϵ and δ^*. Every point in the plot depicts the maximum qP rotation rate among all propagation directions for a given combination of ϵ and δ^*. a) A magnitude 0 reservoir microseismic event at 1km hypocenter distance: maximum peak rotation rate. Vertical P velocity $\alpha = 3928$m/s, vertical S velocity $\beta = 2055$ m/s and $\rho = 2590$ kg/m^3, b) a magnitude 7.0 earthquake at 100km epicenter: P velocity $\alpha = 6600$m/s, vertical S velocity $\beta = 3700$m/s and $\rho = 2900 kg/m^3$. Both cases are in order of 10^{-6} rad/s.

motion, though no recordings have seen this kind of motion (Igel et al., 2015). In this tutorial, we mainly focus on the linear elasticity which suffices for exploration geophysics. For readers interested in the micropolar elasticity we refer to Pujol (2009); Kulesh (2009); Grekova et al. (2009); Grekova (2012); Lakes (1995).

The contribution to the improvement of current exploration geophysical methods from the measurement of rotational motion is mainly due to the information of the spatial gradient of the particle displacement field.

Currently rotational sensors are not a proven technology and many sensors are still in a development phase. We thus anticipate that their sensitivity, recording quality, bandwidth and robustness will be enhanced substantially. We thus refrain from comparing and contrasting individual sensor technologies. Interested readers are referred to Bernauer et al. (2012), which introduces a detailed comparison of several rotational sensors.

Likewise, the above tutorial shows only some of the possible applications of rotational sensors in exploration geophysics. We anticipate that many more

will be found.

2.6   Conclusion

In classic elasticity, twelve degrees of freedom are needed to fully describe the motion of an elastic body in a 3D world - six degrees of strain, three degrees of linear motions and three degrees of rotations. Current multi-component recording systems measure particle velocity/acceleration only, which only includes information on strain and linear motions. Rotations have mainly been ignored for a long time, despite the fact that they contain a wealth of information, in particular on the gradient of particle displacement wavefields.

In this paper we describe a select few possible applications, namely wavefield reconstruction, ground roll removal, source imaging, moment tensor inversion, VSP analysis and rotational AVO. Nonetheless we are confident that there are many other applications of the rotational sensor waiting to be discovered.

Chapter 3

Acoustic time reversal extrapolation using pressure and particle velocities [1]

Traditional ray-based methods for microseismic event localization require picking of P- and S-wave first arrivals, which is often time consuming. Polarization analysis for each event is often also needed to determine its absolute location. Location methods based on reverse time extrapolation avoid the need for first-arrival time picking. Traditional reverse time extrapolation only incorporates particle velocity or displacement wavefields. This is an incomplete approximation of the acoustic representation theorem, which leads to artefacts in the back-propagation process. For instance, if the incomplete approximation is used for microseismic event locations using three-component borehole recordings, it produces a ghost event on the opposite side of the well, which leads to ambiguous interpretations. We propose representation-theorem-based reverse time extrapolation for microseismic event localization, combining both the three-component particle velocities (displacements) and the pressure wavefield. The unwanted ghost location is removed by explicitly incorporating both a wave-

---

field and its spatial derivative. Moreover, polarization analysis is not needed, because wavefields will focus at its absolute location during back-propagation. Determination of microseismic event locations using wavefield extrapolation also necessitates a robust focusing criterion. The Hough transform allows for accurate determination of source timing and location by summing wavefront energy in the time-space domain. Synthetic examples demonstrate the good performance of the wavefield extrapolation scheme and focusing criterion in complex velocity fields for borehole acquisition geometries.

3.1 Introduction

Generally, microseismic event localization methods are categorized into two types: travel-time based and migration based methods. The first method requires accurately picking P- and S-wave arrivals before further processing. However, event picking can often be a challenging and time-consuming task for low quality data (Artman et al., 2010). Both mispicks and missing picks negatively influence event locations (Kocon and Van der Baan, 2012; Castellanos and Van der Baan, 2013; Castellanos and Van der Baan, 2015).

Migration based methods avoid arrival time picking, possibly rendering them more suitable for low SNR data (Artman et al., 2010). In their simplest form, traveltime tables are created for each possible grid location. A semblance analysis over the forward predicted traveltimes then yields potential microseismic event locations (Duncan et al., 2008). In this method, a 3D grid volume is created in which each volume cell represents a possible microseismic event location. Then time shifts that correspond to the travel time from each possible location to all receivers are applied to the microseismic records followed by semblance analysis of the time-shifted microseismic records. The grid point with the highest semblance energy can be considered as the most likely possible event location for a relatively accurate velocity model (Duncan et al., 2008; Chambers and Kendall, 2008).

In this paper we explore time reversal extrapolation for determining microseismic event locations. This method is similar to reverse time migration (RTM) (McMechan, 1983; Whitmore, 1983; Baysal et al., 1983). In traditional
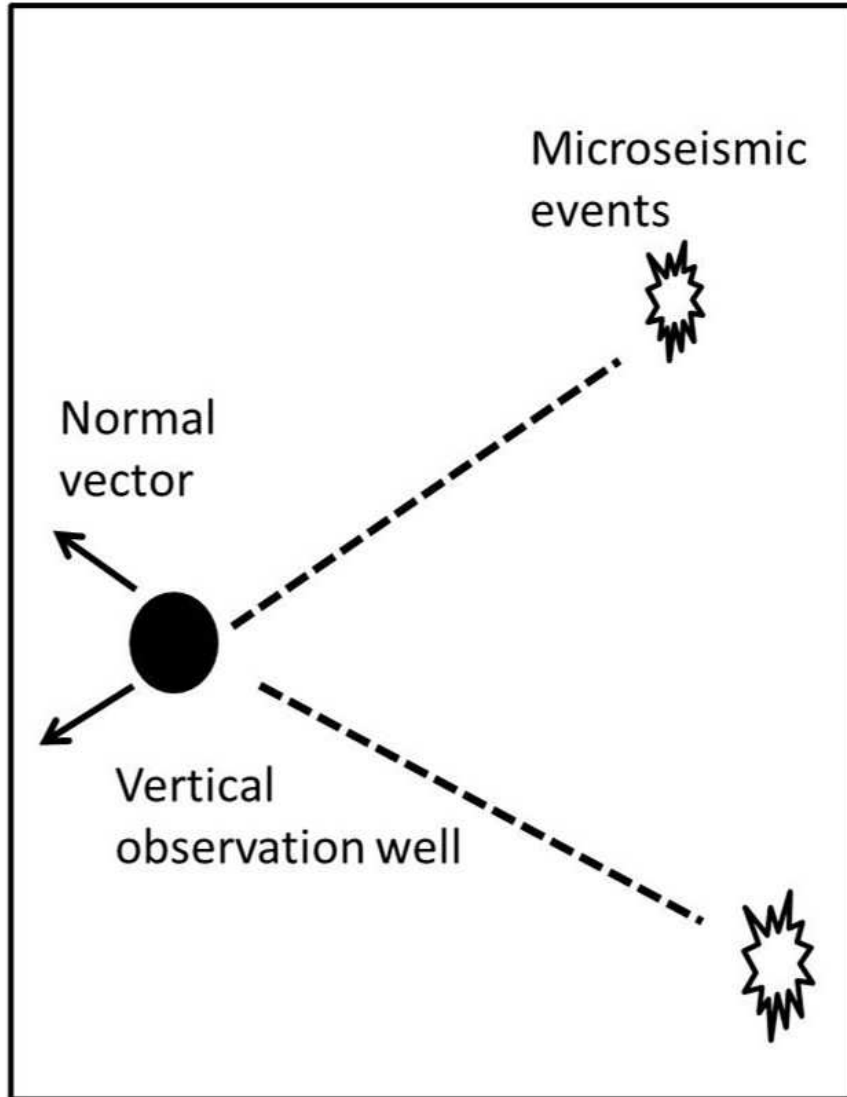
Figure 3.1: Map view of vertical observation geometry for microseismic event localization. Approximate angular range θ in normal vectors (solid black arrows) is determined by locations of perforation shots. Black dashed lines denote 2D planes defined by the vertical observation well and corresponding normal vectors.

RTM, the receiver-side particle displacement (or particle velocity) wavefield is injected into a smoothed velocity model, followed by application of an imaging condition. Sharp contrasts in the model will generate artefacts due to secondary reflections, which are avoided by smoothing. RTM has been used for earthquake fault imaging (McMechan, 1985), thus showing promise for determining event hypocenters.

Traditional time reversal extrapolation uses a finite difference operator for extrapolation (Artman et al., 2010; Fleury and Vasconcelos, 2013). In this paper we introduce an alternative migration based algorithm based on the acoustic representation theorem, allowing us to use either pressure data, three-component particle displacement or velocities, or both pressure and displacement. This has the advantage that it incorporates both a wavefield and its derivatives in the imaging (Vasconcelos, 2013), thereby reducing uncertainty by mitigating ghost focusing.

We also introduce a new focusing criterion based on the Hough transform (Yip et al., 1992) to better determine both the origin time and the hypocenter of recorded microseismic events. The advantage of the Hough transform is that it conveniently assesses focusing continuously in the time-space domain during back-propagation through spatiotemporal stacking, instead of only at a specific instant in time.

In the paper, we first derive the acoustic representation-theorem-based microseismic-event-localization algorithm and then describe the new focusing criterion. Finally we demonstrate performance with several examples, comparing estimated event locations and their origin time using individual (either pressure or particle velocity fields) and multiple wavefields (both pressure and particle velocity fields).

3.2   Theory

The traditional RTM procedure involves back-propagation of reflection data into the subsurface velocity model followed by an imaging condition (McMechan, 1983). For microseismic event localization, it is the same back-propagation procedure but with reflection data replaced by transmission data. In the next
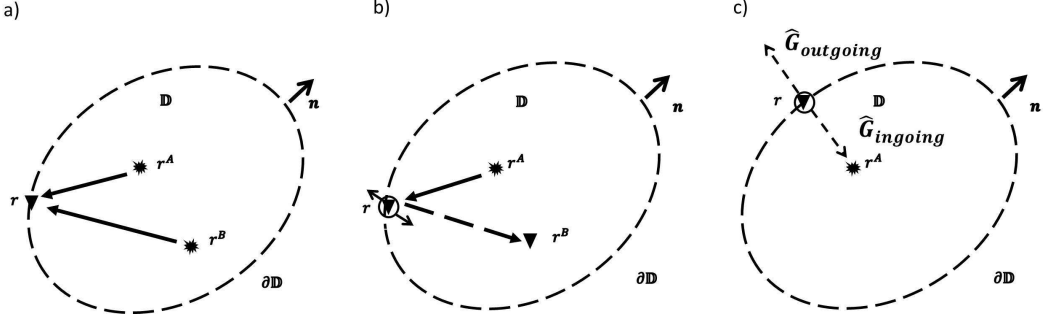
Figure 3.2: Illustration of the domains used for the representation theorem (a) and back-propagation (b and c). The enclosed domain consists of a volume $\mathbb{D}$ with boundary $\partial\mathbb{D}$. The vector $\mathbf{n}$ is the outward unit normal vector to the boundary $\partial\mathbb{D}$. (a) States A and B are wavefields generated by sources located at $\boldsymbol{r}^A$ and $\mathbf{r}^B$. The solid black arrows denote the wave path from source A or B (stars) to the receiver (triangle) located at $\boldsymbol{r}$ on the boundary. (b) $\boldsymbol{r}^A$: the microseismic event location. $\boldsymbol{r}^B$: an arbitrary location in back-propagation image. Solid black arrows : the wave path from the microseismic event (star) to the receiver (triangle) located at $\boldsymbol{r}$ on the boundary. Dashed black arrow : the wave path in the back-propagation. Circle with two solid arrows : both pressure wavefield and its gradient are recorded. (c) Circle with two dashed arrows: when either pressure or particle displacement/velocity wavefields are used, wavefields focusing at true event location $\boldsymbol{r}^A$ is $\hat{G}_{ingoing}$ whereas wavefields focusing at ghost location is $\hat{G}_{outgoing}$.

section we derive the general acoustic representation theorem for wavefield back-propagation.

3.2.1   General Acoustic Representation Theorem

Two independent states A and B are defined in the same 2D spatiotemporal domain $\mathbb{D} \subset \mathbb{R}$, with boundary $\partial\mathbb{D} \subset \mathbb{R}$ (Figure 3.2a). The normal vector pointing outward of $\partial\mathbb{D}$ is represented by $\boldsymbol{n}$. States here simply mean a combination of material parameters, field quantities, source distributions, boundary conditions and initial conditions that satisfy the relevant wave equation (Van Manen et al., 2006). Here we assume that all other parameters in both states are the same except the sources. So, state A and B are expressed by the following first-order wave equations in the space-frequency domain:

State A/B:

$$\begin{cases} \boldsymbol{\nabla}\hat{P}^{A/B}(\boldsymbol{r},\omega) + i\omega\rho(\boldsymbol{r})\hat{\boldsymbol{v}}^{A/B}(\boldsymbol{r},\omega) = \hat{\boldsymbol{f}}^{A/B}(\boldsymbol{r},\omega), \\[12pt] \boldsymbol{\nabla}\cdot\hat{\boldsymbol{v}}^{A/B}(\boldsymbol{r},\omega) + i\omega\kappa(\boldsymbol{r})\hat{P}^{A/B}(\boldsymbol{r},\omega) = \hat{q}^{A/B}(\boldsymbol{r},\omega), \end{cases} \tag{3.1}$$

where A/B means equation 3.1 is valid for both state A and B; $\boldsymbol{\nabla}$ is the spatial gradient operator; hat $\hat{}$ indicates a frequency-domain variable; $\hat{P}^{A/B}$ represents the pressure wavefield of state A/B; ρ is medium density; κ is medium compressibility; $\hat{\boldsymbol{v}}^{A/B}$ denotes particle velocity of state A/B. The source of force $\hat{\boldsymbol{f}}^{A/B}$ and the source of injection rate $q^{A/B}$ are used for sources of state A/B. Then, we apply the complex conjugate to state A of equation 3.1 to get a time-reversed state A (Baysal et al., 1983; Fink et al., 2000; Wapenaar and Fokkema, 2006), yielding

$$\begin{cases} \boldsymbol{\nabla}\hat{P}^{A*}(\boldsymbol{r},\omega) - i\omega\rho(\boldsymbol{r})\hat{\boldsymbol{v}}^{A*}(\boldsymbol{r},\omega) = \hat{\boldsymbol{f}}^{A*}(\boldsymbol{r},\omega), \\[12pt] \boldsymbol{\nabla}\cdot\hat{\boldsymbol{v}}^{A*}(\boldsymbol{r},\omega) - i\omega\kappa(\boldsymbol{r})\hat{P}^{A*}(\boldsymbol{r},\omega) = \hat{q}^{A*}(\boldsymbol{r},\omega). \end{cases} \tag{3.2}$$

A correlation type of representation theorem is derived by calculating the surface integral of the interaction quantity $\boldsymbol{\nabla}\cdot(P^{A*}\boldsymbol{v}^B + P^B\boldsymbol{v}^{A*})$ proposed by De Hoop (1988), whose expression in the frequency domain is given by

$$\begin{aligned} &\int_{\mathbb{D}}\boldsymbol{\nabla}\cdot(\hat{P}^{A*}\hat{\boldsymbol{v}}^B + \hat{P}^B\hat{\boldsymbol{v}}^{A*})dV = \\ &\int_{\mathbb{D}}\left[(\nabla\hat{P}^{A*})\cdot\hat{\boldsymbol{v}}^B + \hat{P}^{A*}\nabla\cdot\hat{\boldsymbol{v}}^B + (\nabla\hat{P}^B)\cdot\hat{\boldsymbol{v}}^{A*} + \hat{P}^B\nabla\cdot\hat{\boldsymbol{v}}^{A*}\right]dV. \end{aligned} \tag{3.3}$$

For brevity, we omit the parameter dependence on frequency ω and spatial location $\boldsymbol{r}$. The surface integral on the left hand side of equation 3.3 can be expressed by a line integral around the enclosed area $\mathbb{D}$ using Stokes' theorem, producing

$$\oint_{\partial \mathbb{D}} \boldsymbol{n} \cdot (\hat{P}^{A*}\hat{\boldsymbol{v}}^B + \hat{P}^B\hat{\boldsymbol{v}}^{A*})dS =$$
$$\int_{\mathbb{D}} \left[(\nabla \hat{P}^{A*}) \cdot \hat{\boldsymbol{v}}^B + \hat{P}^{A*}\nabla \cdot \hat{\boldsymbol{v}}^B + (\nabla \hat{P}^B) \cdot \hat{\boldsymbol{v}}^{A*} + \hat{P}^B\nabla \cdot \hat{\boldsymbol{v}}^{A*} \right] dV, \tag{3.4}$$

where $\boldsymbol{n}$ is the outward unit normal vector to the boundary. Combining equations 3.1 and 3.4, we get

$$\oint_{\partial \mathbb{D}} \boldsymbol{n} \cdot (\hat{P}^{A*}\hat{\boldsymbol{v}}^B + \hat{P}^B\hat{\boldsymbol{v}}^{A*})dS = \int_{\mathbb{D}} \left[\hat{\boldsymbol{f}}^{A*} \cdot \hat{\boldsymbol{v}}^B + \hat{\boldsymbol{f}}^B \cdot \hat{\boldsymbol{v}}^{A*} + \hat{q}^B\hat{P}^{A*} + \hat{q}^{A*}\hat{P}^B \right] dV. \tag{3.5}$$

Equation 3.5 is a general correlation type representation theorem without any boundary conditions and source assumptions. This type of representation is often used for wavefield backward extrapolation to get the characteristics of the seismic source (Aki and Richards, 2002).

In the above derivation, we link two independent wavefields by the general representation theorem without any assumptions on the source types. Next we apply the correlation type representation theorem for time-reversal extrapolation.

3.2.2 Time-reversal extrapolation

First we simplify the correlation type representation by considering assumptions on sources. We arbitrarily choose state A as the physical state, in other words that the recorded wavefield comes from an actual source at true location $\boldsymbol{r}^A$, such as a microseismic event due to a hydraulic fracturing treatment. Then we replace $\hat{P}^{A*}$ with the more general form $\hat{P}^*(\boldsymbol{r}, \boldsymbol{r}^A)$. Then state B is the Green's state representing the wavefield from an impulsive explosive source at location $\boldsymbol{r}^B$ inside the integral area.

We assume a homogeneous medium exists outside of domain $\mathbb{D}$. The source $\hat{q}^B$ is denoted by a Kronecker delta $\delta(\boldsymbol{r} - \boldsymbol{r}^B)$. The pressure wavefield corresponding to this source is the Green's function $\hat{G}(\boldsymbol{r}, \boldsymbol{r}^B)$. State B is also called the Green's state. For simplicity, we assume the volume source of force

49

$\hat{f}$ in both states equals zero (Wapenaar and Fokkema, 2006). The particle velocity in both states can be written in the form of a pressure field, as $\hat{v}^{A*} = \frac{1}{i\omega\rho}\nabla\hat{P}^*(r, r^A)$ and $\hat{v}^B = -\frac{1}{i\omega\rho}\nabla\hat{G}(r, r^B)$ (Curtis and Halliday, 2010). Moreover, both states A and B share the same medium properties within the boundary, giving a definition of state A and B,

State A:

$$
\begin{cases}
\nabla\hat{P}^*(r, \omega) = i\omega\rho(r)\hat{v}^*(r, \omega), \\[2mm]
\nabla \cdot \hat{v}^*(r, \omega) - i\omega\kappa(r)\hat{P}^*(r, \omega) = \hat{s}^*(\omega)\hat{\delta}(r - r^A),
\end{cases}
\tag{3.6}
$$

State B:

$$
\begin{cases}
\nabla\hat{G}(r, \omega) = -i\omega\rho(r)\hat{v}_G(r, \omega), \\[2mm]
\nabla \cdot \hat{v}_G(r, \omega) + i\omega\kappa(r)\hat{G}(r, \omega) = \hat{\delta}(r - r^B),
\end{cases}
\tag{3.7}
$$

where $\hat{s}^*(\omega)$ represents the source signature in the frequency domain and $\hat{v}_G(r, \omega)$ represents the particle velocities corresponding to the Green's state B.

Under these assumptions, we get a further simplified correlation type representation theorem, given by

$$
\oint_{\mathbb{D}} \hat{P}^*(r, r^A)\delta(r - r^B)dV + \oint_{\mathbb{D}} \hat{s}^*(\omega)\hat{G}(r, r^B)\hat{\delta}(r - r^A)dV =
$$
$$
-\int_{\partial\mathbb{D}} n \cdot \left(-\hat{G}(r, r^B)\frac{1}{i\omega\rho}\nabla\hat{P}^*(r, r^A) + \hat{P}^*(r, r^A)\frac{1}{i\omega\rho}\nabla\hat{G}(r, r^B)\right) dS,
\tag{3.8}
$$

where the first part on the left hand side equals to $\hat{P}^*(r^B, r^A)$ according to the delta function property and $\hat{G}(r, r^B)$ is replaced with $\hat{G}(r^B, r)$ through source-receiver reciprocity(Wapenaar and Fokkema, 2006).

The second term on the left hand side of equation 3.8 is called an acoustic sink. During time-reversal it ensures that a wavefield collapsed onto its source location disappears. Normally it cannot be calculated directly, so the converged

wavefield diverges again (Fink et al., 2000). Therefore a focusing criterion is generally used, such as the Hough transform in the next section, to determine wavefield convergence onto the source location.

The left-hand-side of equation 3.8 can be written as $\hat{P}_{TR}^* = \hat{P}^*(\boldsymbol{r}^B, \boldsymbol{r}^A) + \oint_{\mathbb{D}} \hat{s}^*(\omega)\hat{G}(\boldsymbol{r}^B, \boldsymbol{r}^A)dV$ for simplicity, where $\hat{P}_{TR}^*$ is the time-reversed pressure wavefield without acoustic sink. Then, we get the time-reversed extrapolation formula, given by

$$
\begin{aligned}
\hat{P}_{TR}^*(\boldsymbol{r}^B, \boldsymbol{r}^A) = \\
- \oint_{\partial\mathbb{D}} \boldsymbol{n} \cdot (-\hat{G}(\boldsymbol{r}^B, \boldsymbol{r})\frac{1}{\boldsymbol{i}\omega\rho}\boldsymbol{\nabla}\hat{P}^*(\boldsymbol{r}, \boldsymbol{r}^A) + \hat{P}^*(\boldsymbol{r}, \boldsymbol{r}^A)\frac{1}{\boldsymbol{i}\omega\rho}\boldsymbol{\nabla}\hat{G}(\boldsymbol{r}^B, \boldsymbol{r}))dS.
\end{aligned}
\tag{3.9}
$$

Figure 3.2b illustrates the physical meaning of equation 3.9. A circle connected with arrows means both the pressure wavefield $P(\boldsymbol{r}, \boldsymbol{r}^A)$ and its gradient $\boldsymbol{\nabla}P(\boldsymbol{r}, \boldsymbol{r}^A)$ are recorded on the boundary $\partial\mathbb{D}$ from the microseismic event located at $\boldsymbol{r}^A$. The two types of wavefields are back-propagated separately using a given velocity profile. The pressure wavefield at arbitrary location $\boldsymbol{r}^B$ within the boundary is calculated through combination of the back-propagated particle velocity $\hat{\boldsymbol{v}}^*(\boldsymbol{r}, \boldsymbol{r}^A) = \frac{1}{\boldsymbol{i}\omega\rho}\boldsymbol{\nabla}\hat{P}^*(\boldsymbol{r}, \boldsymbol{r}^A)$ and pressure wavefield $\hat{P}^*(\boldsymbol{r}, \boldsymbol{r}^A)$. The location with the highest focus is considered as the most likely possible event location assuming a relatively correct velocity model.

3.2.3 Ghost focus cancellation

Traditional reverse time extrapolation only injects direct arrivals of particle displacement/velocity wavefields. Seismic waves focus not only at the true event location but also on a false location especially for limited borehole observation geometries. We call the false source location a ghost focus because it does not exist in reality.

In the following, we prove that the representation-theorem-based reverse time extrapolation can remove the ghost focus as long as a correct normal vector $\boldsymbol{n}$ is chosen. We first write $\hat{G}(\boldsymbol{r}^B, \boldsymbol{r}) = \hat{G}_{in}(\boldsymbol{r}^B, \boldsymbol{r}) + \hat{G}_{out}(\boldsymbol{r}^B, \boldsymbol{r})$, where the subscripts *in* and *out* refer to waves propagating towards true and false event's

locations from the source at $\boldsymbol{r}$ on $\partial\mathbb{D}$ (Figure 3.2c). $\hat{P}^*(\boldsymbol{r}, \boldsymbol{r}^A)$ is then written as $\hat{P}^*_{in}(\boldsymbol{r}, \boldsymbol{r}^A)$, denoting that the seismic records come from true microseismic event. Equation 3.9 becomes

$$
\begin{aligned}
\hat{P}^*_{TR}(\boldsymbol{r}^B, \boldsymbol{r}^A) = &- \oint_{\partial\mathbb{D}} \boldsymbol{n} \cdot ((-\hat{G}_{in}(\boldsymbol{r}^B, \boldsymbol{r}) - \hat{G}_{out}(\boldsymbol{r}^B, \boldsymbol{r})) \frac{1}{\boldsymbol{i}\omega\rho} \boldsymbol{\nabla} \hat{P}^*_{in}(\boldsymbol{r}, \boldsymbol{r}^A) \\
&+ \hat{P}^*_{in}(\boldsymbol{r}, \boldsymbol{r}^A)(\frac{1}{\boldsymbol{i}\omega\rho} \boldsymbol{\nabla} \hat{G}_{in}(\boldsymbol{r}^B, \boldsymbol{r}) + \frac{1}{\boldsymbol{i}\omega\rho} \boldsymbol{\nabla} \hat{G}_{out}(\boldsymbol{r}^B, \boldsymbol{r}))) dS.
\end{aligned}
\tag{3.10}
$$

We approximate the normal derivatives of the Green's function with their high frequency approximations by replacing $\boldsymbol{\nabla}$ with $\mp \boldsymbol{i}k(\boldsymbol{r}) \|cos(\alpha(\boldsymbol{r}))\|$, where $k(\boldsymbol{r})$ is the local wave number at $\partial\mathbb{D}$ and $\alpha(\boldsymbol{r})$ is the angle between pertinent rays and the normal on $\partial\mathbb{D}$, assuming the medium is smooth in the vicinity around $\partial\mathbb{D}$ (Wapenaar and Fokkema, 2006). The ingoing waves propagating towards the true event location get a minus sign in the high frequency approximation, whereas the outgoing waves propagating towards the false event location have a plus sign. Equation 3.10 then becomes

$$
\begin{aligned}
\hat{P}^*_{TR}(\boldsymbol{r}^B, \boldsymbol{r}^A) = &- \oint_{\partial\mathbb{D}} ((-\hat{G}_{in}(\boldsymbol{r}^B, \boldsymbol{r}) \frac{k(\boldsymbol{r}) \|cos(\alpha_A(\boldsymbol{r}))\|}{\omega\rho} \hat{P}^*_{in}(\boldsymbol{r}, \boldsymbol{r}^A) \\
&- \hat{G}_{out}(\boldsymbol{r}^B, \boldsymbol{r}) \frac{k(\boldsymbol{r}) \|cos(\alpha_A(\boldsymbol{r}))\|}{\omega\rho} \hat{P}^*_{in}(\boldsymbol{r}, \boldsymbol{r}^A) \\
&- \hat{P}^*_{in}(\boldsymbol{r}, \boldsymbol{r}^A) \frac{k(\boldsymbol{r}) \|cos(\alpha_B(\boldsymbol{r}))\|}{\omega\rho} \hat{G}_{in}(\boldsymbol{r}^B, \boldsymbol{r}) \\
&+ \hat{P}^*_{in}(\boldsymbol{r}, \boldsymbol{r}^A) \frac{k(\boldsymbol{r}) \|cos(\alpha_B(\boldsymbol{r}))\|}{\omega\rho} \hat{G}_{out}(\boldsymbol{r}^B, \boldsymbol{r}))) dS,
\end{aligned}
\tag{3.11}
$$

where angle $\alpha_A(\boldsymbol{r})$ is for the true event at $\boldsymbol{r}^A$ and angle $\alpha_B(\boldsymbol{r})$ for an arbitrary location $\boldsymbol{r}^B$. Stationary phase analysis shows that the contribution to the integral comes from those stationary points on $\partial\mathbb{D}$, at which the absolute cosines of $\alpha_A(\boldsymbol{r})$ and $\alpha_B(\boldsymbol{r})$ are identical (Schuster et al., 2004; Wapenaar et al., 2004; Wapenaar and Fokkema, 2006; Snieder, 2004; Snieder et al., 2006). Besides, the signs of the first and the third terms are identical, but reversed for the second and forth terms. In other words, the back-propagated particle velocity and pressure fields have the same polarities when they are propagating towards the

true location, but an opposite polarities in the directions of the ghost location. Thus, the second and forth terms of equation 3.10 cancel each other, leaving the first and third terms, meaning the waves only focus at the true event location when using the representation-theorem-based reverse time extrapolation, giving

$$
\begin{aligned}
\hat{P}_{TR}^*(\boldsymbol{r}^B, \boldsymbol{r}^A) = - \oint_{\partial \mathbb{D}} \boldsymbol{n} \cdot (-\hat{G}_{in}(\boldsymbol{r}^B, \boldsymbol{r}) \frac{1}{\boldsymbol{i}\omega\rho} \boldsymbol{\nabla} \hat{P}_{in}^*(\boldsymbol{r}, \boldsymbol{r}^A) \\
+ \hat{P}_{in}^*(\boldsymbol{r}, \boldsymbol{r}^A)(\frac{1}{\boldsymbol{i}\omega\rho} \boldsymbol{\nabla} \hat{G}_{in}(\boldsymbol{r}^B, \boldsymbol{r})))dS.
\end{aligned}
\tag{3.12}
$$

3.2.4   Implementation

For implementation we use the discrete equivalent of equation 3.9 given by

$$
\begin{aligned}
\hat{P}_{TR}^*(\boldsymbol{r}^B, \boldsymbol{r}^A) = \\
- \sum_{\boldsymbol{r}} \boldsymbol{n_r} \cdot (-\hat{G}(\boldsymbol{r}^B, \boldsymbol{r}) \frac{1}{\boldsymbol{i}\omega\rho} \boldsymbol{\nabla} \hat{P}^*(\boldsymbol{r}, \boldsymbol{r}^A) + \hat{P}^*(\boldsymbol{r}, \boldsymbol{r}^A) \frac{1}{\boldsymbol{i}\omega\rho} \boldsymbol{\nabla} \hat{G}(\boldsymbol{r}^B, \boldsymbol{r})),
\end{aligned}
\tag{3.13}
$$

where $\boldsymbol{n_r}$ is the outward pointing normal of the integration boundary. The product in the first term on the right-hand side represents the forward modeling process in the frequency domain. A wavefield $G(\boldsymbol{r}^B, \boldsymbol{r})$ predicted at location $\boldsymbol{r}^B$ by an explosive monopole source located at $\boldsymbol{r}$ is multiplied with the time-reversed spatial gradient of the observed pressure wavefield denoted by $\frac{1}{\boldsymbol{i}\omega\rho} \boldsymbol{\nabla} \hat{P}^*(\boldsymbol{r}, \boldsymbol{r}^A)$. The product in the second term on the right hand side also represents a forward modeling process in frequency domain. $\boldsymbol{\nabla} \hat{G}(\boldsymbol{r}^B, \boldsymbol{r})$ represents the predicted wavefield at $\boldsymbol{r}^B$ from a dipole source at location $\boldsymbol{r}$, convolved with the time-reversed observed pressure wavefield $\hat{P}^*(\boldsymbol{r}, \boldsymbol{r}^A)$.

Figure 3.3 shows the processing flow of representation theorem based time-reversal extrapolation. For simplicity we explain the problem under 2D implementation. Practical issues when extending to 3D will be introduced in a separate section. Both the pressure wavefield and two components of the particle velocities are recorded. Before reverse-time propagation, the data are first bandpass filtered to the range of interest. Then the processed, complex

conjugates of the pressure and two-component particle-velocity wavefields are multiplied with respectively the dipole and monopole Green's functions. This corresponds to convolution of the time-reversed, observed wavefields with the appropriate Green's functions in the time domain. After both results are combined, a normal vector is used to control the contribution from each component (x and z). The choice of normal vector $\boldsymbol{n_r}$ depends on the predefined integration boundary.

In practice, we use the observed processed pressure wavefield at each receiver, reverse its time axis and then forward propagate the resulting data into the medium using a finite difference algorithm. Likewise, we back propagate the observed two-component velocity field. The final image is then obtained by stacking all corresponding wavefields for all receivers. This allows us to back-propagate only the pressure or two-component wavefields individually but also stack their combined images. A focusing criterion, described next is applied to the wavefield at each time slice to determine the origin time and hypocenter of the microseismic event.

3.2.5 Focusing criterion

A source focusing criterion is needed due to the absence of an acoustic sink in equation 3.9 and 3.13. In traditional reverse time imaging, the zero-lag cross-correlation imaging condition determines focusing. But for microseismic event localization, we only have a receiver wavefield but no known source wavefield. The most straightforward focusing criteria use amplitude, energy or semblance thresholding to determine possible event locations and origin times (Artman et al., 2010).

We use a modification of the Hough transform (Yip et al., 1992) to determine wavefield focusing. In essence, we assume that the wavefront is approximately circular around the source location point just before and after focusing, and maximum energy concentration occurs at the origin time and location (Figure 3.4). Thus as in Figure 3.4, if we sum the energy on the wavefront at time $t_0 - \Delta t$ and $t_0 + \Delta t$, as well as the energy at source location at time t_0, we should get a maximum value compared to the summation value at different locations

Data Pressure Wavefield   X Component of Particle Velocity   Z Component of Particle Velocity

Preprocessing   Bandpass Filtering

Processed Pressure Wavefield   Processed X Component of Particle Velocity   Processed Z Component of Particle Velocity

Convolution with Dipole Green's Function   Convolution with Monopole Green's Function

$$\hat{P}^*(\boldsymbol{r}, \boldsymbol{r}^A)\frac{1}{i\omega\rho}\nabla\hat{G}(\boldsymbol{r}^B, \boldsymbol{r})$$ $$\hat{G}(\boldsymbol{r}^B, \boldsymbol{r})\frac{1}{i\omega\rho}\nabla\hat{P}^*(\boldsymbol{r}, \boldsymbol{r}^A)$$

Normal Vector

Stack all receivers

Time-reversed Wavefield

Focusing Criterion

Figure 3.3: Processing flow of representation theorem based time-reversal extrapolation.
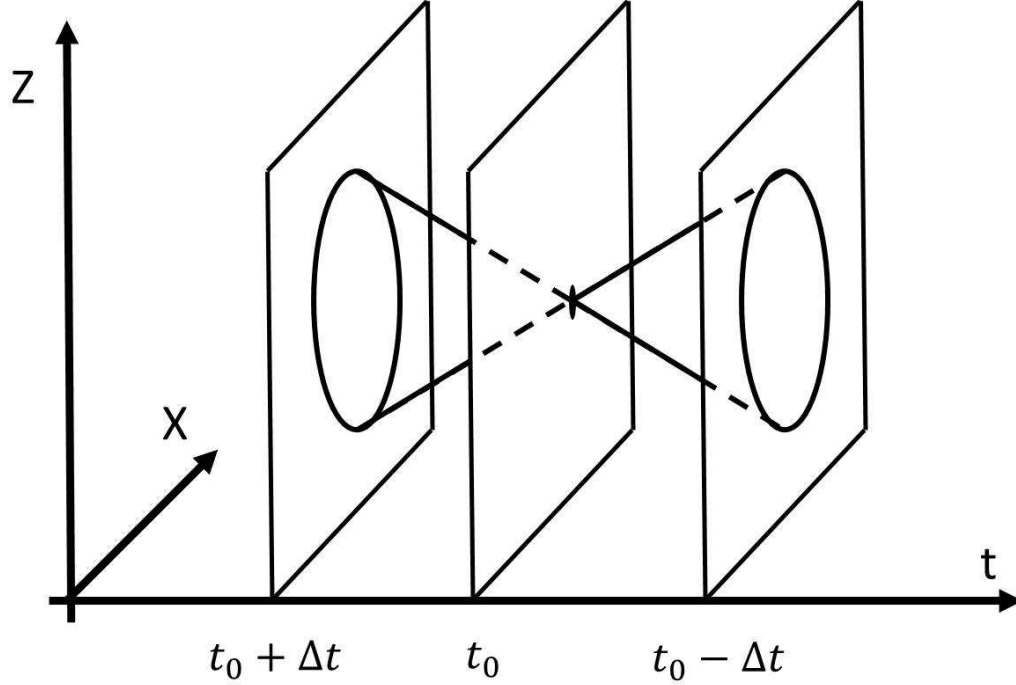
Figure 3.4: Wavefront in the back-propagation images. z and x are spatial coordinates. t is back-propagation time. The black dot in the center time slice denotes source location and t_0 is source origin time. Circles: wavefront with radius $r_{\delta t}$ right before and after origin time t_0. During back-propagation, the wavefront collapses at the source location and then diverges again due to the lack of an acoustic sink.

and times. The modified Hough transform turns a back-propagated pressure wavefield image into a summation image in the spatiotemporal domain, from which we extract the source origin time and location. We name this summation image the Hough map. A back-propagated pressure wavefield image is called the wavefield map for comparison.

The first step is to do spatially circular summation. We sum the envelope of the back-propagated pressure wavefield P_{TR}^* along circles with local radius R around grid points $\boldsymbol{r}_x$ at time instance t_H, that is

$$P_H(\boldsymbol{r}_x, t_H) = \sum_{\boldsymbol{r}} Evn(P_{TR}^*(\boldsymbol{r}, t_H)), \qquad (3.14)$$

where $\boldsymbol{r}$ satisfies $|\boldsymbol{r} - \boldsymbol{r}_x| = R$ and Evn represents the envelope of a time series. Grid points $\boldsymbol{r}_x$ represent generally a coarser grid than that used for the actual

wave simulation. The time axis t_H is sampled every Δt seconds. Variable Δt is a prespecified time interval, such that the largest radii become approximately equal to half a dominant wavelength. Radius R is equal to local velocity $V(\boldsymbol{r}_x)$ times interval Δt. For small time intervals Δt, the actual wavefronts become circles with radii R. This way, we turn the back-propagation image P^*_{TR} into a summation image P_H.

The next step is to do a temporal summation, which combines summed image P_H with back-propagation image P^*_{TR}, yielding a Hough map using

$$P_H^{sum}(\boldsymbol{r}_x, t_H) =$$
$$P_H(\boldsymbol{r_x}, t_H - \Delta t) + P_H(\boldsymbol{r_x}, t_H + \Delta t) + |(Evn(P^*_{TR}(\boldsymbol{r_x}, t_H)))|. \tag{3.15}$$

Hough map P_H^{sum} is evaluated for determining the most likely source location and origin time.

We then assume that only a single microseismic event could occur at each time instant t_H. We save the spatial coordinates of the maximum value in the Hough map as a function of time t_H and compute its shortest distance to the receivers. This greatly condenses the information and allows us to select the most likely source locations and origin times without having to save either the Hough map or the back-propagation image at all time instances.

Next, a magnitude threshold $\mathbb{T}_M$ is set to determine the most likely source positions and origin times. A threshold $\mathbb{T}_D$ for the minimum distance to the receivers is also sometimes needed. In the back-propagation, the highest magnitude of P_H^{sum} may appear at locations near the receivers due to uncancelled noise and signal interferences. These points thus generally represent artefacts and have to be excluded from the selection pool. Finally, the local maximum above the magnitude threshold in both time and position is extracted to find the most likely source positions and origin times.

3.2.6 3D Application

Implementation of the representation-theorem-based reverse time extrapolation becomes more complex in a 3D setting. Figure 1.1 shows two common

observation systems for microseismic monitoring, namely surface and borehole acquisitions. Either has its own advantages and uncertainties when applying our proposed method.

Similar to conventional reverse time migration, a large surface array has a better coverage of microseismic events, producing located microseismic events with higher horizontal resolution. In this case the normal vector is perpendicular to the 2D plane spanned by the receivers, in other words points upward (Figure 1.1).

Borehole observations are more challenging for reverse time extrapolation. Normally less than 20 geophones are used in a borehole scenario, leading to a very limited aperture. Also, no immediate choice of normal vector is available for this acquisition setup for a priori unknown event locations because an infinite number of 2D plane pass through a 1D borehole. Fortunately, we obtain a range of possible normal vectors from the borehole geometry and the locations of perforation shots (Figure 3.1b). First the normal vectors are always perpendicular to the borehole. Only the azimuth of the normal vectors are to be determined. The range of azimuths can be further narrowed down by first locating several events for each hydraulic fracturing stage using ray-based methods, which provides a more appropriate range of azimuths before applying the representation-theorem-based reverse time extrapolation. The final choice of the azimuth of normal vector then ultimately varies with the actual acquisition geometry. If multiple boreholes exist, normals with back-azimuths pointing to the centroid of the expected microseismic cloud will likely work well. Likewise, for strongly deviated wells a normal perpendicular to the well with back-azimuth pointing to the cloud's centroid should suffice. It is only in case of a single horizontal or vertical well that the choice of the optimal azimuth becomes truly challenging. These are the least optimal acquisition geometries for wavefield-extrapolation based event localization. One might have to take recourse to automated polarization analyses (De Meersman et al., 2006) for each event to estimate the azimuth of the required normal, with the possible advantage that only 2D planes are needed for wavefield extrapolation.

3.3 Examples

In this section, we apply the representation-theorem-based reverse time extrapolation to synthetic examples using deviated borehole acquisitions as a challenging test situation. We use second order in time and fourth order in space finite differences to do forward modeling and back extrapolation. We smooth the velocity model during the back-propagation to (1) mimic a partially unknown velocity field and (2) prevent the generation of reflections. We wish to explore the possibilities of this method in different velocity structures, namely a layered-model and the Marmousi velocity model. A homogeneous velocity example can be found in Li and Van der Baan (2014).

3.3.1 Four-layer model

A deviated borehole is set in a four-layer velocity model with 43 receivers (Figure 3.5a), providing a good coverage of signal. The velocity of each layer can be found in Figure 3.5a. The source is an explosive source with a Ricker wavelet with a peak frequency of 60 Hz, located on the right of the well with coordinates (X, Z) of (650m , 530m). It simulates an event at origin time 0.02 s. Both the pressure and particle velocities in the horizontal and vertical directions are measured at each receiver, with total recording time of 0.2 s. The numerical simulation grid spacing is 2.8 m with 0.18 ms time intervals. The synthetic, Gaussian white noise contaminated data are shown in Figure 3.6.

Next we inject three different combinations of the total wavefields using equation 3.13, namely (1) using only the pressure data, (2) both particle velocity fields but not pressure, (3) using both pressure and velocity fields into a smoothed version of the exact velocity model (Figure 3.5b). The normal vectors are perpendicular to the well, pointing to the left side. Figure 3.7 displays the back-propagated source image for all three cases. Figure 3.7a is the case when we only back-propagate the pressure data. Two high energy images appear on both sides of the well at t=0.2s. The left location is a ghost focusing, whereas the right one is the true source location. Even though the energy of the ghost focus is slightly less than the true focus, it still bring ambiguity to the interpretation for the true location of the microseismic event. Figure 3.7b

is the case when we only back-propagate the two-component particle velocity data. The focusing features in this case are similar to the previous case, only the focuses have an opposite polarity from the previous case. When all data are back-propagated, the energy of the ghost focus is significantly reduced. Only the true event location stands out clearly (Figure 3.7c). In addition, the combination of both pressure and velocity fields for microseismic event localization leads to an improved SNR in the final image (3.7c), in particular around the receiver area, compared with the use of individual wavefields (3.7a,b).

We then test the ability of the focusing criterion for origin time and event location detection when both pressure and velocity fields are used (the combination 3). During back-propagation, we apply equations 3.14 and 3.15 to the wavefield map P_{TR}^* to get the Hough map P_H at time t_H. The back-propagation grid spacing is 1.25 m and time intervals for focusing criterion is 2.8 ms. We then save the spatial coordinates of the maximum value in both the Hough map P_H and the envelope of the wavefield P_{TR}^* as a function of time t_H and compute its shortest distance to the receivers before apply threshold $\mathbb{T}_M$ and $\mathbb{T}_D$ (Figure 3.8). Maxima with distances less than 200 m are discarded (Figure 3.8a,c). The local maximum in the Hough map occurs at 0.02 s at the true origin time (Figure 3.8b), whereas the maximum in the wavefield envelope happens at 0.03 s (Figure 3.8d). Moreover, the Hough criterion is better behaved in the sense that the variations are smoother and with a larger dynamic range, indicating that it is less sensitive to noise and imaging artefacts. Figure 3.9 displays the Hough map P_H and the envelope of the wavefield map P_{TR}^* at their respective detected origin times, showing that the Hough map is indeed more stable and accurate with less imaging artefacts.

3.3.2   Marmousi acoustic model

Next we test the representation-theorem-based reverse time extrapolation and focusing criterion under a more realistic situation with a complex structure and a more complex source. In this example, the synthetic seismic records are created using the true Marmousi model (Figure 3.10a) with a Double-Couple (DC) source. The synthetic data from 14 borehole receivers are shown in Figure
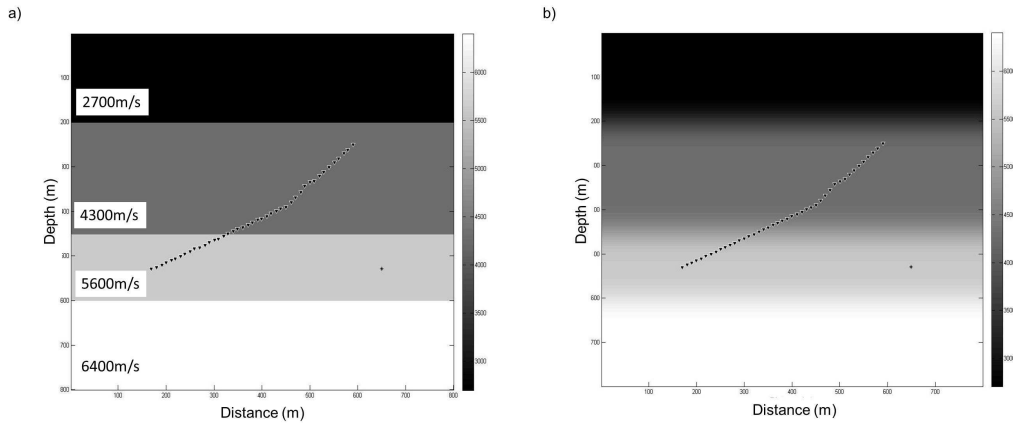
Figure 3.5: 2D acoustic layered velocity model. Red up-side-down triangles: receivers. Blue cross: source. a: true layered velocity model, b: smoothed velocity model.
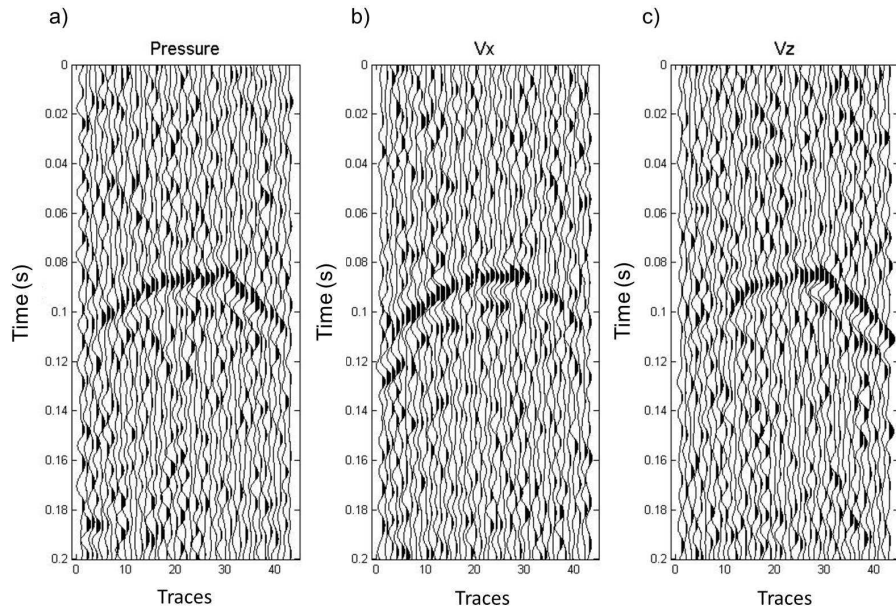
Figure 3.6: Seismic records for four-layer model including pressure and two-component particle velocity wavefields.
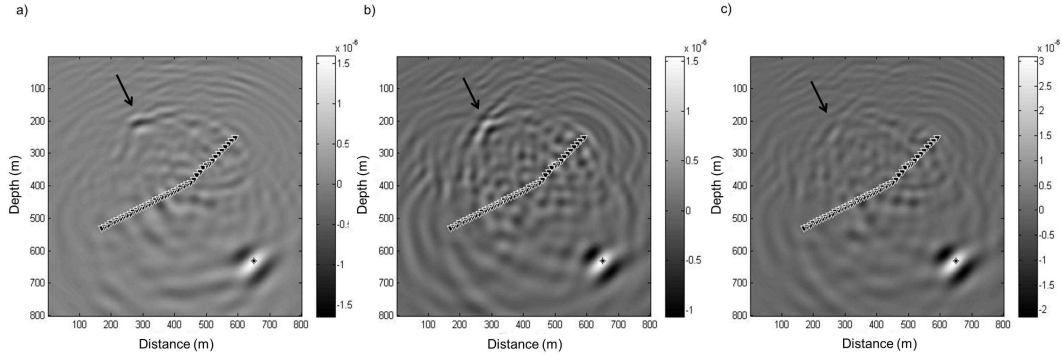
Figure 3.7: Comparison of the back-propagated pressure wavefield via three data combinations when using smoothed layered velocity model. (a) pressure field only. (b) particle velocity fields only. (c) both pressure field and particle velocity fields. The ghost location focusings (pointed by black arrows) exist in the first two cases; The ghost focusing is significantly suppressed in the third case when we combine all data.

3.11. A DC source with a Ricker wavelet with a dominant frequency of 10 Hz is located on the right of the well with coordinates (X, Z) of (6500m , 2500m). Its origin time is at 0.1 s. The simulation grid spacing is 24 m with 1.8 ms time interval.

We apply the focusing criterion in this example to a smoothed version of the exact velocity model (Figure 3.10b) for back-propagation with both pressure and velocity fields (combination 3 in the previous example). The time interval for focusing criterion is 12.6 ms. Figures 3.12 displays the results for the focusing criteria using either the Hough map or the envelope of the wavefield in case of the smoothed velocity model, similar to Figure 3.8. For simplicity, we only show the magnitude points with reasonable distance to receivers. The Hough criterion predicts an origin time of 0.1 s and the envelope maximum occurs at 0.22 s. The appearance of noise introduces large error to the origin time determined by the envelope of the wavefield (Figure 3.12b), whereas an accurate origin time is provided when using the Hough map based focusing criterion (Figure 3.12a). Figure 3.13 shows the comparison of back-propagation images for corresponding origin times derived from the Hough criterion (Figure 3.13a) and the envelope maximum (Figure 3.13b). The envelope maximum fails to locate the source properly because the radiation pattern of the DC source makes the magnitude of focus equal to zero. On the contrary, the Hough map

62
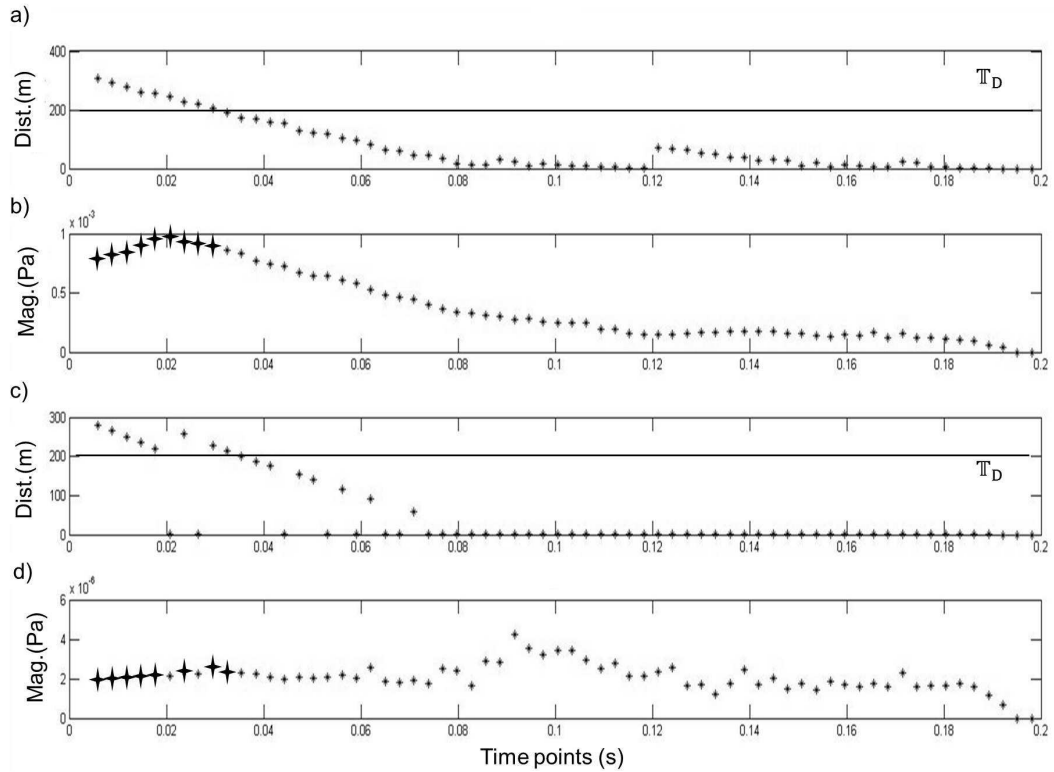
Figure 3.8: Event detection criteria using maxima in Hough map (a and b) or maxima in wavefield envelopes (c and d) for layered velocity model. (a) and (c): Distance of detected maximum to nearest receiver as a function of time. A minimum threshold $\mathbb{T}_D$ of 200m is set (black solid line). All smaller distances are discarded. (b) and (d): Maximum value as a function of time. Black stars: maxima exceeding minimum distance. Local Hough maximum (b) is close to true origin time of 0.02 s, contrary to maximum of wavefield envelope (d). Extracted maxima from the Hough map (b) also display smoother variations with a larger dynamic range than those from the wavefield envelope (d).
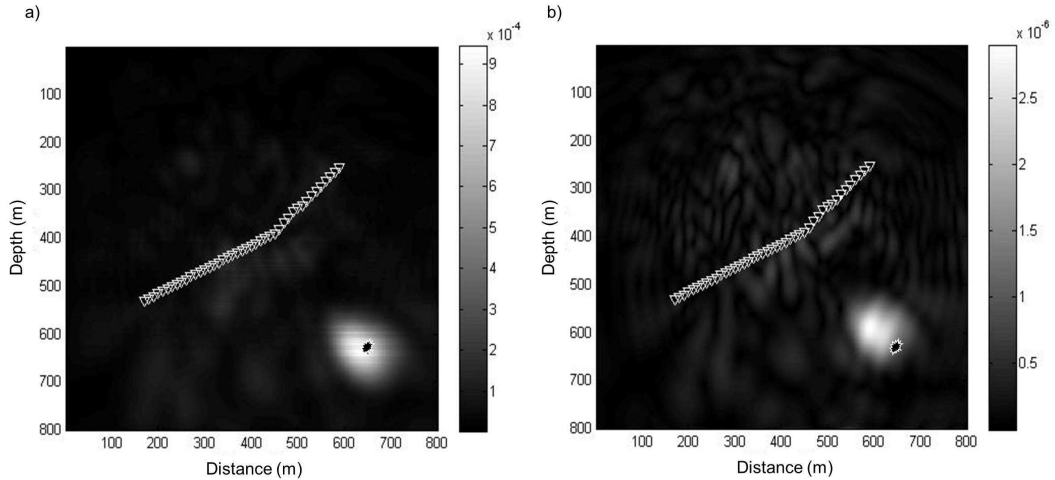
Figure 3.9: Comparison of the Hough map and envelope of the wavefield at respective estimated origin times for the layered velocity model. (a) Hough map at 0.02 s; (b) Wavefield envelope at 0.03 s. Black star: True event location.

leads to a more accurate event location, with less imaging artefacts.

3.4   Discussion

In this paper we have shown the advantages of combining the pressure and three-component particle displacement/velocity wavefields in microseismic event localization. Therefore, we advocate combined usage of hydrophone and three-component receivers in microseismic monitoring. The spatial derivatives of the pressure wavefield contain directional information which can aid in the back-propagation process. The acoustic-representation-theorem based reverse time extrapolation naturally utilizes the two types of data. Moreover, all wavefields are back propagated to the source location independently and combined in the final step. The two types of wavefields generate an opposite polarity image at the ghost location and the same polarity image at the true event location. By adding the two wavefields, the opposite polarization portions cancel each other whereas the energy at true location is boosted. This suppresses image artefacts compared with implementations when only the pressure wavefield or the spatial gradients are used. Moreover, the particle velocity and pressure records may have different signal-to-noise ratios, e.g., due to contamination with different
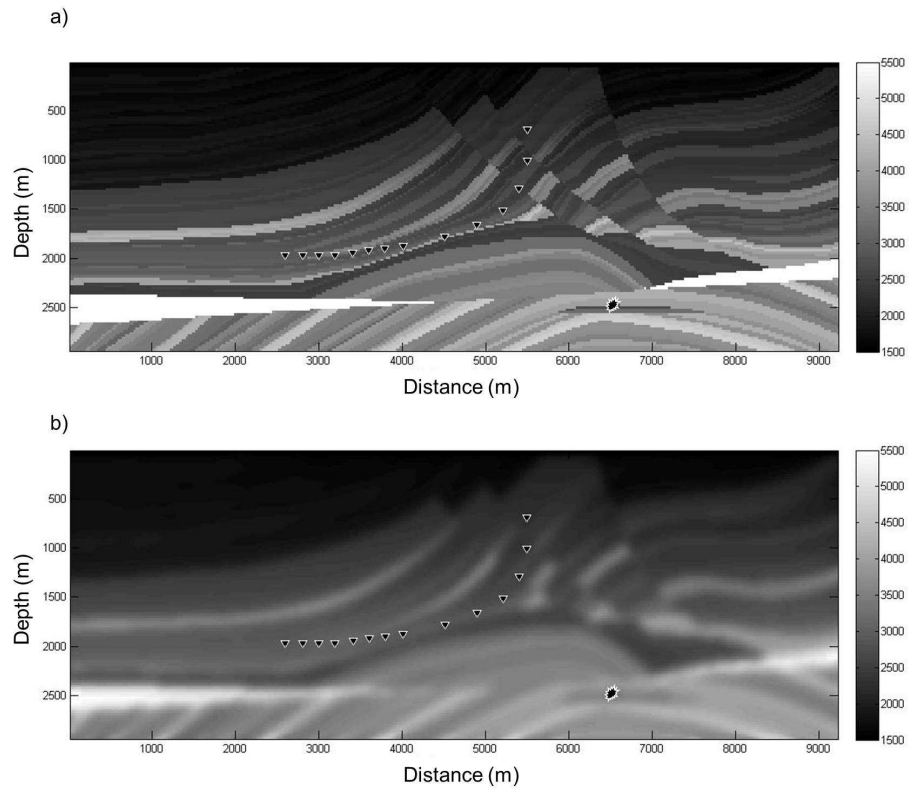
Figure 3.10: 2D acoustic Marmousi velocity model. Red up-side-down triangles: receivers. Red star: source. From upper to bottom: (a) actual velocity model, (b) smoothed velocity model. Velocities are in m/s.
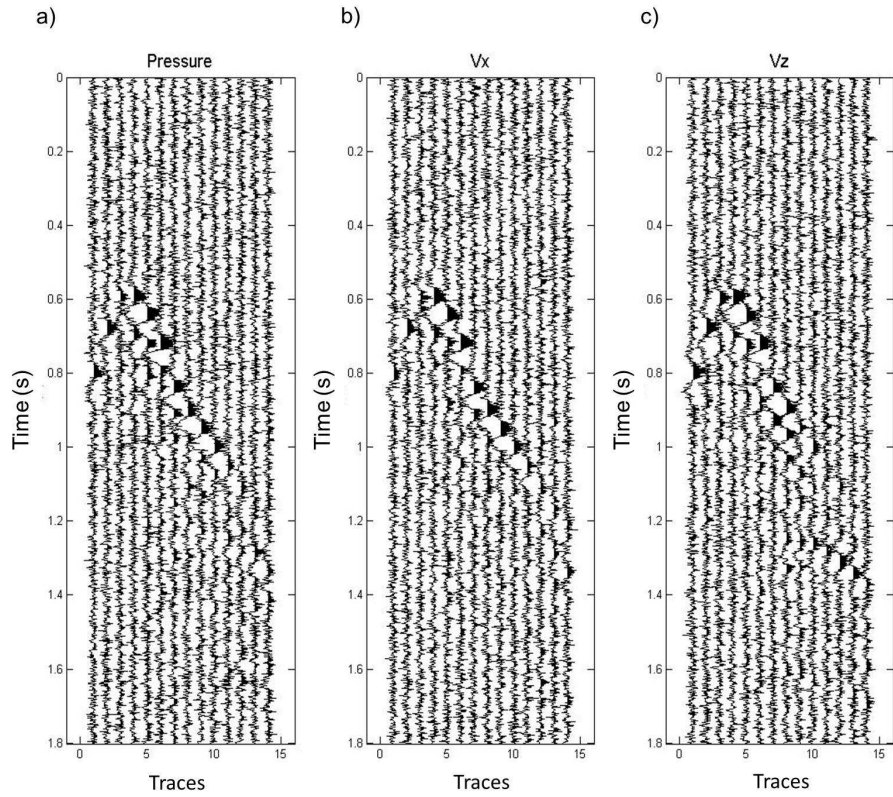
Figure 3.11: Synthetic noisy seismograms for Marmousi test model. The complex waveforms are due to the complex velocity structure. a: Pressure field records. b and c: X and Z components of particle velocity fields records.
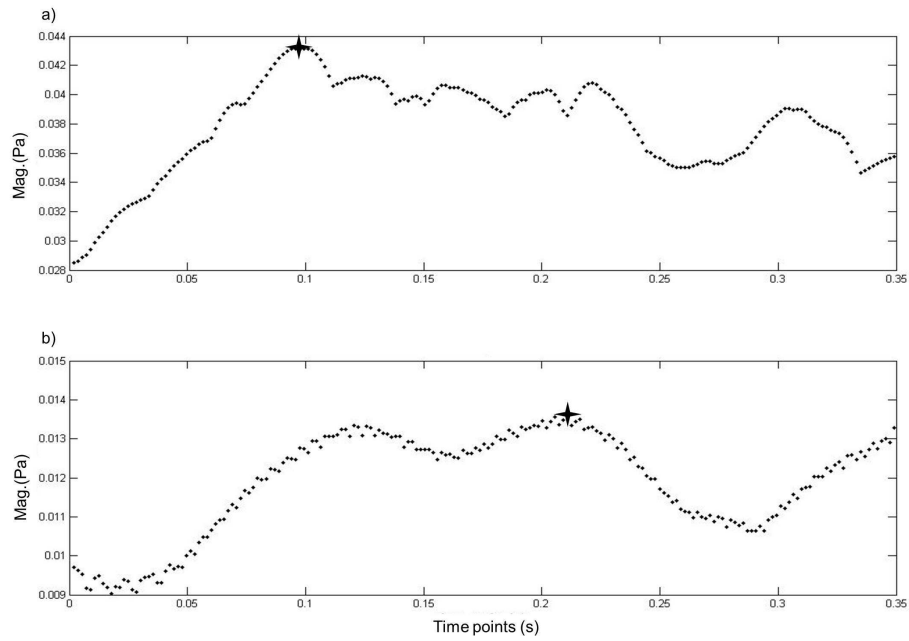
Figure 3.12: Zoom in from time 0s to 0.35s for event detection criteria using maxima in Hough map (a) or maxima in wavefield envelopes (b) for smoothed Marmousi velocity model. See Figure 7 for labels. Detected origin times are respectively (a) 0.1 s (Hough map) and (b) 0.22 s (wavefield envelope). True origin time is at 0.1 s.
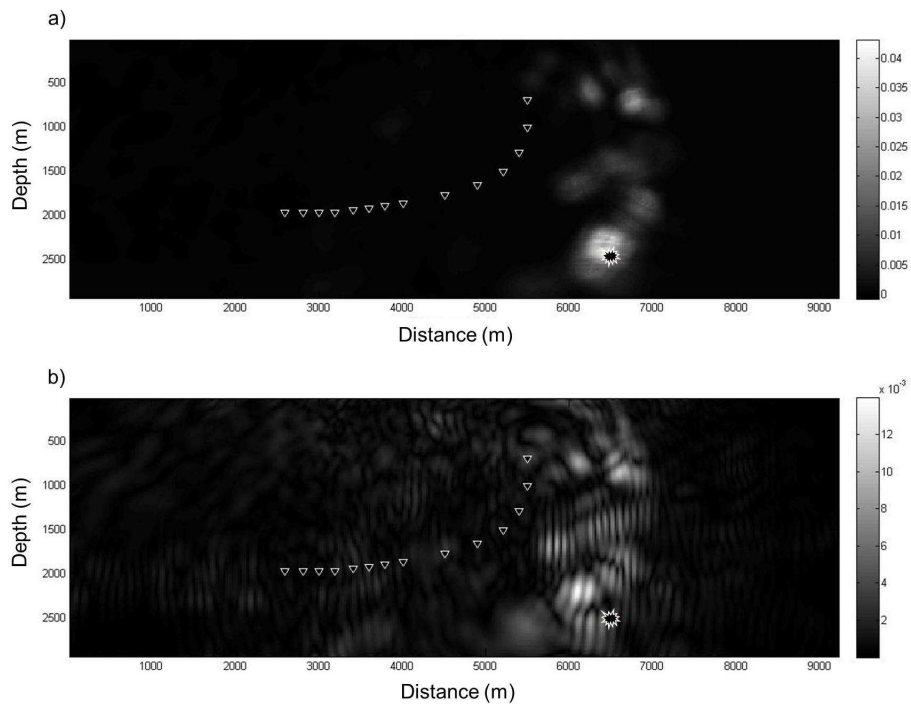
Figure 3.13: Comparison of the Hough map and envelope of the wavefield at respective estimated origin times for the smooth Marmousi velocity model. (a) Hough map at 0.1 s; (b) Wavefield envelope at 0.22 s. Black star: True event location.

types of noise or different bandwidth sensitivities. Judicious weighting may thus enhance the final imaging quality of the reconstructed combined wavefields as well as the Hough images even further compared to the images from the individual wavefields. The combined use of pressure and particle velocity wavefields may equally improve migration of reflection seismic data (Vasconcelos, 2013).

The back-propagated wavefield does not collapse to a point in our tests due to the limited acquisition aperture but leaves an area with high energy concentration. This area provides the uncertainty in event location. A visual comparison for homogeneous and complex velocity models shows that the anticipated uncertainty in event locations using the proposed method is similar to those from travel-time based methods as obtained using the sensitivity analysis of Feroz and Van der Baan (2013). Location uncertainties may also result from velocity model error. The back-propagated wavefield may focus to a misplaced location under an incorrect velocity model. In particular systematic biases from the true model may be problematic. However, use of a much more strongly smoothed velocity model than shown in Figure 3.10b still leads to acceptable locations. In case of erroneous velocities, the proposed Hough Transform based focusing criterion can still find the most focused points, but possibly at an incorrect location. Location uncertainties can be decreased with a more accurate velocity model and/or larger acquisition apertures. To increase the acquisition aperture, a combination of borehole and surface receivers may work best. Indeed even though our example include purely borehole acquisitions, the methodology is readily applicable to surface recordings.

In the representation theorem, a normal vector to the boundary of the enclosed volume is needed in the calculation. That means the normal vector $\boldsymbol{n}_r$ should be specified prior to combination of the various wavefields. This leads to various possible choices especially if the receivers are located in a single borehole. For traditional surface land acquisition system, the normal vector is generally set as pointing upward, but for a straight well trajectory the azimuth of the normal vector is not easily determined. So we suggest to approximate the normal vector according to the spatial relationship between observation well and treatment well. The property of ghost focusing cancellation can also help

determine the azimuth of microseismic events by finding the optimal focusing for different normal vectors. This is mainly because at the correct azimuth, the back-propagated pressure and particle velocity field should optimally align at one side of the borehole and fully cancel at the opposite side.

The performance of the modified Hough transform depends significantly on the ratio between acquisition aperture and source-receiver distance. The ratio has to be sufficiently large for successful focusing. A small ratio makes the back-propagated receiver-side wavefield diverge rather than converge where the assumption of circular wavefronts breaks down. Moreover, the distance from treatment well to observation well determines the $\mathbb{T}_D$ threshold. The microseismic events must exist beyond reasonable range around the treatment well. High focusings inside of this range are not considered. The selection of the $\mathbb{T}_M$ threshold comprises a trade-off between risk of detecting false events and missing true events. A high threshold lowers the risk of identifying false events but also increases the chance of missing true events. On the contrary, a low threshold increases the number of detected events but also the number of false alarms.

Finally, the computational time of the focusing criterion varies with respect to discrete time interval Δt_N. The computational time of the back-propagation process T_{bp} is proportional to $N_T N_X^d$, where N_T is the number of time steps, N_X is the number of gridpoints in dimension d (Van Manen et al., 2006). For simplicity we omit the number of flops needed for calculation of the discrete derivatives. The computational time for the focusing criterion T_{fc} is proportional to $N_T/\Delta t_N N_X^d$ because we only calculate a Hough image for every Δt_N time points. The additional computational time of the focusing criterion is different with different Δt_N but generally it is smaller than 10% of the back-propagation time.

3.5   Conclusion

Representation-theorem-based time-reversal extrapolation offers much promise for obtaining microseismic event locations without the need to first pick individual arrivals, in particular if both the pressure wavefield and its spatial

gradients are available. The latter may require the combined usage of both hydrophones and three-component particle-velocity sensors during microseismic acquisition to get improved microseismic event locations. The Hough map provides a convenient and stable criterion for automatically detecting both event locations and origin times.

Chapter 4

Elastic passive source localization using rotational motion [1]

As a complement to traditional particle velocity recordings, rotational motion provides information on the spatial gradient of particle displacement motion which aids in imaging passive sources using elastic waves. Event localization is for instance important in earthquake seismology and detection of microseismic events during hydraulic fracturing treatments of hydrocarbon reservoirs or injection of carbon dioxide (CO_2) in depleted reservoirs. We propose an elastic reverse time extrapolation technique for passive event localization incorporating a new representation-theorem-based expression that explicitly uses recordings from rotational and particle velocity sensors either simultaneously or separately, leading to enhanced imaging results. We also introduce a novel focusing criterion based on the energy flux which is insensitive to polarity reversals due to non-isotropic source mechanisms. Energy flux combined with the Hough transform leads to a convenient and stable criterion for automatically detecting both event locations and origin times.

---

[1]A version of this chapter has been accepted as Li, Z. and van der Baan, M., 2017, Elastic passive source localization using rotational motion, Geophysical Journal International.

4.1 Introduction

Object or event localization is a widely applied technique in both civilian and national defense usage. Receivers detect acoustic or elastic waves radiated from a source followed by an analysis technique to remotely determine the distance and location of the source. Different types of waves are used for various purposes. For example, acoustic sound in water detected by sonar is used to locate submarines for military usage (Ainslie, 2010). Medical ultrasound is nowadays a common imaging technique to observe internal human body structure for health examinations (McKeighen, 1998). Seismologists detect and analyze elastic waves radiated from a natural earthquake to accurately locate the event and better understand the subsurface tectonics and geology (McMechan, 1985). We focus on another application, namely microseismic event localization (Artman et al., 2010). Microseismicity commonly refers to elastic waves created by rock failure induced by human activities, such as mining and hydraulic fracturing, whose magnitudes are generally smaller than zero on the Gutenberg-Richter scale (Van der Baan et al., 2013). Nonetheless, the described imaging techniques are general and can be applied to both recorded acoustic and elastic waves.

Microseismic event localization and characterization are important tools for understanding in situ rock deformation due to human activities. Microseismic event localization methods generally are categorized into travel-time based and migration based types. Picking of longitudal P- and shear S-wave arrivals is required for the travel-time based method before further processing. However, event picking can often be a challenging and time-consuming task for low quality data (Artman et al., 2010). Both mispicks and missing picks negatively influence event locations (Kocon and Van der Baan, 2012; Castellanos and Van der Baan, 2013; Castellanos and Van der Baan, 2015).

Migration based methods are more suitable for low SNR data (Artman et al., 2010) by avoiding P- and S-wave picking. Time reversal extrapolation is one of the most important methods in this category, which has been applied in locating earthquakes (McMechan, 1985) and microseismic events (Artman et al., 2010). Following a similar procedure as reverse time migration (McMechan, 1983), the time-reversed transmission wavefield is extrapolated

(Artman et al., 2010), followed by an auto-correlation imaging condition to identify the event location and origin time.

Ravasi and Curtis (2013) built an exact wavefield extrapolation algorithm based on the elastic representation theorem. The method requires the measurements of both particle velocity and its spatial gradient in the extrapolation. The combination of the wavefield and its spatial gradient allows for removing those non-physical artifacts due to explicit inclusion of directivity (Wapenaar and Fokkema, 2006). Also this method avoids the creation of false wave modes due to the conventional adjoint state elastic extrapolation. Because the measurement of the spatial gradient of particle velocity/displacement is not always directly available, a high frequency approximation is often needed to avoid using the spatial gradient term (Wapenaar and Fokkema, 2006). This approximation may introduce artifacts to the extrapolated images. An alternative modification is to combine particle velocity and elastodynamic traction in the extrapolation (Wapenaar and Fokkema, 2006,Ravasi and Curtis, 2013). This modified version is especially suitable for processing dual-sensor-streamer data in marine acquisition where particle velocity and pressure are measured simultaneously in an acoustic medium (Ravasi and Curtis, 2013). In land acquisition, two scenarios are considered separately, namely with receivers on the free surface, or shallowly buried or deeper placed geophones such as in boreholes. In the first scenario, only particle velocity is retained in the elastic representation theorem since both normal and shear stresses on the free surface are assumed to be negligible, whereas the latter scenario requires both measurements, because stress does not vanish. Since spatial wavefield gradients in all three directions are rarely measured with sufficient accuracy, we propose using rotational rate recordings as a replacement of the spatial gradient of particle velocity/displacement in this paper. The developed methodology is applicable to both surface and borehole recordings but may be most pertinent to borehole acquisitions because in this case spatial gradients cannot be ignored in representation-based wavefield extrapolation.

In classical infinitesimal elasticity, to completely describe particle motion, we need translational motion, strain deformation and rigid rotation (Van Driel et al., 2012, Li and Van der Baan, 2017). The spatial gradient of particle veloc-

ity is composed of strain deformation and rigid rotation, representing particle deformation. Traditional three-component inertial geophones and seismometers can only measure translational motion and strain deformation along three orthogonal directions, which is not sensitive to rotational motion. Recently, the development of new instruments provides an opportunity to directly record and study the rigid rotational rate in vertical and horizontal directions (Lee et al., 2012). Because rotational rate measurements also include information on the spatial gradient of particle velocity, it will aid in representation theorem based reverse time extrapolation.

In this paper, we first introduce the basic concept of rotational motion. Then we derive the representation theorem from the second-order elastic wave equations in a homogeneous medium which can be applied to simultaneously extrapolate both rotational and particle velocity recordings. Next we describe the implementation scheme especially for passive event localization. Then a new energy flux based focusing criterion is introduced, based on the Hough transform (Li and Van der Baan, 2016). Finally, we use two examples to show that the proposed method also works well in an inhomogeneous medium.

4.2 Theory

4.2.1 Isotropic elastic Representation theorem

In this section we derive the elastic representation theorem for wavefield back-propagation based on a similar procedure as in Knopoff (1956). The homogeneous isotropic second-order elastic wave equation for particle velocity vector $\boldsymbol{v}(\boldsymbol{r}, t)$ in the time domain is used, given by

$$\rho \frac{\partial^2 \boldsymbol{v}(\boldsymbol{r}, t)}{\partial t^2} = (\lambda + 2\mu)\, \boldsymbol{\nabla}\boldsymbol{\nabla} \cdot \boldsymbol{v}(\boldsymbol{r}, t) - \mu \boldsymbol{\nabla} \times \boldsymbol{\nabla} \times \boldsymbol{v}(\boldsymbol{r}, t) + \dot{\boldsymbol{f}}(t)\delta(\boldsymbol{r} - \boldsymbol{r}^s), \ (4.1)$$

where $\boldsymbol{r}$ represents spatial location; ρ is the medium density; λ and μ are the Lamé parameters; $\dot{\boldsymbol{f}}$ is the temporal waveform of the body force rate; $\delta(\boldsymbol{r} - \boldsymbol{r}^s)$ is a kronecker delta with a non-zero value only at $\boldsymbol{r}^s$ indicating the source

location. We further simplify equation 4.1 by dividing both sides by density ρ, giving

$$\frac{\partial^2 \boldsymbol{v}(\boldsymbol{r},t)}{\partial t^2} = \alpha^2 \boldsymbol{\nabla}\boldsymbol{\nabla} \cdot \boldsymbol{v}(\boldsymbol{r},t) - \beta^2 \boldsymbol{\nabla} \times \boldsymbol{\nabla} \times \boldsymbol{v}(\boldsymbol{r},t) + \dot{\boldsymbol{F}}(t)\delta(\boldsymbol{r}-\boldsymbol{r}^s), \quad (4.2)$$

where α and β are P- and S-wave velocity; $\dot{\boldsymbol{F}}(t)$ is the applied body acceleration rate represented by $\dot{\boldsymbol{f}}(t)/\rho$.

Two independent states A and B are defined fulfilling equation 4.2 in the same spatiotemporal 3D domain $\mathbb{D} \subset \mathbb{R}$, with boundary $\partial\mathbb{D} \subset \mathbb{R}$. States here simply mean a combination of material parameters, field quantities, source distributions, boundary conditions and initial conditions that satisfy the relevant wave equation (Van Manen et al., 2006,Li and Van der Baan, 2016). Here we assume that all other parameters in both states are the same except for the sources and the wavefields. For simplicity, we write the elastic wave equation for state A and B in the frequency domain, given by

$$-\omega^2 \hat{\boldsymbol{v}}^{A/B}(\boldsymbol{r},\omega) = \alpha^2 \boldsymbol{\nabla}\boldsymbol{\nabla} \cdot \hat{\boldsymbol{v}}^{A/B}(\boldsymbol{r},\omega) - \beta^2 \boldsymbol{\nabla} \times \boldsymbol{\nabla} \times \hat{\boldsymbol{v}}^{A/B}(\boldsymbol{r},\omega) + \hat{\dot{\boldsymbol{F}}}^{A/B}(\omega)\delta(\boldsymbol{r}-\boldsymbol{r}^{A/B}),$$

$$(4.3)$$

where $\hat{}$ represents variables in the frequency domain; ω angular frequency; A/B state A or B.

According to the definition of particle rotational motion in the previous section, we replace the curl of the particle velocity $\boldsymbol{\nabla} \times \hat{\boldsymbol{v}}^{A/B}$ in equation 4.3 with the particle rotational rate $2\dot{\hat{\boldsymbol{\Omega}}}^{A/B}$ (equation 2.3), giving

$$-\omega^2 \hat{\boldsymbol{v}}^{A/B}(\boldsymbol{r},\omega) = \alpha^2 \boldsymbol{\nabla}\boldsymbol{\nabla} \cdot \hat{\boldsymbol{v}}^{A/B}(\boldsymbol{r},\omega) - 2\beta^2 \boldsymbol{\nabla} \times \dot{\hat{\boldsymbol{\Omega}}}^{A/B}(\boldsymbol{r},\omega) + \hat{\dot{\boldsymbol{F}}}^{A/B}(\omega)\delta(\boldsymbol{r}-\boldsymbol{r}^{A/B}).$$

$$(4.4)$$

We arbitrarily choose state A as the wavefield from real recordings, such as an actual event. State B is the Green's state of a point impulse source of the body acceleration rate of unit strength and exerted in the direction of Cartesian coordinate $\boldsymbol{x}_n$ with $n = 1, 2$ or 3. We denote this unit point source as $\hat{\boldsymbol{x}}_n\delta(\boldsymbol{r}-\boldsymbol{r}^B)$, where $\hat{\boldsymbol{x}}_n$ is the unit vector pointing in the direction of

Cartesian coordinate x_n. $\hat{\boldsymbol{v}}^B$ then becomes the Green's function $\hat{\boldsymbol{G}}_{\boldsymbol{v},n}(\boldsymbol{r}, \boldsymbol{r}^B, \omega)$ (Wapenaar and Fokkema, 2006), and the corresponding Green's function for $\hat{\dot{\boldsymbol{\Omega}}}^B$ is expressed by $\hat{\boldsymbol{G}}_{\dot{\boldsymbol{\Omega}},n}(\boldsymbol{r}, \boldsymbol{r}^B, \omega)$. With the above assumptions, the vector form of equations 4.4 for state A and B become

$$-\omega^2 \hat{\boldsymbol{v}}(\boldsymbol{r}, \boldsymbol{r}^A, \omega) = \alpha^2 \boldsymbol{\nabla}\boldsymbol{\nabla} \cdot \hat{\boldsymbol{v}}(\boldsymbol{r}, \boldsymbol{r}^A, \omega) - 2\beta^2 \boldsymbol{\nabla} \times \hat{\dot{\boldsymbol{\Omega}}}(\boldsymbol{r}, \boldsymbol{r}^A, \omega) + \hat{\dot{\boldsymbol{F}}}(\omega)\delta(\boldsymbol{r} - \boldsymbol{r}^A),$$
(4.5)

and

$$-\omega^2 \hat{\boldsymbol{G}}_{\boldsymbol{v},n}(\boldsymbol{r}, \boldsymbol{r}^B, \omega) = \alpha^2 \boldsymbol{\nabla}\boldsymbol{\nabla} \cdot \hat{\boldsymbol{G}}_{\boldsymbol{v},n}(\boldsymbol{r}, \boldsymbol{r}^B, \omega) - 2\beta^2 \boldsymbol{\nabla} \times \hat{\boldsymbol{G}}_{\dot{\boldsymbol{\Omega}},n}(\boldsymbol{r}, \boldsymbol{r}^B, \omega) + \hat{\boldsymbol{x}}_n \delta(\boldsymbol{r} - \boldsymbol{r}^B).$$
(4.6)

Next, a time-reversed wavefield can be derived by taking the complex conjugate of equation 4.6 (Wapenaar and Fokkema, 2006), given by

$$-\omega^2 \hat{\boldsymbol{G}}_{\boldsymbol{v},n}^{*}(\boldsymbol{r}, \boldsymbol{r}^B, \omega) = \alpha^2 \boldsymbol{\nabla}\boldsymbol{\nabla} \cdot \hat{\boldsymbol{G}}_{\boldsymbol{v},n}^{*}(\boldsymbol{r}, \boldsymbol{r}^B, \omega) - 2\beta^2 \boldsymbol{\nabla} \times \hat{\boldsymbol{G}}_{\dot{\boldsymbol{\Omega}},n}^{*}(\boldsymbol{r}, \boldsymbol{r}^B, \omega) + \hat{\boldsymbol{x}}_n \delta(\boldsymbol{r} - \boldsymbol{r}^B).$$
(4.7)

where $*$ represents the complex conjugate. We then multiply equations 4.7 and 4.5 with $\hat{\boldsymbol{v}}(\boldsymbol{r}, \boldsymbol{r}^A, \omega)$ and $\hat{\boldsymbol{G}}_{\boldsymbol{v},n}^{*}(\boldsymbol{r}, \boldsymbol{r}^B, \omega)$ respectively to construct the correlation type of the elastic representation theorem (Wapenaar and Fokkema, 2006, Li and Van der Baan, 2016). Subsequent subtraction of the resulting equations produces

$$0 = \hat{\boldsymbol{v}}(\boldsymbol{r}, \boldsymbol{r}^A, \omega) \cdot \alpha^2 \left(\boldsymbol{\nabla}\boldsymbol{\nabla} \cdot \hat{\boldsymbol{G}}_{\boldsymbol{v},n}^{*}(\boldsymbol{r}, \boldsymbol{r}^B, \omega) \right) - \hat{\boldsymbol{G}}_{\boldsymbol{v},n}^{*}(\boldsymbol{r}, \boldsymbol{r}^B, \omega) \cdot \alpha^2 \left(\boldsymbol{\nabla}\boldsymbol{\nabla} \cdot \hat{\boldsymbol{v}}(\boldsymbol{r}, \boldsymbol{r}^A, \omega) \right)$$

$$+ \hat{\boldsymbol{G}}_{\boldsymbol{v},n}^{*}(\boldsymbol{r}, \boldsymbol{r}^B, \omega) \cdot 2\beta^2 \boldsymbol{\nabla} \times \hat{\dot{\boldsymbol{\Omega}}}(\boldsymbol{r}, \boldsymbol{r}^A, \omega) - \hat{\boldsymbol{v}}(\boldsymbol{r}, \boldsymbol{r}^A, \omega) \cdot 2\beta^2 \boldsymbol{\nabla} \times \hat{\boldsymbol{G}}_{\dot{\boldsymbol{\Omega}},n}^{*}(\boldsymbol{r}, \boldsymbol{r}^B, \omega)$$

$$+ \hat{\boldsymbol{v}}(\boldsymbol{r}, \boldsymbol{r}^A, \omega) \cdot \hat{\boldsymbol{x}}_n \delta(\boldsymbol{r} - \boldsymbol{r}^B) - \hat{\boldsymbol{G}}_{\boldsymbol{v},n}^{*}(\boldsymbol{r}, \boldsymbol{r}^B, \omega) \cdot \hat{\dot{\boldsymbol{F}}}(\omega)\delta(\boldsymbol{r} - \boldsymbol{r}^A).$$
(4.8)

We move the 5th and 6th term on the right-hand side of equation 4.8 to the left-hand-side and apply a volume integral within $\mathbb{D}$ to both sides, yielding

$$\int_{\mathbb{D}} \hat{\boldsymbol{G}}^{*}_{\boldsymbol{v},n}(\boldsymbol{r}, \boldsymbol{r}^{B}, \omega) \cdot \hat{\boldsymbol{F}}(\omega)\delta(\boldsymbol{r} - \boldsymbol{r}^{A})dV - \int_{\mathbb{D}} \hat{\boldsymbol{v}}(\boldsymbol{r}, \boldsymbol{r}^{A}, \omega) \cdot \hat{\boldsymbol{x}}_{n}\delta(\boldsymbol{r} - \boldsymbol{r}^{B})dV =$$

$$\int_{\mathbb{D}} \left[\hat{\boldsymbol{v}}(\boldsymbol{r}, \boldsymbol{r}^{A}, \omega) \cdot \alpha^{2} \left(\boldsymbol{\nabla}\boldsymbol{\nabla} \cdot \hat{\boldsymbol{G}}^{*}_{\boldsymbol{v},n}(\boldsymbol{r}, \boldsymbol{r}^{B}, \omega) \right) - \hat{\boldsymbol{G}}^{*}_{\boldsymbol{v},n}(\boldsymbol{r}, \boldsymbol{r}^{B}, \omega) \cdot \alpha^{2} \left(\boldsymbol{\nabla}\boldsymbol{\nabla} \cdot \hat{\boldsymbol{v}}(\boldsymbol{r}, \boldsymbol{r}^{A}, \omega) \right) \right] dV$$

$$+ \int_{\mathbb{D}} \left[\hat{\boldsymbol{G}}^{*}_{\boldsymbol{v},n}(\boldsymbol{r}, \boldsymbol{r}^{B}, \omega) \cdot 2\beta^{2}\boldsymbol{\nabla} \times \hat{\boldsymbol{\Omega}}(\boldsymbol{r}, \boldsymbol{r}^{A}, \omega) - \hat{\boldsymbol{v}}(\boldsymbol{r}, \boldsymbol{r}^{A}, \omega) \cdot 2\beta^{2}\boldsymbol{\nabla} \times \hat{\boldsymbol{G}}^{*}_{\dot{\boldsymbol{\Omega}},n}(\boldsymbol{r}, \boldsymbol{r}^{B}, \omega) \right] dV.$$

$$(4.9)$$

The first term on the left-hand side is simplified as follows,

$$\int_{\mathbb{D}} \hat{\boldsymbol{G}}^{*}_{\boldsymbol{v},n}(\boldsymbol{r}, \boldsymbol{r}^{B}, \omega) \cdot \hat{\boldsymbol{F}}(\omega)\delta(\boldsymbol{r} - \boldsymbol{r}^{A})dV = \int_{\mathbb{D}} \hat{\boldsymbol{G}}^{*}_{\boldsymbol{v},n}(\boldsymbol{r}^{A}, \boldsymbol{r}^{B}, \omega) \cdot \hat{\boldsymbol{F}}(\omega)dV$$

$$= \int_{\mathbb{D}} \hat{G}^{*}_{1,n}(\boldsymbol{r}^{A}, \boldsymbol{r}^{B}, \omega)\hat{F}_{1}(\omega)dV + \int_{\mathbb{D}} \hat{G}^{*}_{2,n}(\boldsymbol{r}^{A}, \boldsymbol{r}^{B}, \omega)\hat{F}_{2}(\omega)dV + \int_{\mathbb{D}} \hat{G}^{*}_{3,n}(\boldsymbol{r}^{A}, \boldsymbol{r}^{B}, \omega)\hat{F}_{3}(\omega)dV$$

$$= \int_{\mathbb{D}} \hat{G}^{*}_{n,1}(\boldsymbol{r}^{B}, \boldsymbol{r}^{A}, \omega)\hat{F}_{1}(\omega)dV + \int_{\mathbb{D}} \hat{G}^{*}_{n,2}(\boldsymbol{r}^{B}, \boldsymbol{r}^{A}, \omega)\hat{F}_{2}(\omega)dV + \int_{\mathbb{D}} \hat{G}^{*}_{n,3}(\boldsymbol{r}^{B}, \boldsymbol{r}^{A}, \omega)\hat{F}_{3}(\omega)dV$$

$$= \hat{v}^{*}_{n}(\boldsymbol{r}^{B}, \boldsymbol{r}^{A}, \omega),$$

$$(4.10)$$

where $\hat{G}^{*}_{i,n}(\boldsymbol{r}^{A}, \boldsymbol{r}^{B}, \omega)$ ($i = 1$, 2 or 3) is the ith component of the time-reversed Green's function $\hat{\boldsymbol{G}}^{*}_{\boldsymbol{v},n}(\boldsymbol{r}^{A}, \boldsymbol{r}^{B}, \omega)$, which satisfies the reciprocity theorem (Knopoff and Gangi, 1959) that $\hat{G}^{*}_{i,n}(\boldsymbol{r}^{A}, \boldsymbol{r}^{B}, \omega) = \hat{G}^{*}_{n,i}(\boldsymbol{r}^{B}, \boldsymbol{r}^{A}, \omega)$.

The second term on the left-hand side of equation 4.9 is a forward extrapolation term which can be simplified to $\hat{v}_{n}(\boldsymbol{r}^{B}, \boldsymbol{r}^{A}, \omega)$ according to the definition of the delta function. In reality, this term can not be calculated because it requires the knowledge of the source locations, which are unknown as they are the objective of any localization method. Without this term, the back-propagated wavefields diverge again after they converge at their source locations. To compensate for the missing calculation of the forward propagation term, we introduce a focusing criterion for automatic event localization in a later section.

The first and second volume integration terms on the right-hand side of equation 4.9 are replaced by the surface integrations within $\partial\mathbb{D}$ according to the Green's theorem (equations 4 and 5 in Knopoff (1956)), giving

$$\hat{v}_n^*(\boldsymbol{r}^B, \boldsymbol{r}^A, \omega) - \hat{v}_n(\boldsymbol{r}^B, \boldsymbol{r}^A, \omega) =$$

$$\int_{\partial \mathbb{D}} \mathbf{n} \cdot \alpha^2 \left[\hat{\boldsymbol{v}}(\boldsymbol{r}, \boldsymbol{r}^A, \omega) \left(\boldsymbol{\nabla} \cdot \hat{\boldsymbol{G}}_{v,n}^*(\boldsymbol{r}, \boldsymbol{r}^B, \omega) \right) - \hat{\boldsymbol{G}}_{v,n}^*(\boldsymbol{r}, \boldsymbol{r}^B, \omega) \left(\boldsymbol{\nabla} \cdot \hat{\boldsymbol{v}}(\boldsymbol{r}, \boldsymbol{r}^A, \omega) \right) \right] dS$$

$$+ \int_{\partial \mathbb{D}} \mathbf{n} \cdot 2\beta^2 \left[\hat{\dot{\boldsymbol{\Omega}}}(\boldsymbol{r}, \boldsymbol{r}^A, \omega) \times \hat{\boldsymbol{G}}_{v,n}^*(\boldsymbol{r}, \boldsymbol{r}^B, \omega) - \hat{\boldsymbol{G}}_{\dot{\boldsymbol{\Omega}},n}^*(\boldsymbol{r}, \boldsymbol{r}^B, \omega) \times \hat{\boldsymbol{v}}(\boldsymbol{r}, \boldsymbol{r}^A, \omega) \right] dS,$$

$$(4.11)$$

where $\mathbf{n}$ is the outward pointing normal of the integration boundary (Li and Van der Baan, 2016). Equation 4.11 indicates we can calculate the back-propagated particle velocity field inside of volume $\mathbb{D}$ when we have the measurements of rotational motions and the particle velocity fields on the boundary $\partial \mathbb{D}$. All bold symbols are vectors depending on the x, y and z components in the 3-D case. This equation allows us to locate the source at location $\boldsymbol{r}^A$ if we have the measurements of the rotational rate wavefield $\dot{\boldsymbol{\Omega}}$ and the particle velocity fields $\boldsymbol{v}$ on the boundary ∂D.

We write equation 4.11 into a form with a much clearer physical meaning, given by

$$\hat{v}_n^*(\boldsymbol{r}^B, \boldsymbol{r}^A, \omega) - \hat{v}_n(\boldsymbol{r}^B, \boldsymbol{r}^A, \omega) =$$

$$\int_{\partial \mathbb{D}} \mathbf{n} \cdot \alpha^2 \left[\hat{\boldsymbol{v}}^p(\boldsymbol{r}, \boldsymbol{r}^A, \omega) \left(\boldsymbol{\nabla} \cdot \hat{\boldsymbol{G}}_{v^p,n}^*(\boldsymbol{r}, \boldsymbol{r}^B, \omega) \right) - \hat{\boldsymbol{G}}_{v^p,n}^*(\boldsymbol{r}, \boldsymbol{r}^B, \omega) \left(\boldsymbol{\nabla} \cdot \hat{\boldsymbol{v}}^p(\boldsymbol{r}, \boldsymbol{r}^A, \omega) \right) \right] dS$$

$$+ \int_{\partial \mathbb{D}} \mathbf{n} \cdot 2\beta^2 \left[\hat{\dot{\boldsymbol{\Omega}}}(\boldsymbol{r}, \boldsymbol{r}^A, \omega) \times \hat{\boldsymbol{G}}_{v^s,n}^*(\boldsymbol{r}, \boldsymbol{r}^B, \omega) - \hat{\boldsymbol{G}}_{\dot{\boldsymbol{\Omega}},n}^*(\boldsymbol{r}, \boldsymbol{r}^B, \omega) \times \hat{\boldsymbol{v}}^s(\boldsymbol{r}, \boldsymbol{r}^A, \omega) \right] dS,$$

$$(4.12)$$

where the first line on the right-hand side of equation 4.11 is the back-propagated P-wavefield whereas the second line is the back-propagated S-wavefield, as indicated by the symbols p and s in the Green's functions and particle velocities. A detailed derivation is shown in appendix A. The first and second terms on the right-hand side of equation 4.12 mean the P- and S-wavefields can be reconstructed separately, using

$$\hat{v}_n^{p*}(\boldsymbol{r}^B, \boldsymbol{r}^A, \omega) + \hat{v}_n^p(\boldsymbol{r}^B, \boldsymbol{r}^A, \omega) =$$

$$\int_{\partial \mathbb{D}} \mathbf{n} \cdot \alpha^2 \left[\hat{\boldsymbol{v}}^p(\boldsymbol{r}, \boldsymbol{r}^A, \omega) \left(\boldsymbol{\nabla} \cdot \hat{\boldsymbol{G}}_{\boldsymbol{v}^p, n}^*(\boldsymbol{r}, \boldsymbol{r}^B, \omega) \right) - \hat{\boldsymbol{G}}_{\boldsymbol{v}^p, n}^*(\boldsymbol{r}, \boldsymbol{r}^B, \omega) \left(\boldsymbol{\nabla} \cdot \hat{\boldsymbol{v}}^p(\boldsymbol{r}, \boldsymbol{r}^A, \omega) \right) \right] dS,$$

(4.13)

and

$$\hat{v}_n^{s*}(\boldsymbol{r}^B, \boldsymbol{r}^A, \omega) + \hat{v}_n^s(\boldsymbol{r}^B, \boldsymbol{r}^A, \omega) =$$

$$\int_{\partial \mathbb{D}} \mathbf{n} \cdot 2\beta^2 \left[\hat{\boldsymbol{\Omega}}(\boldsymbol{r}, \boldsymbol{r}^A, \omega) \times \hat{\boldsymbol{G}}_{\boldsymbol{v}^s, n}^*(\boldsymbol{r}, \boldsymbol{r}^B, \omega) - \hat{\boldsymbol{G}}_{\dot{\boldsymbol{\Omega}}, n}^*(\boldsymbol{r}, \boldsymbol{r}^B, \omega) \times \hat{\boldsymbol{v}}^s(\boldsymbol{r}, \boldsymbol{r}^A, \omega) \right] dS,$$

(4.14)

essentially because P- and S-wave fields are decoupled in homogeneous isotropic media. Note that equations 4.13 and 4.14 indicate that P/S-wavefield separation is required at the receiver level. Various P/S wavefield separation techniques exist (Schalkwijk et al., 1999, Schalkwijk et al., 2003, Al-Anboori and Kendall, 2005, Van der Baan et al., 2013).

4.2.2   Implementation

In this section, we introduce more details on the practical implementation of our proposed methods for passive event localization. The S-wave energy of a microseismic event or earthquake is often several times stronger than their P-wave energy, even in case of non-double-couple moment tensors (Eaton et al., 2014). For simplicity, one could therefore use expression 4.14 involving solely the S-wave particle velocity. We thus assume that P/S wavefield separation may not be required. Unfortunately, equation 4.14 also invokes $\boldsymbol{G}_{v_s}$ the S-wave only Green's function. Computation of an S-wave only Green's function for elastic media is likely to be cumbersome. If we replace the S-wave only Green's function $\boldsymbol{G}_{\boldsymbol{v}^s}$ with the full Green's function $\boldsymbol{G}_{\boldsymbol{v}}$ then we obtain

$$\hat{v}_n^{s*}(\boldsymbol{r}^B, \boldsymbol{r}^A, \omega) + \hat{v}_n^s(\boldsymbol{r}^B, \boldsymbol{r}^A, \omega) \approx$$
$$\int_{\partial \mathbb{D}} \mathbf{n} \cdot 2\beta^2 \left[\hat{\dot{\boldsymbol{\Omega}}}(\boldsymbol{r}, \boldsymbol{r}^A, \omega) \times \hat{\boldsymbol{G}}_{\boldsymbol{v},n}^*(\boldsymbol{r}, \boldsymbol{r}^B, \omega) - \hat{\boldsymbol{G}}_{\dot{\boldsymbol{\Omega}},n}^*(\boldsymbol{r}, \boldsymbol{r}^B, \omega) \times \hat{\boldsymbol{v}}(\boldsymbol{r}, \boldsymbol{r}^A, \omega) \right] dS,$$

(4.15)

where the full recordings of particle velocities $\hat{\boldsymbol{v}}(\boldsymbol{r}, \boldsymbol{r}^A, \omega)$ is used to replace S-wave recordings $\hat{\boldsymbol{v}}^s(\boldsymbol{r}, \boldsymbol{r}^A, \omega)$ in equation 4.14. Rotational rate recordings $\hat{\dot{\boldsymbol{\Omega}}}(\boldsymbol{r}, \boldsymbol{r}^A, \omega)$ can be obtained from rotational sensors.

Implementation of equation 4.15 by expanding its right-hand side into a scalar form for the 3-D case, producing

$$\hat{v}_n^{s*}(\boldsymbol{r}^B, \boldsymbol{r}^A, \omega) + \hat{v}_n^s(\boldsymbol{r}^B, \boldsymbol{r}^A, \omega) \approx$$
$$\oint_{\partial \mathbb{D}} 2\beta^2 \left[\mathrm{n}_x (\hat{G}_{\dot{\Omega}_y,n}^*(\boldsymbol{r}, \boldsymbol{r}^B, \omega) \hat{v}_z(\boldsymbol{r}, \boldsymbol{r}^A, \omega) - \hat{G}_{\dot{\Omega}_z,n}^*(\boldsymbol{r}, \boldsymbol{r}^B, \omega) \hat{v}_y(\boldsymbol{r}, \boldsymbol{r}^A, \omega)) \right.$$
$$+ \mathrm{n}_y (\hat{G}_{\dot{\Omega}_z,n}^*(\boldsymbol{r}, \boldsymbol{r}^B, \omega) \hat{v}_x(\boldsymbol{r}, \boldsymbol{r}^A, \omega) - \hat{G}_{\dot{\Omega}_x,n}^*(\boldsymbol{r}, \boldsymbol{r}^B, \omega) \hat{v}_z(\boldsymbol{r}, \boldsymbol{r}^A, \omega))$$
$$+ \mathrm{n}_z (\hat{G}_{\dot{\Omega}_x,n}^*(\boldsymbol{r}, \boldsymbol{r}^B, \omega) \hat{v}_y(\boldsymbol{r}, \boldsymbol{r}^A, \omega) - \hat{G}_{\dot{\Omega}_y,n}^*(\boldsymbol{r}, \boldsymbol{r}^B, \omega) \hat{v}_x(\boldsymbol{r}, \boldsymbol{r}^A, \omega)) \qquad (4.16)$$
$$- \mathrm{n}_x (\hat{\dot{\Omega}}_y(\boldsymbol{r}, \boldsymbol{r}^A, \omega) \hat{G}_{v_z,n}^*(\boldsymbol{r}, \boldsymbol{r}^B, \omega) - \hat{\dot{\Omega}}_z(\boldsymbol{r}, \boldsymbol{r}^A, \omega) \hat{G}_{v_y,n}^*(\boldsymbol{r}, \boldsymbol{r}^B, \omega))$$
$$- \mathrm{n}_y (\hat{\dot{\Omega}}_z(\boldsymbol{r}, \boldsymbol{r}^A, \omega) \hat{G}_{v_x,n}^*(\boldsymbol{r}, \boldsymbol{r}^B, \omega) - \hat{\dot{\Omega}}_x(\boldsymbol{r}, \boldsymbol{r}^A, \omega) \hat{G}_{v_z,n}^*(\boldsymbol{r}, \boldsymbol{r}^B, \omega))$$
$$\left. - \mathrm{n}_z (\hat{\dot{\Omega}}_x(\boldsymbol{r}, \boldsymbol{r}^A, \omega) \hat{G}_{v_y,n}^*(\boldsymbol{r}, \boldsymbol{r}^B, \omega) - \hat{\dot{\Omega}}_y(\boldsymbol{r}, \boldsymbol{r}^A, \omega) \hat{G}_{v_x,n}^*(\boldsymbol{r}, \boldsymbol{r}^B, \omega)) \right] dS,$$

where x, y and z are the Cartesian coordinates. In the right-hand side of equation 4.16 there are 12 multiplications in the frequency domain within the square bracket, which represent cross-correlations in the time domain. Considering for instance the term $n_x \hat{\dot{\Omega}}_y(\boldsymbol{r}, \boldsymbol{r}^A, \omega) \hat{G}_{v_z,n}^*(\boldsymbol{r}, \boldsymbol{r}^B, \omega)$, it represents the y component of rotation rate $\dot{\boldsymbol{\Omega}}$ recorded at $\boldsymbol{r}$ from an event at $\boldsymbol{r}^A$; it is cross-correlated with the z component of the time-reversed Green's function of the particle velocity $G_{v_z,n}^*$ recorded at $\boldsymbol{r}$ from an impulse source at $\boldsymbol{r}^B$ in the nth direction. Likewise, the term $n_x \hat{G}_{\dot{\Omega}_y,n}^*(\boldsymbol{r}, \boldsymbol{r}^B, \omega) \hat{v}_z(\boldsymbol{r}, \boldsymbol{r}^A, \omega)$ represents the z component of the back-propagated particle velocity v_z from the event at $\boldsymbol{r}^A$ as cross-correlated

with the y component of the time-reversed Green's function of the rotational rate $G^*_{\Omega_y,n}$ from the same impulse source at $\boldsymbol{r}^B$. The sum of the contribution of both terms is controlled by the x component of the normal vector $\mathbf{n}$. Other terms at the right-hand side of equation 4.16 have similar meaning but involve different combinations of particle velocity and rotation rate components. The orientation of normal vector $\mathbf{n}$ depends on the pre-defined integration boundary $\partial \mathbb{D}$ (Li and Van der Baan, 2016).

In practice, a forward modeling scheme such as a finite difference algorithm (Pitarka, 1999) is used instead of cross-correlation. Similar to implementation for standard acoustic or elastic reverse time migration, the recorded three components of particle velocities are time-reversed and then forward propagated into the medium (McMechan, 1983). Likewise, the recorded three components of the rotational rate are back-propagated.

The final image is then obtained by stacking all back-propagated images for all receivers. This allows us to backpropagate only the three-component particle velocity or three-component rotational rate individually as well as also stack their combined images. A focusing criterion, described next is applied to the wavefield at each time slice to determine the origin time and hypocenter of the microseismic event or other passive source.

4.2.3 Energy based focusing criterion

In this section we propose a focusing criterion based on the evaluation of the energy flux in the back-propagated image. The entire procedure is based on the Hough transform as proposed by Li and Van der Baan (2016) but applied to energy flux instead of summation of amplitudes. In essence, we assume that the wavefront approximately converges towards the source location as a spherical wavefront in 3-D implementations or a circle in 2-D ones. In the illustrated 2-D case, we consider a circle centered at the source location, and measure the total energy E going into and out of the circle during a time period Δt (Figure 4.1). The radius of the circle R is determined by local medium velocity $V(\boldsymbol{r})$ times the time interval Δt. Variable Δt is a pre-specified time interval, expressed as $\Delta t = m * dt$. dt is the sampling time interval and m is an integer
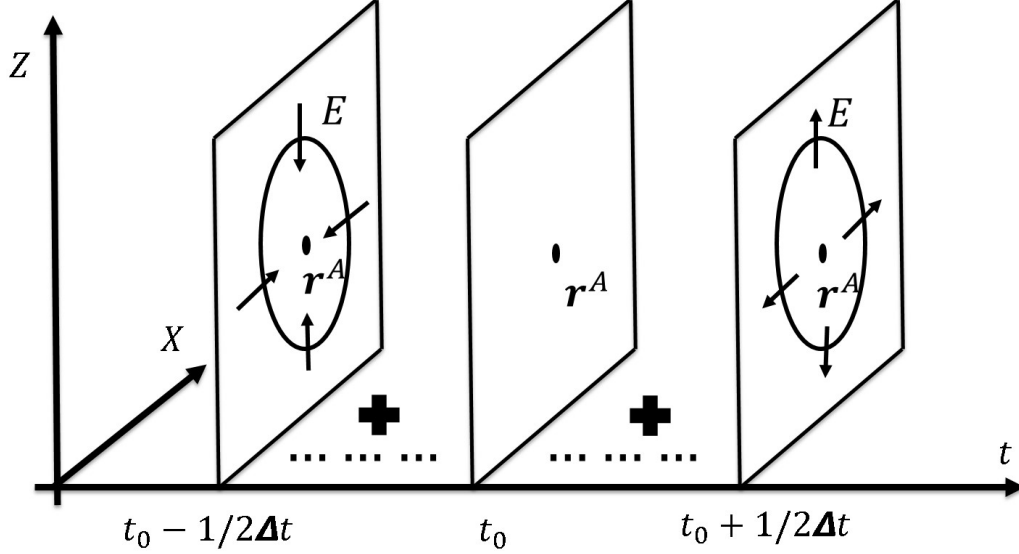
Figure 4.1: Wavefront of each time slice during the back-propagation. z and x are spatial coordinates. t is back-propagation time. The black dot in the center time slice denotes source location and t_0 is source origin time. Circle is wavefront with radius R right before and after origin time t_0. During back-propagation, the wavefront collapses at the source location and then diverges again due to the lack of an elastic sink. E is the total energy on the wave front.

selected to make the largest radii R become approximately equal to or a little smaller than half a dominant wavelength. If we sum the energy going through the predefined circle during the period between time $t_0 - \frac{1}{2}\Delta t$ and $t_0 + \frac{1}{2}\Delta t$, we should get a maximum value corresponding to the true event location $\boldsymbol{r}_0$ and origin time t_0 compared to the summation value at different locations and times. The summation is done through the Hough transform (Li and Van der Baan, 2016).

To calculate the total energy, we apply the concept of energy flux (Synge, 1995), denoted by $\boldsymbol{EF}$, which is the rate of energy transport per unit area. Energy flux is a vector whose components are determined by the normal direction of the measurement area. The first step is to calculate the ith component of the energy flux $EF_i(\boldsymbol{r})$ at an arbitrary time t using

$$EF_i(\boldsymbol{r}, t) = \tau_{ij}(\boldsymbol{r}, t)v_j(\boldsymbol{r}, t), \tag{4.17}$$

where $\tau_{ij}(\boldsymbol{r}, t)$ is the ij^{th} component of the second order stress tensor at location

r and time t; v_j is the jth component of the particle velocity vector (Synge, 1995). We use a staggered grid finite difference code for back-propagation (Pitarka, 1999), where the second order stress tensor $\tau_{ij}(\boldsymbol{r}, t)$ is easily calculated. The absolute value of the energy flux $\mid \boldsymbol{EF}(\boldsymbol{r}, t) \mid$ provides the magnitude of energy passing through the point at $\boldsymbol{r}$ and time t. This way we turn the back-propagated particle velocity map into an energy map. This procedure further justifies use of equation 20 instead 19 for back-propagation since both P- and S-wave energy should collapse onto the event location, assuming correct velocity models. Equation 4.16 is however simpler to implement and thus faster than use of equations 4.12 or 4.13 and 4.14.

Then using the Hough transform, we apply spatially circular summation (Li and Van der Baan, 2016). We sum the back-propagated energy flux $\mid \boldsymbol{EF}^*_{TR} \mid$ along circles with local radius R centered at grid points $\boldsymbol{r}$ at every discrete time point t_n, that is

$$E_H(\boldsymbol{r}, t_n) = \sum_{\boldsymbol{r}_b} \mid \boldsymbol{EF}^*_{TR}(\boldsymbol{r}_b, t_n) \mid, \tag{4.18}$$

where $\boldsymbol{r}_b$ satisfies $|\boldsymbol{r}_b - \boldsymbol{r}| = R$. Physically this step means that we calculate the energy going through the circle centered at $\boldsymbol{r}$ with radius R at time instant t_n.

The next step is to do a temporal summation of image E_H for a time period Δt yielding a Hough map for an arbitrary discrete time point t_H using

$$E_H^{sum}(\boldsymbol{r}, t_H) = \sum_{t_n=t_H-\frac{1}{2}\Delta t}^{t_n=t_H+\frac{1}{2}\Delta t} E_H(\boldsymbol{r}, t_n). \tag{4.19}$$

where the summation is done at sampling time step dt. The Hough map E_H^{sum} is evaluated for determining the most likely source location and origin time. Physically, equation 4.19 determines the total energy going through the pre-defined circle centred at r with radius R during the period Δt. This way, we turn the back-propagation energy image $\mid \boldsymbol{E}_H \mid$ into a summation Hough image E_H^{sum}.

We assume that only a single (passive) event occurs during the period Δt. We save the spatial coordinates of the maximum value in the Hough map as

a function of time t and compute its shortest distance to the receivers. This greatly condenses the information and allows us to select the most likely source locations and origin times without having to save either the Hough map or the back-propagation image at all time instances.

Next, similar to the focusing criterion proposed by Li and Van der Baan (2016), we set a magnitude threshold $\mathbb{T}_M$ and a distance threshold $\mathbb{T}_D$ to automatically select the source position and the origin time. The distance threshold is used to exclude those locations with unreasonable small distances to the receivers, even though the highest magnitude may appear at those locations. In practice, a reasonable distance threshold $\mathbb{T}_D$ is determined by the relative location between the observation well and the treatment well in for instance hydraulic fracturing treatments. Then, tests of the magnitude are often required to determine a proper magnitude threshold $\mathbb{T}_M$ which balances the number of missed events (false negatives) versus number of false alarms (false positives). Finally, the location and corresponding time of all Hough maxima above the magnitude and distance thresholds are extracted as the most likely source positions and origin times.

4.3   Examples

In this section, we apply the proposed method to synthetic data acquired in a borehole and at the surface. We apply temporal second order and spatial fourth order finite differences to do elastic forward modeling and back extrapolation. To mimic a realistic scenario, we use a smoothed velocity model during the back-propagation. This can also prevent the generation of secondary reflections. We wish to explore the possibilities of this imaging method in complex structures, namely the elastic Marmousi velocity model (Versteeg and Grau, 1990, Versteeg and Grau, 1991) and a subduction slab model.

4.3.1   Elastic Marmousi model

The P-wave Marmousi model is shown in Figure 4.2a. The S-wave velocity is $1/\sqrt{3}$ of the P-wave velocity and a constant density of 2.4 g/cm^3 is used in

this example. The model is based on a profile through the North Quenguela trough in the Cuanza basin (Mora, 2002). A vertical borehole is simulated with two scenarios, namely 1) 12 receivers measuring x- and z-component particle velocities only at depths from 500m to 1600m with a spatial interval of 100m (Figure 4.2a) and 2) 8 three-component receivers measuring both x- and z-component particle velocities and y-component rotational rate, whose locations coincide with some of the 12 receivers in the previous scenario except the ones at depths of 700m, 1000m, 1300m and 1500m. The purpose is to keep the total number of traces identical in the two scenarios as well as the same aperture. The source is an double-couple (DC) source with a Ricker wavelet with a peak frequency of 20Hz, representing a horizontally oriented fault plane with horizontal slip direction, located on the right of the well with coordinates (x, z) of (8000m, 1500m). It simulates a microseismic event, caused for instance by an hydraulic fracturing at origin time 0.2s. The total recording time in both scenarios is 3s. The numerical simulation grid spacing is 24m with 1.8ms time intervals. To show the property of the rotational motion recordings, the synthetic data without noise are shown in Figure 4.3. In a homogeneous, isotropic and elastic medium P-waves are rotation free and S-waves have zero divergence (Aldridge and Abbott, 2009). Therefore rotational instruments are significantly less sensitive than particle velocity sensors to P-wave arrivals (Figure 4.3).

For back-propagation, we add Gaussian white noise with a SNR equal to 1 to the original synthetic dataset to test the robustness of our algorithm (Figure 4.4). The SNR is such that most P-waves are barely visible. Next we inject two different combinations of the total wavefields corresponding to different scenarios using equation 20 into a smoothed version of the exact velocity model (Figure 4.2b). The normal vectors are perpendicular to the well, pointing to the left side. Figure 4.5 displays a part of the back-propagated source image starting from 2800m in horizontal direction at the real origin time for the two scenarios. Figures 4.5a correspond to the x and z components of the back-propagated S-wavefields using only the particle velocity data. The back-propagated S-wavefields focus on the true source location (dashed arrow in Figure 4.5a). But at the same time, weaker but still noticeable concentrations can be found on the left side of the well (black arrows in Figure 4.5a). Li

86

and Van der Baan (2016) define these artefacts as ghost foci because they do not actually exist in reality. The ghost foci with such strong magnitudes will bring ambiguity to the interpretation of the true event location. Besides, artifacts in the vicinity of the receivers are also strong due to the existence of noise combined with use of only a few borehole instruments. When we use both the rotational rate and the particle velocity recordings, the ghost foci are significantly suppressed and only the true event location stands out clearly (Figure 4.5b). In addition, the combination of both types of wavefields leads to improved SNR in the final image, in particular around the receiver area.

We then test the ability of the energy flux based focusing criterion for origin time and event location detection when both rotational motion and particle velocity fields are used. During back-propagation, the staggered-grid finite difference modeling algorithm automatically provides the stress field τ_{ij} and the particle velocity wavefield v_j required to calculate energy flux $\boldsymbol{EF}$. Then we apply equations 4.18 and 4.19 to the absolute energy flux map $|\boldsymbol{EF}^*_{TR}|$ to get the Hough map E_H at time t. The back-propagation grid spacing is 24 m and time period Δt for temporal summation is 90 ms. We then save the spatial coordinates of the maximum value in both the Hough map E_H and the envelope of the back-propagated particle velocity map $\boldsymbol{v}^*_{S,n}$ as a function of time t and compute its shortest distance to the receivers before applying the magnitude threshold $\mathbb{T}_M$ and the distance threshold $\mathbb{T}_D$ (Figure 4.6). In this example, we manually set $\mathbb{T}_D$ as 1500m according to the known receiver locations and the approximate event location on the maxima-to-receiver distance plot for the Hough map (Figure 4.6a) and x and z components of back-propagated particle velocities (Figure 4.6c,e). In the example, we save the point with the maximum magnitude on each summation map instead of setting the magnitude threshold $\mathbb{T}_M$ for simplicity. The curve of the maximum magnitude for the Hough image is much smoother than that of the envelop of both components of the particle velocity wavefields, indicating that the Hough image is less sensitive to noise and imaging artifacts. We then zoom in the magnitude plot to a smaller range (Figure 4.7). The local maximum in the Hough map occurs at 0.2 s at the true origin time (Figure 4.7a), whereas the maximum in the particle velocity wavefields envelope happens at 0.27s and 0.225s respectively (Figure 4.7b and
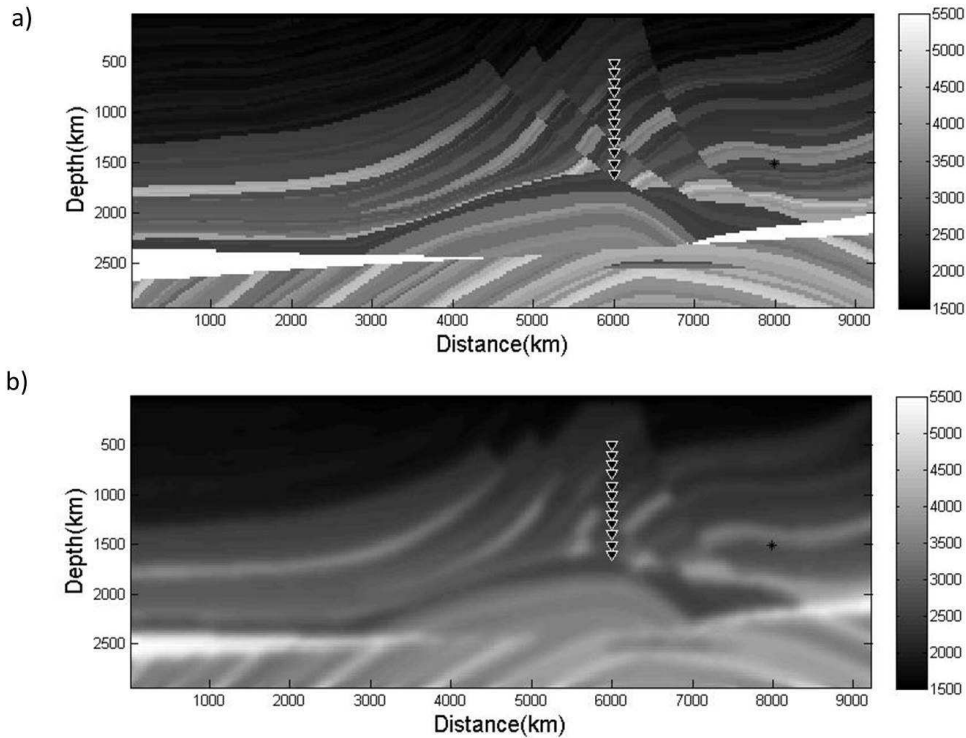
Figure 4.2: 2D elastic P-wave Marmousi velocity model. triangles: receivers. Cross: a double-couple (DC) source. a: true velocity model for forward modeling, b: smoothed velocity model for back-propagation.

c). Performance of the Hough transform to detect microseismic event locations and origin times improves further with an increasing number of instruments since this eliminates acquisition footprints and wavefield aliasing.

4.3.2 Subduction slab model

Our second example simulates an earthquake within a subducting slab recorded at the surface. Here we test the ability of the focusing criterion for earthquake imaging with a highly noisy and sparsely acquired dataset. The subduction slab normally has a higher velocity than its surrounding layers (Stern, 2002). Based on this property, we build a simplified subduction slab model for this example. Figure 4.8a is the true velocity model with P- and S-wave velocities indicated in the figure. The model size is 30km by 30km, with a surface recording array buried 10m below free surface. Similar to the previous example, two combinations of receivers are compared, namely 1) 42 receivers measuring x-
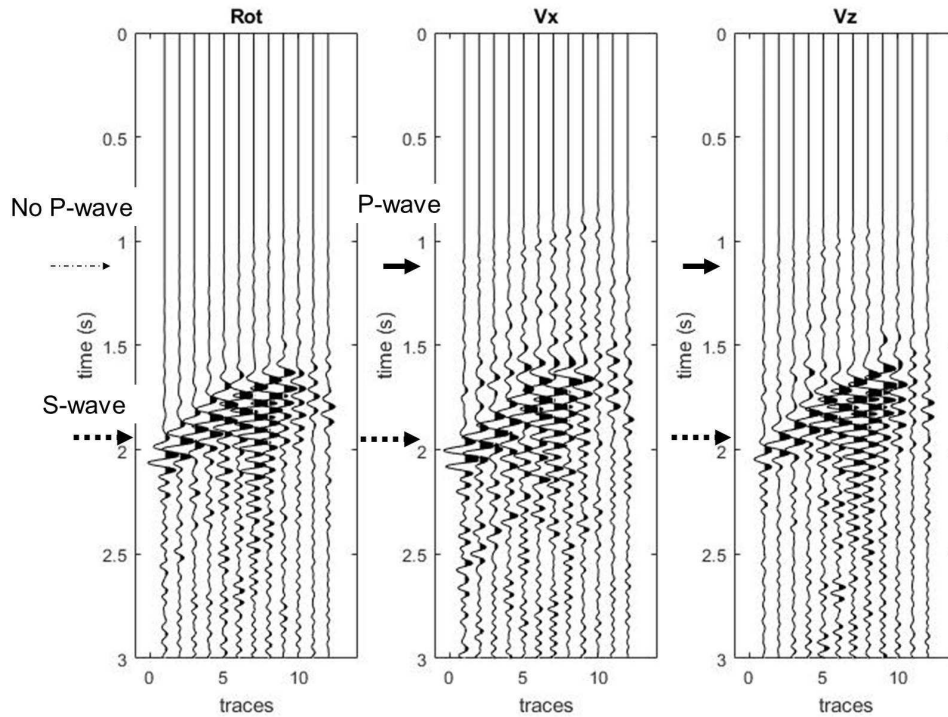
Figure 4.3: Synthetic seismic records without noise. $'Rot'$ is the short form of rotational motion around y direction in this example. $'V_x'$ and $'V_z'$ are the particle velocities in x and z directions. Thin dashed arrow denotes the absence of the P-wave arrival in rotational recordings. Short solid lines denote the main P-wave arrivals in the particle velocity recordings. The long dashed lines denote the principal S-wave arrivals in all three recordings.
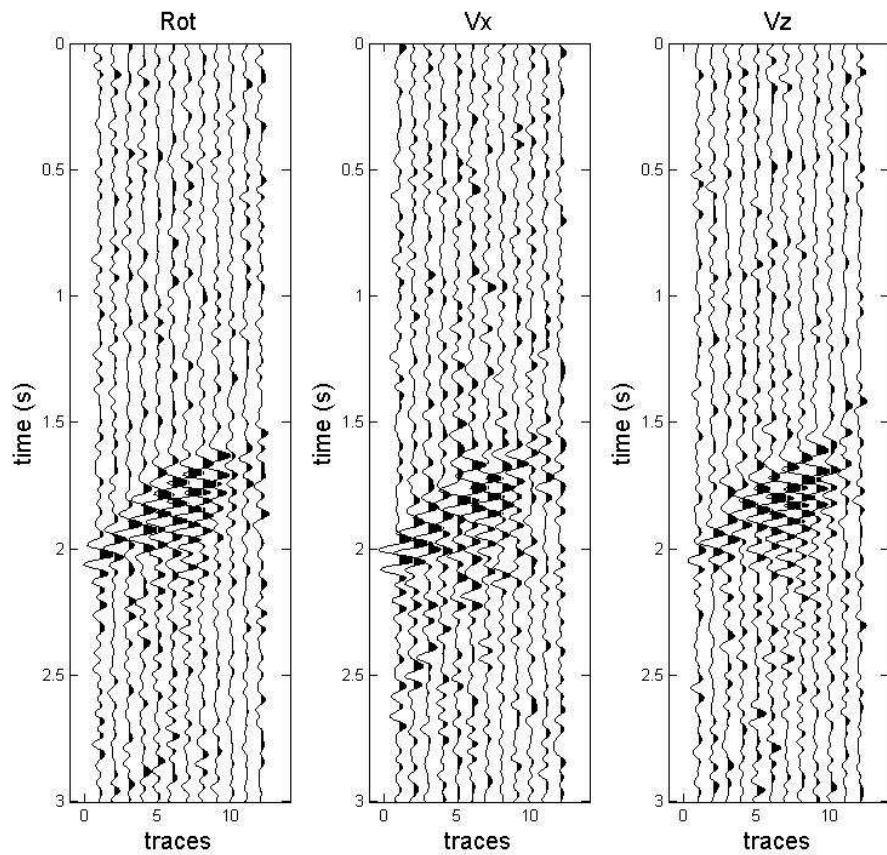
Figure 4.4: Synthetic seismic records with Gaussian white noise. $'Rot'$ is the short form of rotational motion around y direction in this example. $'V_x'$ and $'V_z'$ are the particle velocities in x and z directions. The P-wave is barely seen in $'V_x'$ and $'V_z'$ due to the presence of the noise.
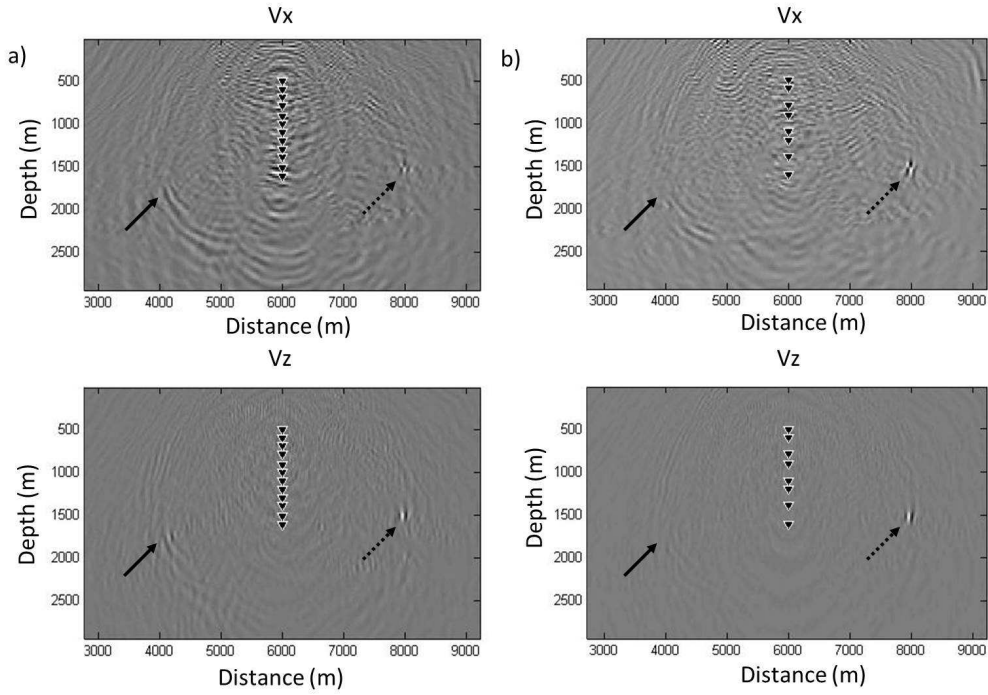
Figure 4.5: Comparison of x (top row) and z (bottom row) components of the back-propagated S-wave particle velocity wavefields using two combinations of recordings. a): only x and z components of particle velocity recordings. b): both particle velocity and rotational motion recordings. Triangle: receivers. Black star: true event location. Ghost focusings appear in a) pointed by black solid arrows whereas only true event location is revealed in b). Artefacts (black ellipses) in vicinity of receivers in b) are more suppressed than in a).
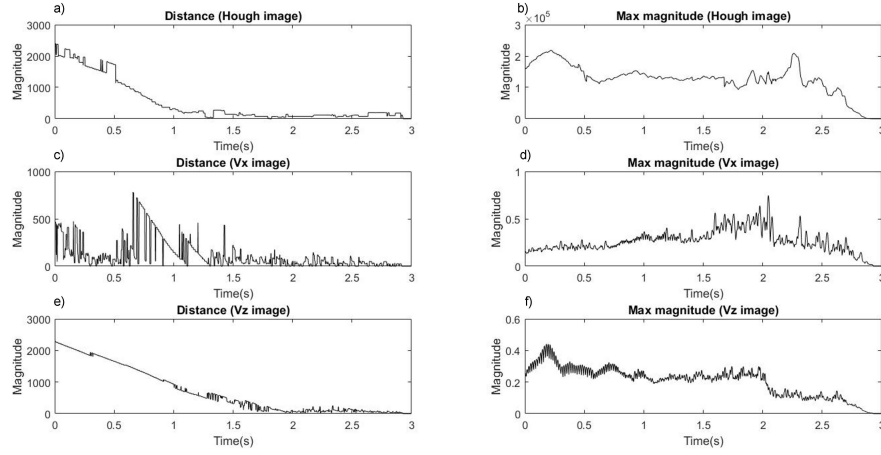
Figure 4.6: Event detection criteria using maxima in Hough map (a and b) or maxima in wavefield envelopes (c, d, e and f). a): Distance of detected maximum to nearest receiver as a function of time from Hough images; c) and e): Distance of detected maximum to nearest receiver as a function of time from x and z components of back-propagated particle velocity images. A minimum threshold $\mathbb{T}_D$ of 1500m is set. All smaller distances are discarded. b): Maximum value as a function time from Hough images; d) and f): Maximum value as a function of time from x and z components of back-propagated particle velocity images.
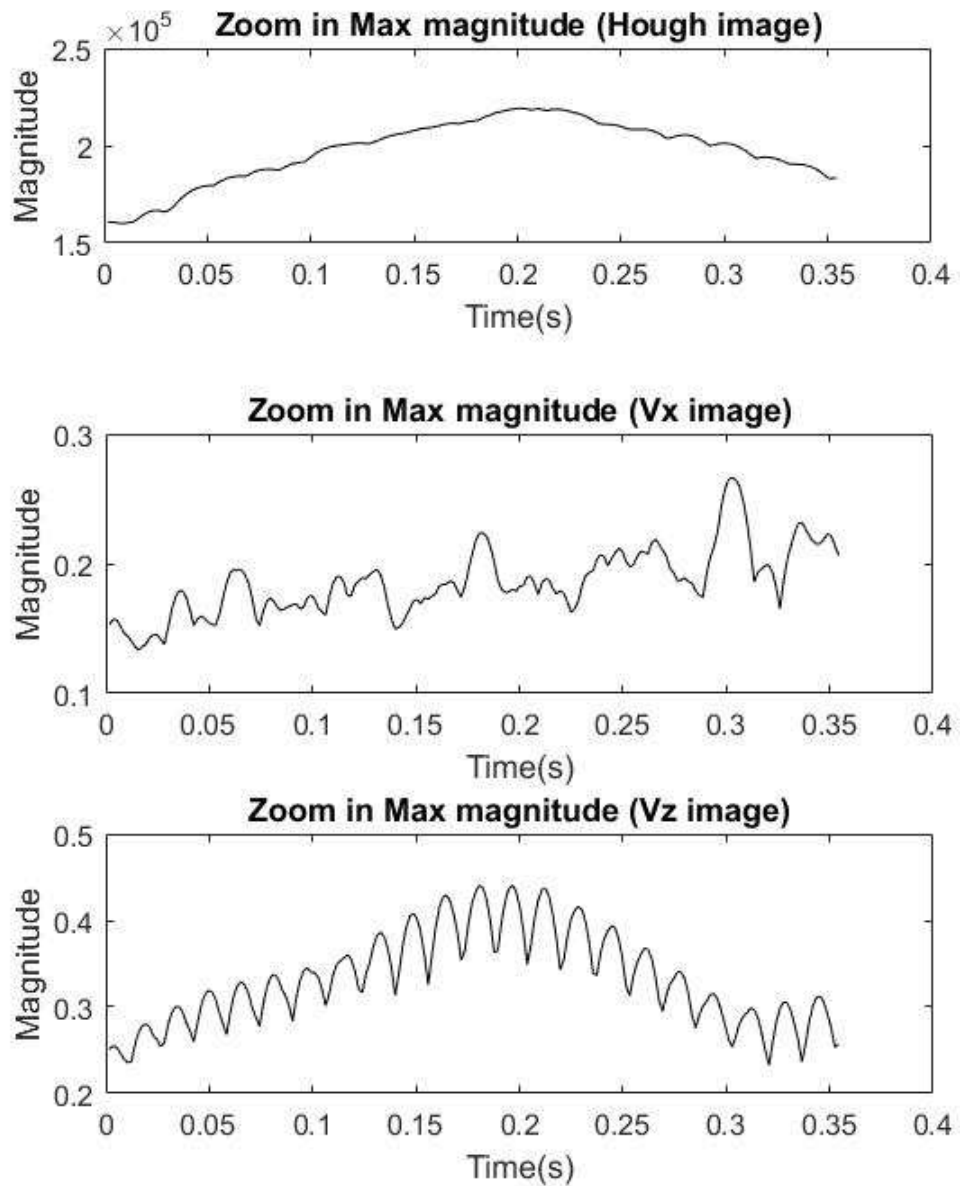
Figure 4.7: Zoom in of magnitude plot in Figure 4.6 from 0s to 0.35s. a): Hough image; maximum is right at 0.2s; b): x component of particle velocity image; maximum is at 0.27s; c): z component of particle velocity image; maxiumum is at 0.225s.

and z-component particle velocities with spatial interval of 50m (Figure 4.2a) and 2) 28 three-component receivers measuring both x- and z-component particle velocities and y-component rotational rate. The white area in the model represents the subduction slab, with a double-couple earthquake happening on top of the slab. The sliding plane of the earthquake is coincident with the top plane of the subduction slab for simplicity. The earthquake is located at a depth of 21.5km and in the center of the model ($x = 15$km), with a dominant frequency of 10Hz and origin time of 1s. Both the rotational motion around the y axis and the particle velocities in the x and z direction are measured at each receiver, with a total recording time of 15s. We add strong bandpassed white noise to the original synthetic data to create noise contaminated data with a SNR of 0.1dB (Figure 4.9). Contrary to the previous example the P-waves remain visible on the z-component. This allows us to test the performance of equation 4.16 in the absence of P/S-wavefield separation.

In the back-propagation stage, two combinations of recordings are injected into a smoothed velocity model (Figure 4.8b) using our proposed method, followed by a comparison between the resulting source images (Figure 4.10). It can be seen that the source images obtained from the back-propagation of the combination with rotational rate (Figure 4.10b) is highly similar to the one using two-component particle velocities only (Figure 4.10a), which indicates that rotational component can aid in the passive source imaging even when the number of receivers are largely reduced.

We then test the proposed focusing criterion. We first compare the maximum magnitude plots of the Hough image and the two-component back-propagation wavefields (Figure 4.11). The corresponding estimated time point of the peak on the Hough image plot appears at 1s, which is the accurate origin time, whereas the corresponding time points on the wavefield plots are 1.32s and 1.05s respectively, due to the noise disturbance. We show the back-propagated S-wave x- and z-component particle velocity wavefields at the estimated time point (Figure 4.12a). Even though noisy data are used, we get focusing at the true location for both the x- and z-component particle velocity images. We also show the estimated particle velocity wavefields based on only the maximum magnitude criterion of the envelop of the particle velocity maps (Figure

94
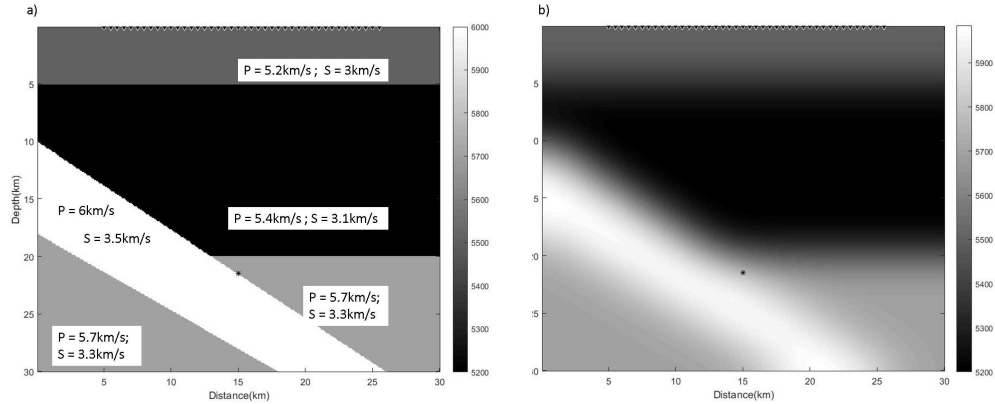
Figure 4.8: 2D elastic subduction slab velocity model. triangles: receivers. Star: a double-couple (DC) source. a): true velocity model for forward modeling; P- and S-wave velocities are denoted on the model, b): smoothed velocity model for back-propagation.

4.12b). The estimated event locations in both the x- and z-component wavefields are shifted from the true event location leading to a predicted source location 1km above the true one (Figure 4.11 middle and bottom). This would place the event above the subducting slab.

4.4 Discussion

Rotational motion recordings are a strong supplement to the particle velocity recordings (Li and Van der Baan, 2017). The combined analysis of both rotational motion and the particle displacement/velocity has many applications in exploration geophysics, such as wavefield reconstruction (Muyzert et al., 2012) and ground roll removal (Barak et al., 2014). It is likely that it may also find application in other fields where elastic waves are used for imaging (Li and Van der Baan, 2017). A practical challenge is the current scarcity in suitable recording equipment (Van Driel et al., 2012).

Rotational rate recordings provide information on the spatial derivatives of the particle velocity wavefield, which aids in wavefield extrapolation. Elastic-representation-theorem based reverse time extrapolation requires the spatial gradient of the particle displacement/velocity field, which could either be approximated by finite differentiation between sensors using receiver groups or a
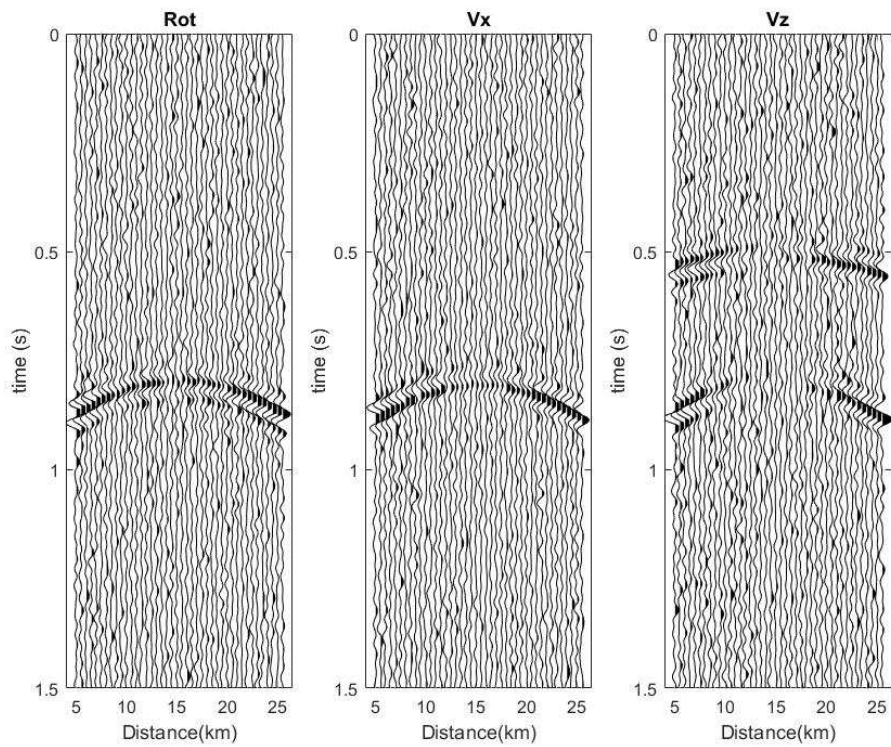
Figure 4.9: Synthetic seismic records with noise for subduction slab velocity model. Rot is the short form of rotational motion around y direction in this example. V_x and V_z are the particle velocities in x and z directions.
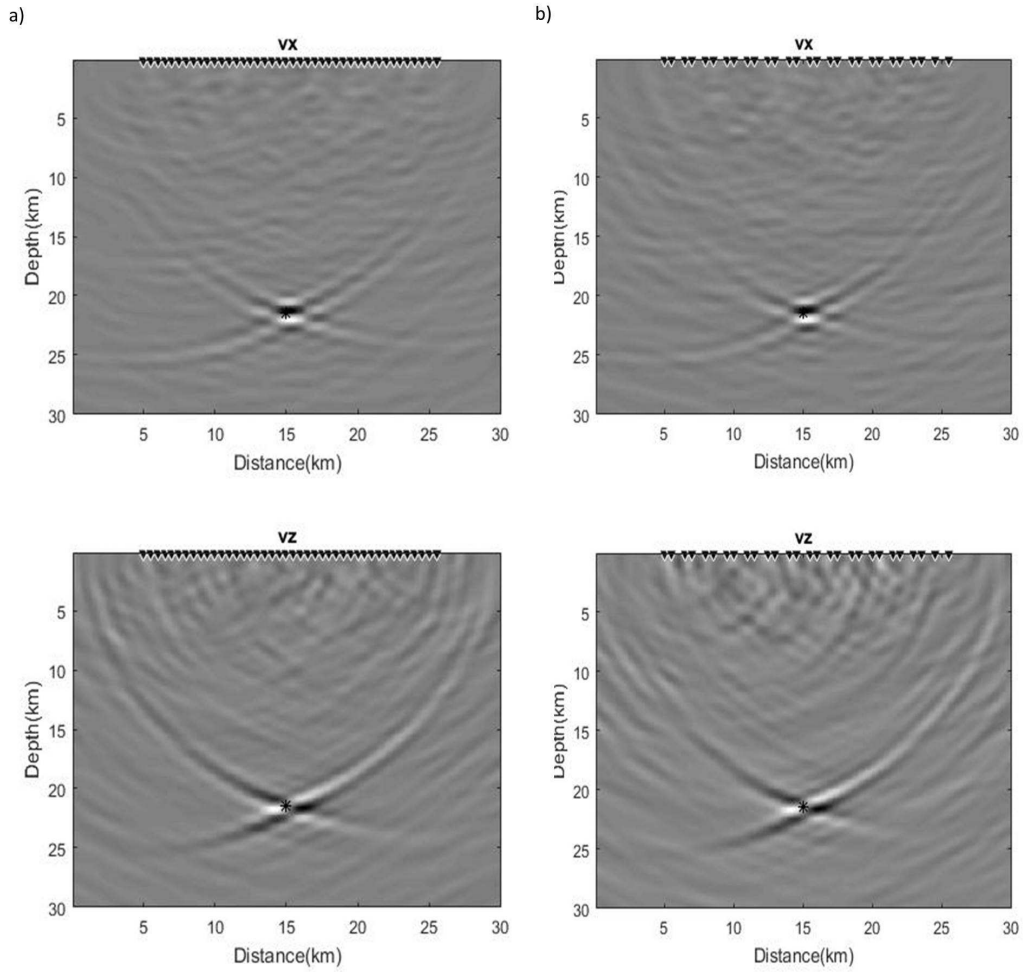
Figure 4.10: Comparison of x (top row) and z (bottom row) components of the back-propagated S-wave particle velocity wavefields using two combinations of recordings. a): only x and z components of particle velocity recordings. b): both particle velocity and y-component rotational rate recordings. Triangle: receivers. Black star: true event location. Both a) and b) have similar back-propagated source images, even though the number of receivers in b) is less than that in a).
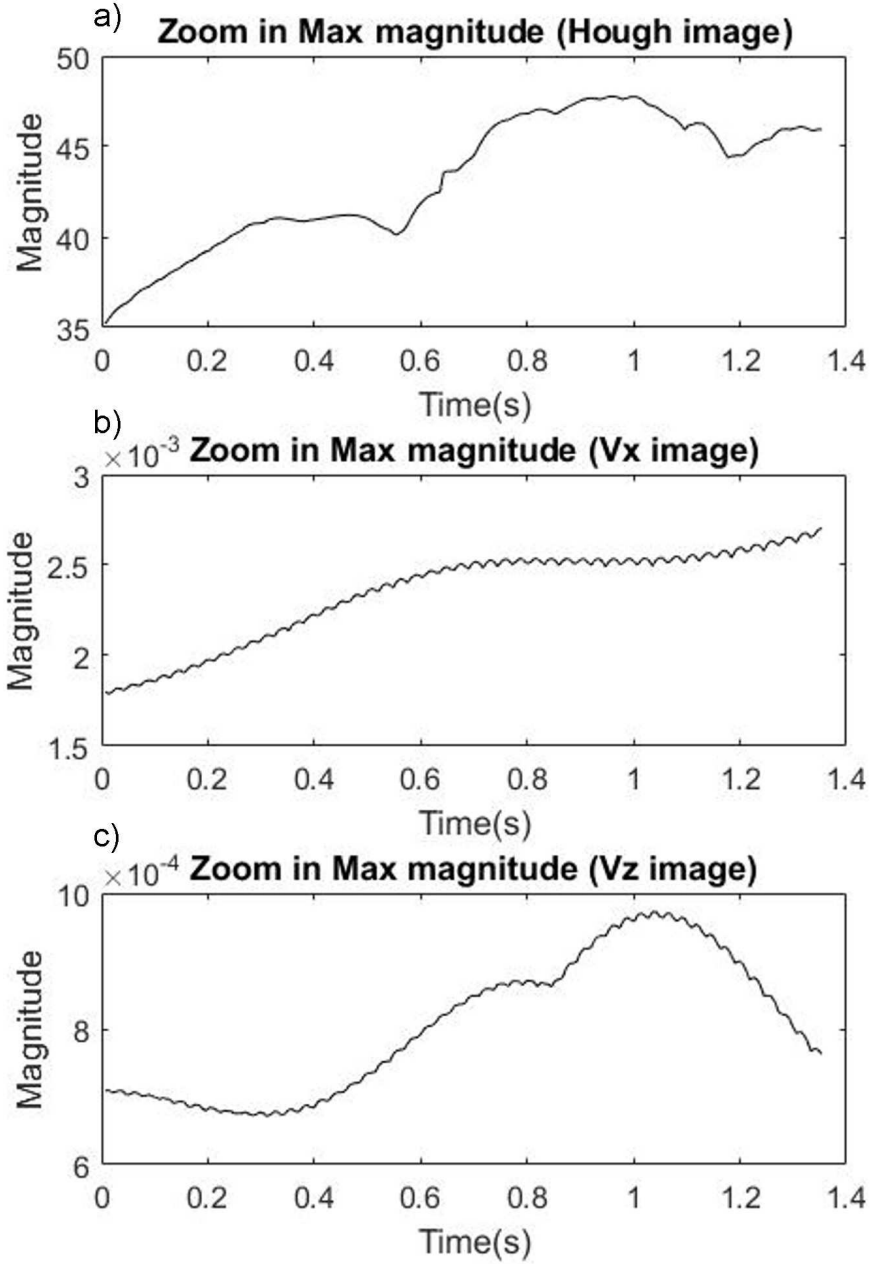
Figure 4.11: Event detection criteria using maxima in Hough map (a) or maxima in wavefield envelopes (b and c). Maximum value as a function of time. a): Extracted maxima from the Hough map. b) and c): Extracted maxima from the back-propagated particle velocity V_x and V_z images. Local Hough maximum is at the true origin time of 1s, contrary to maximum of the particle velocity wavefields.
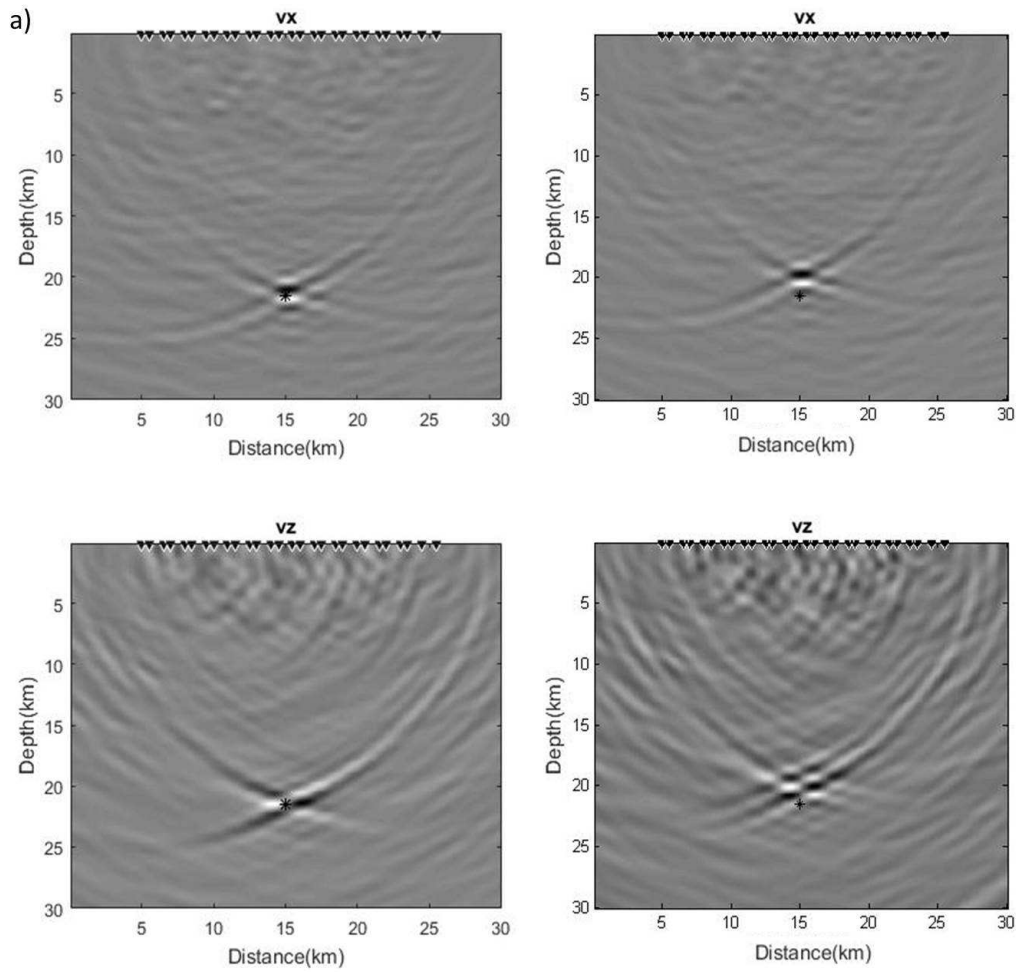
Figure 4.12: The back-propagated x- (left column) and z-component (right column) particle velocity wavefields using (a) the energy based focusing criterion at the estimated origin times 1s and (b) the magnitude criterion at the estimated origin time 1.32s (V_x) and 1.05s (V_z) . Star: true event location.

far-field approximation is included to remove this term (Wapenaar and Fokkema, 2006). Equation 4.11 provides the required gradient information by directly including rotational motions which can be recorded separately. This makes the technique in principle less sensitive to recorded noise. Li and Van der Baan (2016) discuss in general terms the effect of both the acquisition geometry and precision of the velocity field on image quality.

In this paper, we build the elastic representation theorem based on the homogeneous isotropic elastic wave equation (Equation 4.1) because it is a simple wave equation that directly involves rotation rate as S-wave potential $\boldsymbol{\nabla} \times \boldsymbol{v}$. The theorem shows that in an isotropic, homogeneous medium, P- and S-waves can be back-propagated separately. The measurements of rotational rate only contribute in the construction of shear wavefields, which is normally dominant in passive seismic recordings. In some cases, such as microseismic monitoring using vertical-component surface arrays, the P-wave is the dominant recorded wave (Duncan and Eisner, 2010), which could then be back-propagated with equation 4.13 where we use the full Green's function $\boldsymbol{G}_v$ and the full wavefield $\boldsymbol{v}$ instead of the P-wave equivalents, analagous to the substitutions to obtain equation 4.15 from 4.14. Moreover, although the proposed method is derived under homogeneous circumstances, examples indicate that it is also applicable for inhomogeneous velocity models. Yet, it remains an open question if the procedure is also applicable to anisotropic media. Pham et al. (2010) have numerically shown that the magnitude of rotation rates in anisotropic media is large enough to invert for medium properties, indicating the rotational sensors are likely to pick up P-waves in anisotropic media.

Furthermore it is important to emphasize that recorded data should only consist of body waves; that is, all surface and interface waves must be removed first. For instance, tube waves may be generated due to body waves impinging on a borehole(Dayley et al., 2003, Vaezi and Van der Baam, 2015). If left untouched these will generate undesirable artifacts in the back-propagated images. The same holds true for unremoved surface waves in surface-array data.

The energy flux based focusing criterion is a more promising general focusing criterion than amplitude-based ones. Different from the particle velocity
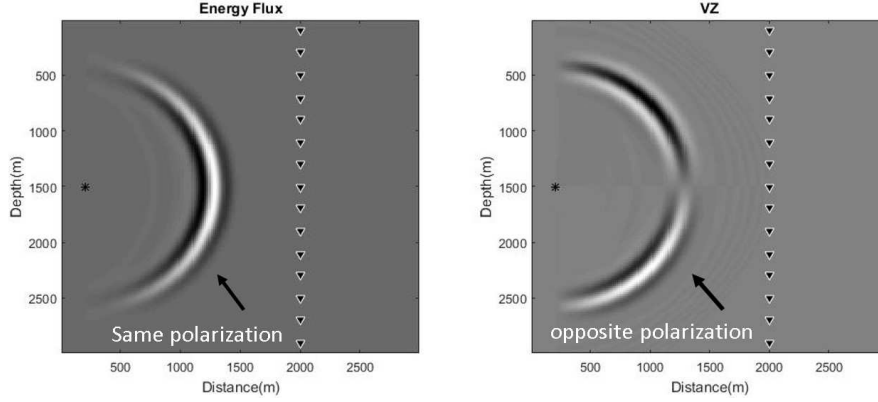
Figure 4.13: Amplitudes for a) energy flux and b) vertical component of particle velocity. Black star: Double-couple source (shear failure). triangles: receivers. Energy flux has the same polarization along the entire wavefront, whereas the amplitudes of the up and downgoing wavefields have opposite polarity.

wavefield, the energy flux is directly related to the wave propagation direction, which is physically more pertinent for event localization. Also amplitude-based summation may fail because of the non-isotropic source mechanisms, invoking polarity changes depending on radiation directions (Chambers et al., 2010, Chambers et al., 2014,Li and Van der Baan, 2016). The magnitude of the back-propagated wavefields may have opposite polarization which cancel each other during summation along the wavefront as shown in Figure 4.13b. Because energy flux is only sensitive to wave propagation direction, for a fixed acquisition system, the back-propagation results are the same with different source mechanisms, providing more stable results compared to amplitude-based summation (Figure 4.13a). Energy flux can be used for both elastic and acoustic data. In the acoustic case, equation 4.17 is replaced by $EF_i = p \times v_i$ with p is pressure and v_i is the ith component of the particle velocity $\boldsymbol{v}$. The Hough transform procedure remains otherwise unchanged.

4.5   Conclusion

Rotational motion provides information on the spatial gradient of the particle velocity wavefields. The introduced elastic representation-theorem-based time-

reversal extrapolation equation uses explicitly recordings from rotational and particle displacement/velocity sensors simultaneously or separately, leading to enhanced imaging results. The energy flux based Hough map provides a convenient and stable criterion for automatically detecting both event locations and origin times.

4.6 Appendix: Derivation of Equation 4.12

Since for a homogeneous, isotropic medium, P- and S-waves are decoupled when radiated from a source, the elastic wave equation 4.5 can be written into a pair of equations corresponding to P- and S-waves, given by

$$- \omega^2 \hat{\boldsymbol{v}}^p(\boldsymbol{r}, \boldsymbol{r}^A, \omega) = \alpha^2 \boldsymbol{\nabla} \boldsymbol{\nabla} \cdot \hat{\boldsymbol{v}}^p(\boldsymbol{r}, \boldsymbol{r}^A, \omega) + \left[\hat{\dot{\boldsymbol{F}}}(\omega) \right]_p \delta(\boldsymbol{r} - \boldsymbol{r}^A), \qquad (4.20)$$

$$- \omega^2 \hat{\boldsymbol{v}}^s(\boldsymbol{r}, \boldsymbol{r}^A, \omega) = -2\beta^2 \boldsymbol{\nabla} \times \hat{\dot{\boldsymbol{\Omega}}}(\boldsymbol{r}, \boldsymbol{r}^A, \omega) + \left[\hat{\dot{\boldsymbol{F}}}(\omega) \right]_s \delta(\boldsymbol{r} - \boldsymbol{r}^A), \qquad (4.21)$$

where $\hat{\boldsymbol{v}}^p$ and $\hat{\boldsymbol{v}}^s$ are P- and S-wave particle velocities, satisfying $\hat{\boldsymbol{v}} = \hat{\boldsymbol{v}}^p + \hat{\boldsymbol{v}}^s$; $\left[\hat{\dot{\boldsymbol{F}}}(\omega) \right]_p$ and $\left[\hat{\dot{\boldsymbol{F}}}(\omega) \right]_s$ are the decoupled source terms contributing solely to P- and S-waves respectively, fulfilling $\hat{\dot{\boldsymbol{F}}}(\omega) = \left[\hat{\dot{\boldsymbol{F}}}(\omega) \right]_p + \left[\hat{\dot{\boldsymbol{F}}}(\omega) \right]_s$.

Likewise, equation 4.6 can be written into

$$- \omega^2 \hat{\boldsymbol{G}}^*_{\boldsymbol{v}^p,n}(\boldsymbol{r}, \boldsymbol{r}^B, \omega) = \alpha^2 \boldsymbol{\nabla} \boldsymbol{\nabla} \cdot \hat{\boldsymbol{G}}^*_{\boldsymbol{v}^p,n}(\boldsymbol{r}, \boldsymbol{r}^B, \omega) + [\hat{\boldsymbol{x}}_n]_p \, \delta(\boldsymbol{r} - \boldsymbol{r}^B), \qquad (4.22)$$

$$- \omega^2 \hat{\boldsymbol{G}}^*_{\boldsymbol{v}^s,n}(\boldsymbol{r}, \boldsymbol{r}^B, \omega) = -2\beta^2 \boldsymbol{\nabla} \times \hat{\boldsymbol{G}}^*_{\dot{\boldsymbol{\Omega}},n}(\boldsymbol{r}, \boldsymbol{r}^B, \omega) + [\hat{\boldsymbol{x}}_n]_s \, \delta(\boldsymbol{r} - \boldsymbol{r}^B), \qquad (4.23)$$

where $\hat{\boldsymbol{G}}^*_{\boldsymbol{v}^p,n}$ and $\hat{\boldsymbol{G}}^*_{\boldsymbol{v}^s,n}$ are the Green's functions for P- and S-wave particle velocities from a unit force $\hat{\boldsymbol{x}}_n$ at the nth direction; $[\hat{\boldsymbol{x}}_n]_p$ and $[\hat{\boldsymbol{x}}_n]_s$ are the portions of the unit force $\hat{\boldsymbol{x}}_n$ exciting P- and S-waves only. They also satisfy $\hat{\boldsymbol{G}}^*_{\boldsymbol{v},n} = \hat{\boldsymbol{G}}^*_{\boldsymbol{v}^p,n} + \hat{\boldsymbol{G}}^*_{\boldsymbol{v}^s,n}$ and $\hat{\boldsymbol{x}}_n = [\hat{\boldsymbol{x}}_n]_p + [\hat{\boldsymbol{x}}_n]_s$.

We use the denotation $[.]_p$ and $[.]_s$ around the force terms to indicate that P- and S-wave separation is applied immediately upon excitation of the specified force within the brackets. These terms can thus be identified with the resulting

wavefields due to P- and S-wave force potentials as used in Wapenaar and Haime (1990).

We then start deriving equation 4.12 from the left-hand-side of equation 4.9, given by

$$
\int_{\mathbb{D}} \left[\hat{\boldsymbol{G}}_{\boldsymbol{v},n}^{*}(\boldsymbol{r}, \boldsymbol{r}^{B}, \omega) \cdot \hat{\dot{\boldsymbol{F}}}(\omega) \delta(\boldsymbol{r} - \boldsymbol{r}^{A}) - \hat{\boldsymbol{v}}(\boldsymbol{r}, \boldsymbol{r}^{A}, \omega) \cdot \hat{\boldsymbol{x}}_{n} \delta(\boldsymbol{r} - \boldsymbol{r}^{B}) \right] dV
$$

$$
= \int_{\mathbb{D}} \left(\hat{\boldsymbol{G}}_{\boldsymbol{v}^{p},n}^{*}(\boldsymbol{r}, \boldsymbol{r}^{B}, \omega) + \hat{\boldsymbol{G}}_{\boldsymbol{v}^{s},n}^{*}(\boldsymbol{r}, \boldsymbol{r}^{B}, \omega) \right) \cdot \left(\left[\hat{\dot{\boldsymbol{F}}}(\omega) \right]_{p} + \left[\hat{\dot{\boldsymbol{F}}}(\omega) \right]_{s} \right) \delta(\boldsymbol{r} - \boldsymbol{r}^{A}) dV
$$

$$
- \int_{\mathbb{D}} \left(\hat{\boldsymbol{v}}^{p}(\boldsymbol{r}, \boldsymbol{r}^{A}, \omega) + \hat{\boldsymbol{v}}^{s}(\boldsymbol{r}, \boldsymbol{r}^{A}, \omega) \right) \cdot \left([\hat{\boldsymbol{x}}_{n}]_{p} + [\hat{\boldsymbol{x}}_{n}]_{s} \right) \delta(\boldsymbol{r} - \boldsymbol{r}^{B}) dV
$$

$$
= \int_{\mathbb{D}} \left[\hat{\boldsymbol{G}}_{\boldsymbol{v}^{p},n}^{*}(\boldsymbol{r}, \boldsymbol{r}^{B}, \omega) \cdot \left[\hat{\dot{\boldsymbol{F}}}(\omega) \right]_{p} \delta(\boldsymbol{r} - \boldsymbol{r}^{A}) - \hat{\boldsymbol{v}}^{p}(\boldsymbol{r}, \boldsymbol{r}^{A}, \omega) \cdot [\hat{\boldsymbol{x}}_{n}]_{p} \delta(\boldsymbol{r} - \boldsymbol{r}^{B}) \right] dV
$$

$$
+ \int_{\mathbb{D}} \left[\hat{\boldsymbol{G}}_{\boldsymbol{v}^{s},n}^{*}(\boldsymbol{r}, \boldsymbol{r}^{B}, \omega) \cdot \left[\hat{\dot{\boldsymbol{F}}}(\omega) \right]_{s} \delta(\boldsymbol{r} - \boldsymbol{r}^{A}) - \hat{\boldsymbol{v}}^{s}(\boldsymbol{r}, \boldsymbol{r}^{A}, \omega) \cdot [\hat{\boldsymbol{x}}_{n}]_{s} \delta(\boldsymbol{r} - \boldsymbol{r}^{B}) \right] dV
$$

$$
+ \int_{\mathbb{D}} \left[\hat{\boldsymbol{G}}_{\boldsymbol{v}^{p},n}^{*}(\boldsymbol{r}, \boldsymbol{r}^{B}, \omega) \cdot \left[\hat{\dot{\boldsymbol{F}}}(\omega) \right]_{s} \delta(\boldsymbol{r} - \boldsymbol{r}^{A}) - \hat{\boldsymbol{v}}^{p}(\boldsymbol{r}, \boldsymbol{r}^{A}, \omega) \cdot [\hat{\boldsymbol{x}}_{n}]_{s} \delta(\boldsymbol{r} - \boldsymbol{r}^{B}) \right] dV
$$

$$
+ \int_{\mathbb{D}} \left[\hat{\boldsymbol{G}}_{\boldsymbol{v}^{s},n}^{*}(\boldsymbol{r}, \boldsymbol{r}^{B}, \omega) \cdot \left[\hat{\dot{\boldsymbol{F}}}(\omega) \right]_{p} \delta(\boldsymbol{r} - \boldsymbol{r}^{A}) - \hat{\boldsymbol{v}}^{s}(\boldsymbol{r}, \boldsymbol{r}^{A}, \omega) \cdot [\hat{\boldsymbol{x}}_{n}]_{p} \delta(\boldsymbol{r} - \boldsymbol{r}^{B}) \right] dV,
$$

$$(4.24)$$

where the cross terms mixing P- and S-waves equal zero, because P- and S-wave sources have no contributions to S- and P-waves respectively in a homogeneous, isotropic medium, yielding

$$
\int_{\mathbb{D}} \left[\hat{\boldsymbol{G}}_{\boldsymbol{v},n}^{*}(\boldsymbol{r}, \boldsymbol{r}^{B}, \omega) \cdot \hat{\dot{\boldsymbol{F}}}(\omega) \delta(\boldsymbol{r} - \boldsymbol{r}^{A}) - \hat{\boldsymbol{v}}(\boldsymbol{r}, \boldsymbol{r}^{A}, \omega) \cdot \hat{\boldsymbol{x}}_{n} \delta(\boldsymbol{r} - \boldsymbol{r}^{B}) \right] dV
$$

$$
= \int_{\mathbb{D}} \hat{\boldsymbol{G}}_{\boldsymbol{v}^{p},n}^{*}(\boldsymbol{r}, \boldsymbol{r}^{B}, \omega) \cdot \left[\hat{\dot{\boldsymbol{F}}}(\omega) \right]_{p} \delta(\boldsymbol{r} - \boldsymbol{r}^{A}) - \hat{\boldsymbol{v}}^{p}(\boldsymbol{r}, \boldsymbol{r}^{A}, \omega) \cdot [\hat{\boldsymbol{x}}_{n}]_{p} \delta(\boldsymbol{r} - \boldsymbol{r}^{B}) dV
$$

$$
+ \int_{\mathbb{D}} \hat{\boldsymbol{G}}_{\boldsymbol{v}^{s},n}^{*}(\boldsymbol{r}, \boldsymbol{r}^{B}, \omega) \cdot \left[\hat{\dot{\boldsymbol{F}}}(\omega) \right]_{s} \delta(\boldsymbol{r} - \boldsymbol{r}^{A}) - \hat{\boldsymbol{v}}^{s}(\boldsymbol{r}, \boldsymbol{r}^{A}, \omega) \cdot [\hat{\boldsymbol{x}}_{n}]_{s} \delta(\boldsymbol{r} - \boldsymbol{r}^{B}) dV
$$

$$(4.25)$$

Then, we multiply equations 4.20 and 4.22 with $\hat{\boldsymbol{G}}_{\boldsymbol{v}^{p},n}^{*}(\boldsymbol{r}, \boldsymbol{r}^{B}, \omega)$ and $\hat{\boldsymbol{v}}^{p}(\boldsymbol{r}, \boldsymbol{r}^{A}, \omega)$ respectively, followed by a subtraction of the resulting equations and a body

integration, given by

$$
\int_{\mathbb{D}} \left[\hat{\boldsymbol{G}}^*_{\boldsymbol{v}^p,n}(\boldsymbol{r},\boldsymbol{r}^B,\omega) \cdot \left[\hat{\tilde{\boldsymbol{F}}}(\omega)\right]_p \delta(\boldsymbol{r}-\boldsymbol{r}^A) - \hat{\boldsymbol{v}}^{\boldsymbol{p}}(\boldsymbol{r},\boldsymbol{r}^A,\omega) \cdot [\hat{\boldsymbol{x}}_n]_p \delta(\boldsymbol{r}-\boldsymbol{r}^B) \right] dV
$$
$$
= \alpha^2 \int_{\mathbb{D}} \left[\hat{\boldsymbol{v}}^{\boldsymbol{p}}(\boldsymbol{r},\boldsymbol{r}^A,\omega) \cdot \boldsymbol{\nabla}\boldsymbol{\nabla} \cdot \hat{\boldsymbol{G}}^*_{\boldsymbol{v}^p,n}(\boldsymbol{r},\boldsymbol{r}^B,\omega) - \hat{\boldsymbol{G}}^*_{\boldsymbol{v}^p,n}(\boldsymbol{r},\boldsymbol{r}^B,\omega) \cdot \boldsymbol{\nabla}\boldsymbol{\nabla} \cdot \hat{\boldsymbol{v}}^{\boldsymbol{p}}(\boldsymbol{r},\boldsymbol{r}^A,\omega) \right] dV.
$$

$$(4.26)$$

Similarly, we multiply equations 4.21 and 4.23 with $\hat{\boldsymbol{G}}^*_{\boldsymbol{v}^s,n}(\boldsymbol{r},\boldsymbol{r}^B,\omega)$ and $\hat{\boldsymbol{v}}^s(\boldsymbol{r},\boldsymbol{r}^A,\omega)$ respectively, and follow a similar procedure as before to obtain

$$
\int_{\mathbb{D}} \left(\hat{\boldsymbol{G}}^*_{\boldsymbol{v}^s,n}(\boldsymbol{r},\boldsymbol{r}^B,\omega) \cdot \left[\hat{\tilde{\boldsymbol{F}}}(\omega)\right]_s \delta(\boldsymbol{r}-\boldsymbol{r}^A) - \hat{\boldsymbol{v}}^s(\boldsymbol{r},\boldsymbol{r}^A,\omega) \cdot [\hat{\boldsymbol{x}}_n]_s \delta(\boldsymbol{r}-\boldsymbol{r}^B) \right) dV
$$
$$
= 2\beta^2 \int_{\mathbb{D}} \left(\hat{\boldsymbol{G}}^*_{\boldsymbol{v}^s,n}(\boldsymbol{r},\boldsymbol{r}^B,\omega) \cdot \boldsymbol{\nabla} \times \hat{\dot{\boldsymbol{\Omega}}}(\boldsymbol{r},\boldsymbol{r}^A,\omega) - \hat{\boldsymbol{v}}^s(\boldsymbol{r},\boldsymbol{r}^A,\omega) \cdot \boldsymbol{\nabla} \times \hat{\boldsymbol{G}}^*_{\dot{\boldsymbol{\Omega}},n}(\boldsymbol{r},\boldsymbol{r}^B,\omega) \right) dV.
$$

$$(4.27)$$

Then, equation 4.12 is derived by substituting equations 4.26 and 4.27 into equation 4.25, followed by an application of the Stokes' theorem, giving

$$
\hat{v}^*_n(\boldsymbol{r}^B,\boldsymbol{r}^A,\omega) - \hat{v}_n(\boldsymbol{r}^B,\boldsymbol{r}^A,\omega) =
$$
$$
\int_{\partial\mathbb{D}} \mathbf{n} \cdot \alpha^2 \left[\hat{\boldsymbol{v}}^{\boldsymbol{p}}(\boldsymbol{r},\boldsymbol{r}^A,\omega) \left(\boldsymbol{\nabla} \cdot \hat{\boldsymbol{G}}^*_{\boldsymbol{v}^p,n}(\boldsymbol{r},\boldsymbol{r}^B,\omega) \right) - \hat{\boldsymbol{G}}^*_{\boldsymbol{v}^p,n}(\boldsymbol{r},\boldsymbol{r}^B,\omega) \left(\boldsymbol{\nabla} \cdot \hat{\boldsymbol{v}}^{\boldsymbol{p}}(\boldsymbol{r},\boldsymbol{r}^A,\omega) \right) \right] dS
$$
$$
+ \int_{\partial\mathbb{D}} \mathbf{n} \cdot 2\beta^2 \left[\hat{\dot{\boldsymbol{\Omega}}}(\boldsymbol{r},\boldsymbol{r}^A,\omega) \times \hat{\boldsymbol{G}}^*_{\boldsymbol{v}^s,n}(\boldsymbol{r},\boldsymbol{r}^B,\omega) - \hat{\boldsymbol{G}}^*_{\dot{\boldsymbol{\Omega}},n}(\boldsymbol{r},\boldsymbol{r}^B,\omega) \times \hat{\boldsymbol{v}}^s(\boldsymbol{r},\boldsymbol{r}^A,\omega) \right] dS,
$$

$$(4.28)$$

where the left-hand side is again obtained using equation 4.10 and the definition of the delta function, identical to the derivation of equation 4.11.

It worth emphasizing that all derivations above are only suitable for a homogeneous, isotropic medium. For an inhomogeneous medium, P- and S-wave force potentials should be invoked for P-/S-wavefield separation at the source. Details can be found in Wapenaar and Haime (1990).

Chapter 5

Real-time microseismic event localization based on fast time-reversal extrapolation

Traditional time-reversal extrapolation is a promising technique for microseismic event localization. However, the technique is based on solving discrete two-way wave equations using the finite difference or finite element method, which makes it very time-consuming and not suitable for real-time applications. The generated wavefields have information redundancy such that only a small amount of information is enough to represent the whole extrapolation process. Proper orthogonal decomposition is used to remove information redundancy and create a much smaller extrapolation system, from which real-time microseismic event localization is possible. In this paper, we create a new extrapolation system by applying proper orthogonal decomposition to the first-order two-way elastic wave equations. The new extrapolation system is used to build a continuous waveform based microseismic event localization scheme that can rapidly locate multiple seismic events and determine their origin time.

5.1 Introduction

Event localization is one of the most important tasks for microseismic monitoring, including locating earthquakes in global seismology (Fehler, 2008) and microseismicity in hydraulic fracturing treatment (Van der Baan et al., 2013, Li and Van der Baan, 2016). Time-reversal extrapolation is a promising event localization technique using full waveform information (McMechan, 1985, Artman et al., 2010), which can also be called backward wavefield extrapolation. In traditional time-reversal extrapolation, receivers are treated as sources and the three-component wavefields are time-reversed and directly propagated toward its source location using a two-way elastic wave modeling operator and a known velocity model (McMechan, 1983). This method could be more accurate compared to traditional travel-time based methods since no picking of P- and S-wave first arrivals is required. Location results may be badly affected by mispicking and inaccurate picks (Castellanos and Van der Baan, 2015, Li and Van der Baan, 2016). Li and Van der Baan (2016) introduce an improved time-reversal extrapolation scheme, in which both particle velocity and pressure are extrapolated separately followed by their combination according to the acoustic representation theorem. For the purpose of computational efficiency, the same type of data can be extrapolated simultaneously. However, these methods are still both impractical for application in continuous real-time monitoring because solving a very large simulation system composed of several spatially discretized elastic wave equations is computationally intensive.

Pereyra and Kaelin (2008) first propose a fast acoustic wavefield propagation simulation procedure by constructing an order-reduced modeling operator using a technique called proper orthogonal decomposition (POD), which provides a possible solution to the issue of high computational cost mentioned above. Essentially, they speed up simulation by projecting the spatially discretized wave equations from a higher dimensional system to a much lower dimensional system, still keeping sufficient accuracy (Pereyra and Kaelin, 2008).

POD is a promising technique aimed at reducing the complexity of a numerical simulation system using mathematical insights, which has been widely applied in many dynamic system simulations in a common form as shown in Chatterjee (2000) and Schilders (2008). Applications include modeling of fluid flow,

real-time control, heat conduction (Lucia et al., 2004), wavefield propagation (Pereyra and Kaelin, 2008, Wu et al., 2013), aircraft design (Lieu et al., 2006), arterial simulations (Lassila et al., 2013) and nuclear reactor core design (Sartori et al., 2014), etc. POD is based on the observation that simulations with a high computational load often repeatedly solve the same problem (Benner et al., 2015). For instance, in the case of time-reversal extrapolation for microseismic event localization, the continuously recorded data are back-propagated through an unchanging velocity model. Thus the wave propagation 'engine' does not change, only the recorded data vary. Also, informational redundancy exists in most of the traditional simulation processes (Schilders, 2008), which means the discretized wave equations can be represented as a large but sparse matrix which can be compressed into a small but denser system that is much faster to solve.

In this paper, we introduce an adaptive randomized QR decomposition (ARQRd) (Halko et al., 2010) based POD procedure, balancing accuracy and computational efficiency. Similar techniques, such as randomized SVD and randomized QR, have been applied as rapid rank approximation methods for geophysical purposes (Gao et al., 2011, Oropeza and Sacchi, 2011, Cheng and Sacchi, 2015), especially when dealing with large datasets. The basic idea is to project the original data in a high-dimensional space to a low-dimensional data space using randomly selected vectors. However, the dimension of the new space is usually unknown (Halko et al., 2010) and sometimes needs to be pre-tested before the new matrix can capture the demanded amount of features in the original data. In our case, ARQRd can automatically provide the new projected data which not only have the minimum dimension but also capture the most amount of information without the needs of pretesting.

We then build a reduced-order two-way elastic wave modeling system that can be used for time-reversal extrapolation using the proposed POD process. We also propose a POD-based energy flux based focusing criterion firstly proposed by Li and Van der Baan (2017) to fit in the low-order modeling scheme. The new wavefield extrapolation approach is more computationally efficient which makes real-time automatic seismic event localization possible. Finally, we compare the ARQRd results with the results from traditional time-reversal

extrapolation in the example section.

5.2 General Theory

POD generally has two steps, namely an off-line training part where the smaller simulation system is learned and created, and an on-line calculation where the data are repeatedly generated with little cost and high accuracy. We briefly introduce the two parts in the following content respectively.

5.2.1 Off-line training

Off-line training is the key aspect of POD which includes the following steps:

(1) Compute training data and construct a snapshot matrix, which is formed from high-fidelity simulations. A high-fidelity simulation is calculated by numerically solving a group of spatially discretized partial differential equations (PDEs), given by

$$\frac{\partial \boldsymbol{u}(t)}{\partial t} = \boldsymbol{L}\boldsymbol{u}(t) + \boldsymbol{f}(t), \tag{5.1}$$

where $\boldsymbol{u}$ is a time dependent state variable, which is spatially discrete but continuous in time; $\boldsymbol{L}$ is a matrix of partial differential operators, $\boldsymbol{f}$ is a time dependent source term, the total discretized simulation time is N_T. Equation 5.1 is a general form of discretized PDEs that is applicable in 1D, 2D or 3D wave simulations. Finite difference or finite element methods are the two most common methods to solve equation 5.1. Since equation 5.1 represents a time-varying system, a snapshot means one time slice of a high-fidelity simulation of the system. A series of snapshots extracted during the full simulation are put into snapshot matrix $\boldsymbol{A}_{\boldsymbol{s_i}}$ in chronological order, given by

$$\boldsymbol{A}_{\boldsymbol{s_i}} = [\boldsymbol{u}_1^i, \boldsymbol{u}_2^i, \boldsymbol{u}_3^i, ..., \boldsymbol{u}_{N_t}^i], \tag{5.2}$$

where s_i means the ith simulation; each column $\boldsymbol{u}_t^i$ corresponds to a vectorized snapshot at time t and the subscript index N_t is the total number of time slices used for training, where $N_t \leqslant N_T$ and the sampling time interval between any

two adjacent slices has to satisfy the Nyquist sampling theorem. For multiple simulations, an even larger snapshot matrix $\boldsymbol{A}$ is constructed comprising multiple snapshot matrices, given by

$$\boldsymbol{A} = [\boldsymbol{A_{s_1}}, \boldsymbol{A_{s_2}}, \boldsymbol{A_{s_3}}, ..., \boldsymbol{A_{s_n}}], \tag{5.3}$$

where n is the number of simulations. Each simulation $\boldsymbol{s_i}$ can represent different aspects, for instance, different source positions or different source radiation patterns.

(2) Compute and compress a left orthogonal basis of snapshot matrix $\boldsymbol{A}$. The basic assumption of POD is that matrix $\boldsymbol{A}$ can be approximated by a new matrix $\boldsymbol{Q}$ whose rank is much lower than the size of either dimension of matrix $\boldsymbol{A}$, while still keeping most of the key information of $\boldsymbol{A}$, denoted by

$$Rank(\boldsymbol{Q}) << Minimum(m, n), \tag{5.4}$$

where m and n are the row and column numbers of snapshot matrix $\boldsymbol{A}$ respectively. The selection of $\boldsymbol{Q}$ is non-unique. In this paper, we define $\boldsymbol{Q}$ as an orthonormal basis such that each column of the matrix $\boldsymbol{A}$ can be expressed by a combination of columns in $\boldsymbol{Q}$ with sufficient accuracy. Since $\boldsymbol{Q}$ is an orthonormal matrix, it also satisfies the condition

$$\boldsymbol{Q}^T\boldsymbol{Q} = \boldsymbol{I}, \tag{5.5}$$

where $\boldsymbol{I}$ is an identity matrix (Strang, 2006).

Singular value decomposition (SVD) or QR decomposition (QRd) are the two most commonly used methods to compute the left orthonormal basis $\boldsymbol{Q}$ and the singular values of the snapshot matrix $\boldsymbol{A}$. The approximated rank $R_{\boldsymbol{A}}$ is determined by choosing the largest singular values and the corresponding columns are grouped into $\boldsymbol{Q}$ which is only a small portion of the full left orthonormal basis, as long as the selected basis $\boldsymbol{Q}$ is enough to span the column space of the snapshots matrix $\boldsymbol{A}$, mathematically satisfying the evaluation criterion

$$||\boldsymbol{A} - \boldsymbol{Q}\boldsymbol{Q}^T\boldsymbol{A}|| \leq \epsilon \tag{5.6}$$

where $|| \cdot ||$ denotes the l_2 norm and ϵ is a positive error tolerance (Halko et al., 2010). We call the selected basis $\boldsymbol{Q}$ the reduced orthonormal column basis.

We use ARQRd to calculate the left orthonormal basis $\boldsymbol{Q}$. It can be seen as a randomized Gram-Schmidt method embedded with the evaluation criterion (equation 5.6), where the reduced orthonormal column basis $\boldsymbol{Q}$ of the snapshot matrix $\boldsymbol{A}$ is calculated in an iterative scheme (Halko et al., 2010).

In the ith iteration, a new column vector $\boldsymbol{c}_i$ is first calculated through a projection of snapshot matrix $\boldsymbol{A}$ using

$$\boldsymbol{c}_i = \boldsymbol{A}\boldsymbol{\omega}_i, \tag{5.7}$$

where $\boldsymbol{\omega}_i$ is a random column vector with a Gaussian distribution. Then $\boldsymbol{c}_i$ is orthonormalized to all previously generated $i - 1$ columns using the Gram-Schmidt method before it is added to the desired basis $\boldsymbol{Q}$. Equation 5.6 is evaluated in each iteration so that the calculated basis $\boldsymbol{Q}$ has a minimum number of columns satisfying the evaluation criterion with a given error tolerance ϵ, when iteration stops. This makes ARQRd more computationally efficient than traditional randomized QR or SVD (Halko et al., 2010).

(3) Construct a new reduced simulation system. The new reduced system approximates the full system (5.1), as long as the source positions are unchanged. The source waveforms can be different but must have an overlapping frequency content. The state variable $\mathbf{u}(t)$ can then be expressed as a linear combination of the reduced orthonormal column basis $\boldsymbol{Q}$, using

$$\mathbf{u}(t) = \boldsymbol{Q}\boldsymbol{a}(t), \tag{5.8}$$

where $\boldsymbol{a}(t)$ is a coefficient vector at time t. Note equation 5.8 is the key assumption that makes this method successful. Equation 5.8 is substituted into equation 5.1 giving

$$\frac{\partial \boldsymbol{Q}\boldsymbol{a}(t)}{\partial t} = \boldsymbol{L}\boldsymbol{Q}\boldsymbol{a}(t) + \mathbf{f}(t). \tag{5.9}$$

Given that matrix $\boldsymbol{Q}$ is time independent, we can further rephrase the equation

by multiplying its both sides with $\boldsymbol{Q}^T$, rendering

$$\frac{\partial \boldsymbol{a}(t)}{\partial t} = \boldsymbol{Q}^T \boldsymbol{L} \boldsymbol{Q} \boldsymbol{a}(t) + \boldsymbol{Q}^T \mathbf{f}(t), \tag{5.10}$$

where $\boldsymbol{Q}^T \boldsymbol{L} \boldsymbol{Q}$ is a reduced-order partial differential operator matrix of size $[N_Q, N_Q]$; $\boldsymbol{Q}^T \mathbf{f}(t)$ a reduced-order source term. We can see from equation 5.4 that the dimensions of the new simulation system is much smaller than the original one (equation 5.1), which ensures the repeated simulations can be done on-the-fly.

5.2.2 On-line simulation

Equation 5.10 is solved on-the-fly using a finite difference method, where both spatial and temporal axes are discretized, given by

$$\boldsymbol{a}_{i+1} - \boldsymbol{a}_{i-1} = \mathbb{L} \boldsymbol{a}_i + \mathbb{Q}^T \mathbf{f}_i, \tag{5.11}$$

where $\mathbb{L}$ is the reduced finite difference operator $\boldsymbol{Q}^T \boldsymbol{L} \boldsymbol{Q}$ scaled by dt; $\boldsymbol{a}_{i+1}$, $\boldsymbol{a}_i$ and $\boldsymbol{a}_{i-1}$ are coefficient vectors at discrete time point $i+1$, i and $i-1$; $\mathbb{Q}$ is the basis matrix scaled by dt.

At each time iteration, the coefficient vector $\mathbf{a}$ is updated using equation 5.11 and saved for wavefield construction. Then, any snapshot $\boldsymbol{u}_i$ at time point i can be reconstructed using equation 5.8.

5.3 Reduced-order time-reversal extrapolation

In this section, we start with the 2D stress-velocity two-way elastic wave equations, given by

$$\frac{\partial v_x(t)}{\partial t} = \frac{1}{\rho}\frac{\partial \tau_{xx}(t)}{\partial x} + \frac{1}{\rho}\frac{\partial \tau_{xz}(t)}{\partial z} + f_{v_x}(t)$$

$$\frac{\partial v_z(t)}{\partial t} = \frac{1}{\rho}\frac{\partial \tau_{xz}(t)}{\partial x} + \frac{1}{\rho}\frac{\partial \tau_{zz}(t)}{\partial z} + f_{v_z}(t)$$

$$\frac{\partial \tau_{xx}(t)}{\partial t} = (\lambda + 2\mu)\frac{\partial v_x(t)}{\partial x} + \lambda\frac{\partial v_z(t)}{\partial z} + f_p(t) \qquad (5.12)$$

$$\frac{\partial \tau_{zz}(t)}{\partial t} = (\lambda + 2\mu)\frac{\partial v_z(t)}{\partial z} + \lambda\frac{\partial v_x(t)}{\partial x} + f_p(t)$$

$$\frac{\partial \tau_{xz(t)}}{\partial t} = \mu(\frac{\partial v_x(t)}{\partial z} + \frac{\partial v_z(t)}{\partial x}),$$

where τ_{xx} and τ_{zz} are the x and z components of the normal stress fields; τ_{xz} is the shear stress field; v_x and v_z are the horizontal and vertical components of particle velocity fields; f_{v_x} and f_{v_z} are single forces and f_p is an external pressure source.

We write equation 5.12 into the matrix form of equation 5.1 by assigning that

$$\boldsymbol{u} = \begin{pmatrix} \boldsymbol{v}_x \\ \boldsymbol{v}_z \\ \boldsymbol{\tau}_{xx} \\ \boldsymbol{\tau}_{zz} \\ \boldsymbol{\tau}_{xz} \end{pmatrix}, \boldsymbol{L} = \begin{pmatrix} \boldsymbol{0} & \boldsymbol{0} & \frac{1}{\rho}\boldsymbol{L}_x & \boldsymbol{0} & \frac{1}{\rho}\boldsymbol{L}_z \\ \boldsymbol{0} & \boldsymbol{0} & \boldsymbol{0} & \frac{1}{\rho}\boldsymbol{L}_z & \frac{1}{\rho}\boldsymbol{L}_x \\ (\lambda+2\mu)\boldsymbol{L}_x & \lambda\boldsymbol{L}_z & \boldsymbol{0} & \boldsymbol{0} & \boldsymbol{0} \\ \lambda\boldsymbol{L}_x & (\lambda+2\mu)\boldsymbol{L}_z & \boldsymbol{0} & \boldsymbol{0} & \boldsymbol{0} \\ \mu\boldsymbol{L}_z & \mu\boldsymbol{L}_x & \boldsymbol{0} & \boldsymbol{0} & \boldsymbol{0} \end{pmatrix}, \boldsymbol{f} = \begin{pmatrix} \boldsymbol{f}_{v_x} \\ \boldsymbol{f}_{v_z} \\ \boldsymbol{f}_p \\ \boldsymbol{f}_p \\ \boldsymbol{0} \end{pmatrix},$$

$$(5.13)$$

where $\boldsymbol{L}_x$, $\boldsymbol{L}_y$ and $\boldsymbol{L}_z$ represent the matrix form of the spatial derivatives $\frac{\partial}{\partial x}$, $\frac{\partial}{\partial y}$ and $\frac{\partial}{\partial z}$; $\boldsymbol{u}$ and $\boldsymbol{f}$ are the vectorized wavefields and source term respectively.

A staggered grid finite difference method is used to discretize the 2D model, where wavefield variables $\boldsymbol{v}_x$, $\boldsymbol{v}_z$, $\boldsymbol{\tau}_{xx}$, $\boldsymbol{\tau}_{zz}$ and $\boldsymbol{\tau}_{xz}$ are assigned to the grid according to Figure 5.1 (Zeng and Liu, 2001), with the corresponding grid size $[N_z, N_x - 1]$, $[N_z - 1, N_x]$, $[N_z, N_x]$, $[N_z, N_x]$ and $[N_z - 1, N_x - 1]$. Since $\boldsymbol{u}$ is a vector composed of five vectorized wavefield variables, its length is the sum of their total grid numbers, denoted by N_m. Likewise, $\boldsymbol{L}$ is a sparse matrix with the size of $[N_m, N_m]$.
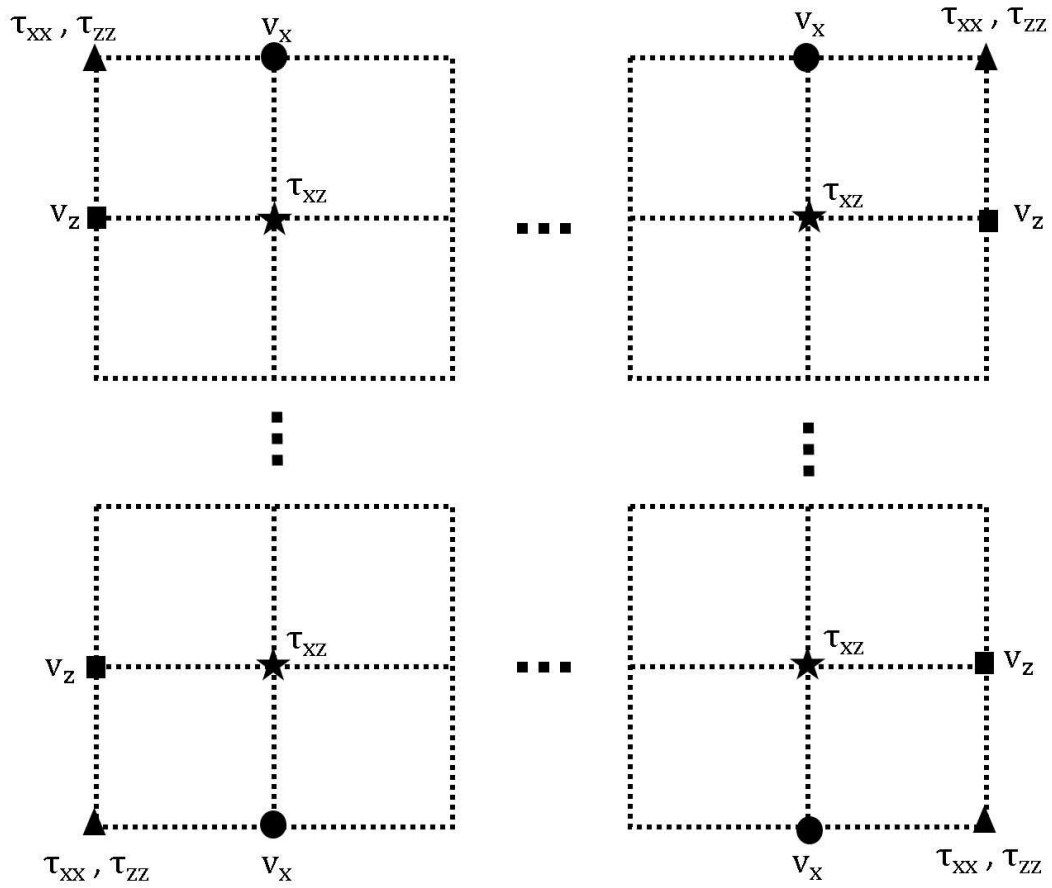
Figure 5.1: The relative locations of wavefields components in a staggered grid.

Next, we introduce a procedure to build a reduced-order system of two-way elastic wave equations for time reversal extrapolation. Though the derivation is in the 2D space for simplicity, it can be extended to the 3D space without difficulty. Moreover, two assumptions are needed for this derivation, namely (1) receiver locations and approximated velocity model are known; (2) the same finite differential operator is used in both forward and time-reversal extrapolations.

The idea of traditional time-reversal extrapolation is basically the same as wave propagation simulation using equation 5.12. The only difference is that the source term $\boldsymbol{f}_{v_x}$ and $\boldsymbol{f}_{v_z}$ in equations 5.1 and 5.13 are replaced with the time-reversed x- and z-component of particle velocity recordings, which means in this method receivers are turned into sources from where recordings are injected into the medium (McMechan, 1983).

5.3.1   Offline Training

According to the previous description, the size of the snapshot matrix $\boldsymbol{A}$ is directly determined by the number of receivers. For generality, we assume there are N_s receivers located at coordinates $[x_1, z_1]$, $[x_2, z_2]$, ..., $[x_{N_s}, z_{N_s}]$ for microseismic monitoring, where x and z are horizontal position and depth respectively. Since in 2D reverse-time extrapolation, there are horizontal and vertical components of recordings to be extrapolated, simulations from sources with a single component, horizontal and vertical, are both needed to generate both P- and S-wavefields, and all of these are included in one snapshot matrix $\boldsymbol{A}$ for training (Equation 5.3). The snapshot matrix for a jth horizontal single-force source s_j located at $[x_j, z_j]$ is

$$\boldsymbol{U}^x_{s_j} = [\boldsymbol{u}^x_1, \boldsymbol{u}^x_2, ...\boldsymbol{u}^x_{N_t}], \tag{5.14}$$

where superscript x refers to the horizontal direction of a single-force source; $N_t \leqslant N_T$, where N_T is discrete total simulation time. A similar expression holds for $\boldsymbol{U}^z$ where superscript z denotes vertical direction. Then the complete snapshot matrix for training is grouped as

$$\boldsymbol{A} = [\boldsymbol{U}_{s_1}^x, \boldsymbol{U}_{s_2}^x, ...\boldsymbol{U}_{s_{N_s}}^x, \boldsymbol{U}_{s_1}^z, \boldsymbol{U}_{s_2}^z, ...\boldsymbol{U}_{s_{N_s}}^z] \tag{5.15}$$

Then we apply ARQRd to the snapshot matrix $\boldsymbol{A}$ to get a basis $\boldsymbol{Q}$ with the grid size of $[N_m, N_Q]$ following the step (2) in the last section. Likewise, we construct a reduced-order partial differential operator $\boldsymbol{Q}^T \boldsymbol{L} \boldsymbol{Q}$, which can be used in time-reversal extrapolation for real-time microseismic localization. The size of the new partial differential operator is $[N_Q, N_Q]$. Since $N_Q << N_m$, we have a reduced-order extrapolation system whose size is much smaller than the original one.

Based on the previous derivation, the reduced-order time-reversal extrapolation system can be built by first replacing the source term $\boldsymbol{f}$ in equation 5.13 with the time-reversed horizontal and vertical components of particle velocity recordings $\boldsymbol{R}_x^{tr}$ and $\boldsymbol{R}_z^{tr}$ respectively, given by

$$\boldsymbol{D}^{tr} = \begin{pmatrix} \boldsymbol{R}_x^{tr} \\ \boldsymbol{R}_z^{tr} \\ \boldsymbol{0} \\ \boldsymbol{0} \\ \boldsymbol{0} \end{pmatrix}, \tag{5.16}$$

where the total temporal sampling number of recordings is N_D. Equation 5.1 becomes

$$\frac{\partial \boldsymbol{u}^{tr}}{\partial t} = \boldsymbol{L} \boldsymbol{u}^{tr} + \boldsymbol{D}^{tr}, \tag{5.17}$$

where $\boldsymbol{u}^{tr}$ are the time-reversed wavefields, denoted by

$$\boldsymbol{u}^{tr} = \begin{pmatrix} \boldsymbol{v}_x^{tr} \\ \boldsymbol{v}_z^{tr} \\ \boldsymbol{\tau}_{xx}^{tr} \\ \boldsymbol{\tau}_{zz}^{tr} \\ \boldsymbol{\tau}_{xz}^{tr} \end{pmatrix}, \tag{5.18}$$

Analogous to the derivation of equation 5.10, equation 5.17 is written into

a reduced-order form

$$\frac{\partial \boldsymbol{a}^{tr}(t)}{\partial t} = \boldsymbol{Q}^T \boldsymbol{L} \boldsymbol{Q} \boldsymbol{a}^{tr}(t) + \boldsymbol{Q}^T \boldsymbol{D}^{tr}, \qquad (5.19)$$

where $\boldsymbol{a}^{tr}(t)$ is the coefficient vector at time t for time-reversal extrapolation; $\boldsymbol{Q}^T \boldsymbol{D^{tr}}$ are the reduced-order recordings as a source term. Equation 5.19 is the reduced-order equation for time-reversal extrapolation.

5.3.2 Continuous online time-reversal extrapolation

With the previously derived reduced-order system, we now introduce the implementation of continuous online time-reversal extrapolation. In this step, since the total discrete simulation time in the offline training step is N_T, which is likely substantially less than the total sampling number of recordings N_D, a discrete temporal window of length N_T is used to select the reduced-order recording segments for extrapolation, using equation 5.11 and 5.19.

Then similar to equation 8, an equation

$$\boldsymbol{U}^{tr} = \boldsymbol{Q} \boldsymbol{a}^{tr} \qquad (5.20)$$

is used to reconstruct the complete time-reversed wavefields, where the structure of the basis $\boldsymbol{Q}$ is

$$\boldsymbol{Q} = \begin{pmatrix} \boldsymbol{Q}_{\boldsymbol{v}_x} \\ \boldsymbol{Q}_{\boldsymbol{v}_z} \\ \boldsymbol{Q}_{\boldsymbol{\tau}_{xx}} \\ \boldsymbol{Q}_{\boldsymbol{\tau}_{zz}} \\ \boldsymbol{Q}_{\boldsymbol{\tau}_{xz}} \end{pmatrix} \qquad (5.21)$$

However, sometimes it is only necessary to reconstruct the wavefields within a target area (Figure 5.2), which means only the portion of the basis corresponding to the area is used in wavefield reconstruction, leading to

$$\boldsymbol{u}^{tr} = \boldsymbol{Q}_{new} \boldsymbol{a}^{tr}, \qquad (5.22)$$

where $\boldsymbol{Q}_{new}$ represents the portion of basis $\boldsymbol{Q}$ we used for reconstruction.

116
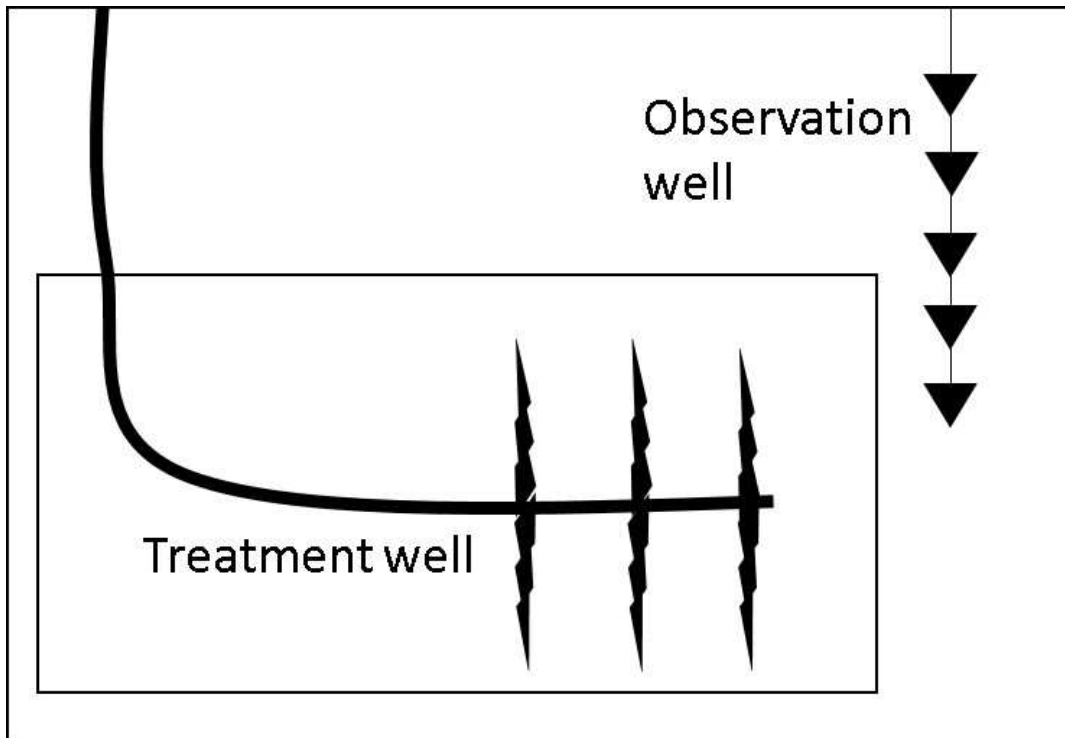
Figure 5.2: Geological settings for microseismic monitoring. Triangles: receivers in a borehole. Three hydraulic fracturing stages are at the end of a treatment well. Outer box: the model used for training. Inner box: target area in which wavefields are reconstructed.

This describes the procedure of reduced-order extrapolation for a single segment of data, whereas for continuous extrapolation, a parameter $N_{T_{step}}$ is used to move the temporal window of time-reversed data D^{tr} to the next segment, followed by the same extrapolation process.

During back-propagation, a source focusing criterion is needed due to the absence of the zero-lag cross-correlation imaging condition which is normally applied in time-reverse extrapolation based source localization methods (Artman et al., 2010). An energy flux based focusing criterion can be applied to each time slice of the back-propagated source image to automatically determine the source location based on the Hough transform. Full details can be found in Li and Van der Baan (2017).

5.4   Example

In this section, we apply the proposed reduced-order system to two examples, namely wavefield extrapolation and continuous microseismic event localization. Both examples use the Marmousi velocity model (Figure 5.3), which is based on a profile through the North Quenguela trough in the Cuanza basin (Mora, 2002). The model is 2928m in depth and 9216m in length. The discrete velocity model we used in this section has grid numbers of 122 in depth and 384 in length, with a grid spacing of 24m and time interval of 1.8ms. The size of the finite differential operator ($\mathbb{L}$ in equation 5.11) for the high-fidelity simulation is [233229, 233229], where 233229 is the number of rows of $\boldsymbol{u}$ in equation 5.13.

In both examples, the high-fidelity simulations are conducted by solving the traditional two-way wave equations using a staggered-grid finite difference method, in which a fourth-order spatial and a second-order temporal finite difference operator are applied.

5.4.1   Reduced-order Wavefield Extrapolation

This example is used to illustrate that input source time functions used for the on-line simulation can be different from the one used for off-line training step. For simplicity, we use only one source denoted by the second star from the top
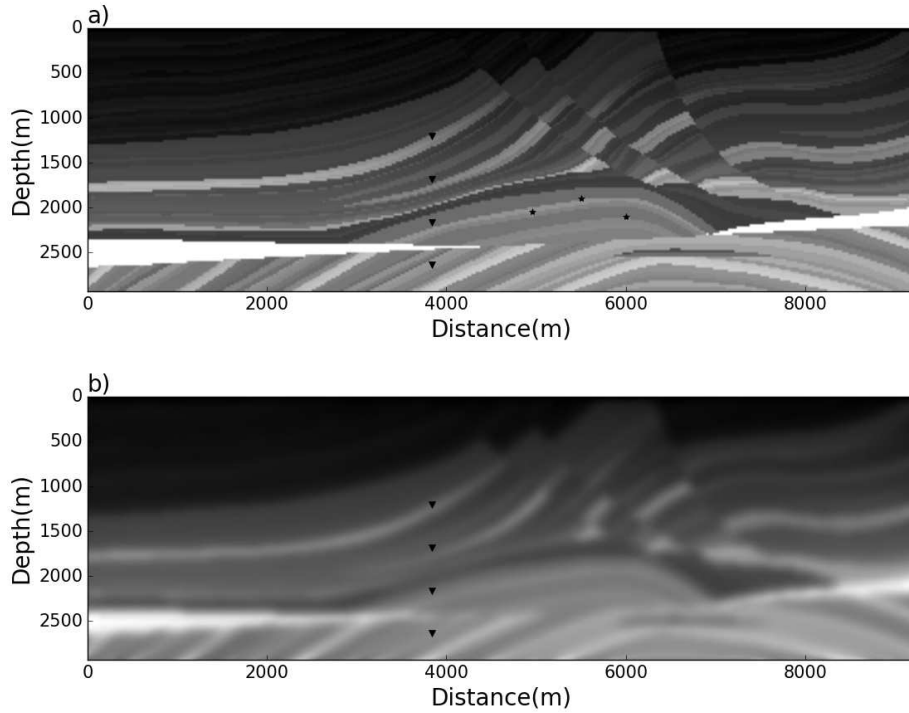
Figure 5.3: a) Marmousi velocity model for microseismic monitoring simulation. Stars: microseismic events. b) Smoothed Marmousi velocity model for time-reversal extrapolation. Triangles: receivers in a borehole.

in Figure 5.3a and the smoothed Marmousi velocity model (Figure 5.3b).

In the off-line training step, an explosive source with a Ricker wavelet with a peak frequency of 10Hz is used, which originates at 0.01s (Figure 5.4a). The source locates on the right of the well with coordinates (x, z) of (1900, 5500). The total simulation time is 1.5s, with a temporal interval of 1.8ms. We save every snapshot of both particle velocity and stress wavefields obtained from the high-fidelity simulation to a snapshot matrix $\boldsymbol{A}$ according to equation 5.13 and 5.15. The size of $\boldsymbol{A}$ is [233229, 834], where 834 is the total number of discrete times N_t.

In order to illustrate the information redundancy of matrix $\boldsymbol{A}$, we display the singular values of $\boldsymbol{A}$ in Figure 5.5, obtained by applying SVD to $\boldsymbol{A}$. Figure 5.5 shows a sharp drop in the singular values, showing information redundancy exists in the traditional simulation process. We then apply ARQRd to auto-

119
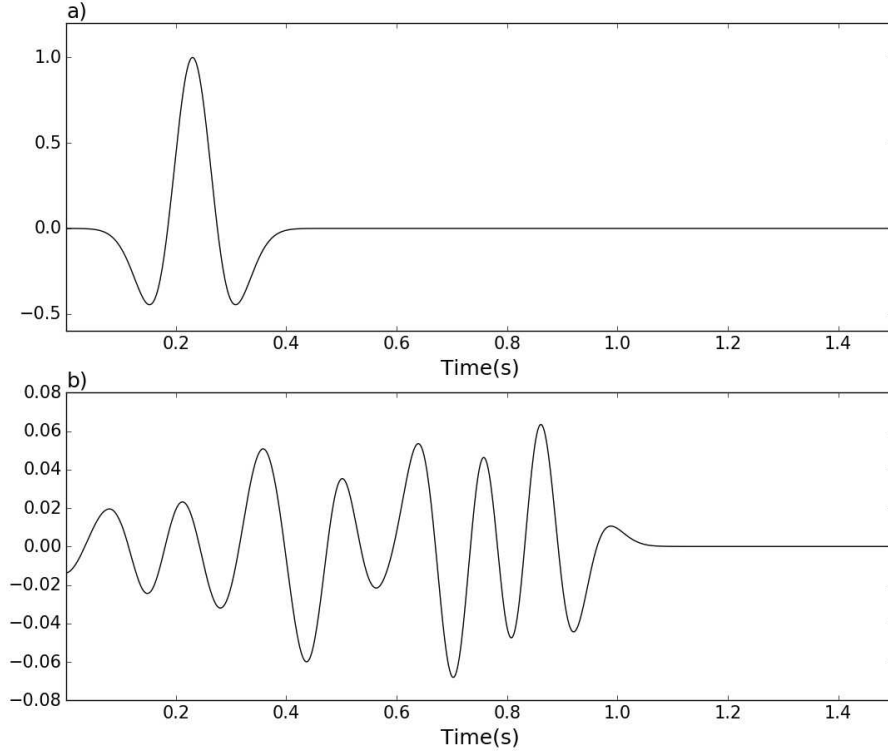
Figure 5.4: Source time functions a) used for off-line training. b) used for on-line simulation

matically calculate basis Q of the snapshot matrix A, where the value of ϵ is 10^{-6}. The size of the basis Q is [233229, 216]. The reduced-order extrapolation system is constructed according to equation 5.10, in which the size of the reduced-order partial differential operator is [216, 216]. The size of the new system is about 2×10^{-5} times of that of the original extrapolation system.

In the online simulation step, a new source time function (Figure 5.4b) is applied as force $\boldsymbol{f}(t)$ in equation 5.10, using the reduced-order matrix Q as obtained from the simpler source, as shown in Figure 5.4a. Wavefields are calculated using equations 5.8 and 5.10. As a comparison, we also calculate the wavefields from the new source time function (Figure 5.4b) using the high-fidelity simulation. The resulting wavefields from the two simulation systems are shown in Figure 5.6.

The pressure wavefields in Figure 5.6 at 0.71s and 0.99s are calculated us-
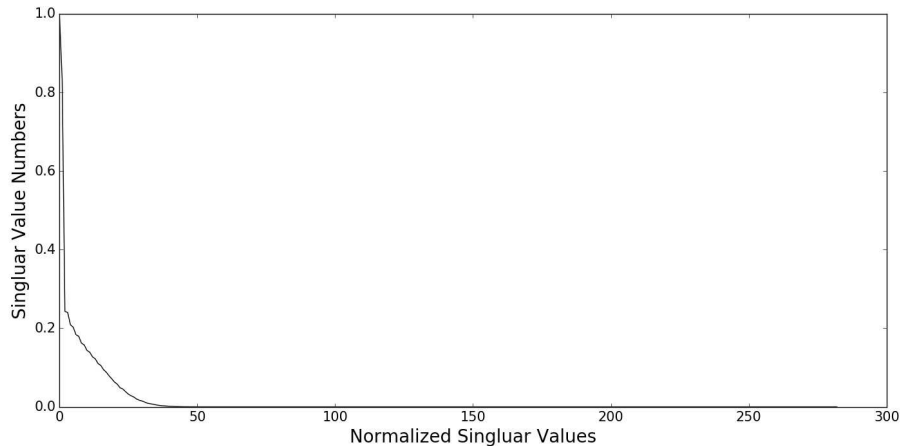
Figure 5.5: Singular value plot of the snapshot matrix $\boldsymbol{A}$.

ing the reduced-order (Figure 5.6a and 5.6b) and the high-fidelity simulations (Figure 5.6c and d). Figures 5.6e and 5.6f show that the average differences between the pressure wavefields constructed by the two simulation schemes deviate less than 0.1% of the largest negative amplitudes. Figure 5.7 shows a trace extracted from an arbitrary spatial location to compare the simulated waveforms in detail. The waveforms of pressure and x- and z-component of particle velocities from two simulation schemes overlap each other perfectly. The above results show that the reduced-order simulation is insensitive to changing source time functions in the on-line simulation step as long as the frequency contents overlap and the source position remains fixed. Wavefields derived from the reduced-order simulation are near-identical to the ones obtained from the high-fidelity simulation.

We then compare the computational costs of 1.5s of both high-fidelity and reduced-order simulations, where the latter includes the costs of the offline training, online calculation of coefficients and wavefield construction, displayed in Table 5.1. For a fair comparison, we calculate the complete wavefields including two-component particle velocities and normal and shear stresses in both cases. The total computation time for the reduced-order simulation is 575.73s, which is much longer than the cost of the high-fidelity simulation, 190s. However, approximately 99% of computation costs are due to offline training in order to obtain an order-reduced simulation system whereas the calculation
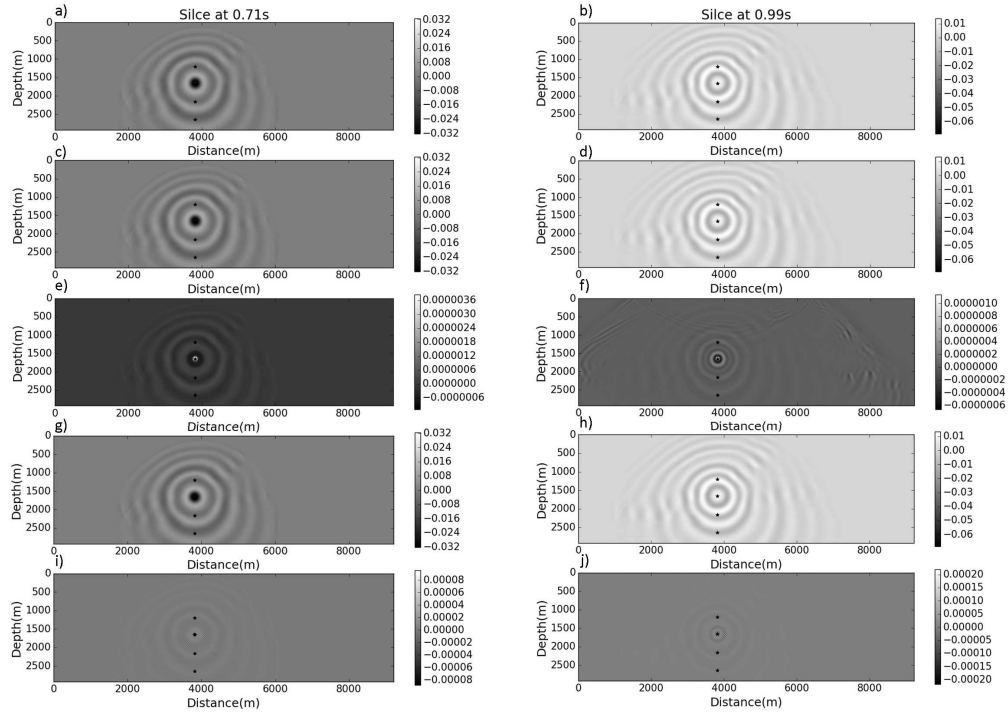
Figure 5.6: Left and right panel: Snapshots at 0.71s and 0.99s respectively from the source waveform in Figure 5.4b. a) and b): Pressure wavefields constructed by reduced-order simulation derived from a snapshot matrix $\boldsymbol{A}$ including all the time snapshots. c) and d): Pressure wavefields constructed by high-fidelity simulation. e): Difference between a) and c). f): Difference between b) and d). The max errors on the all snapshots are less than 0.03%. g) and h): Pressure wavefields constructed by reduced-order simulation. In this case only one third of the snapshots are selected to build the snapshot matrix $\boldsymbol{A}$. i): Difference between a) and g). j): Difference between b) and h). The max errors on the all snapshots are less than 2%.

122
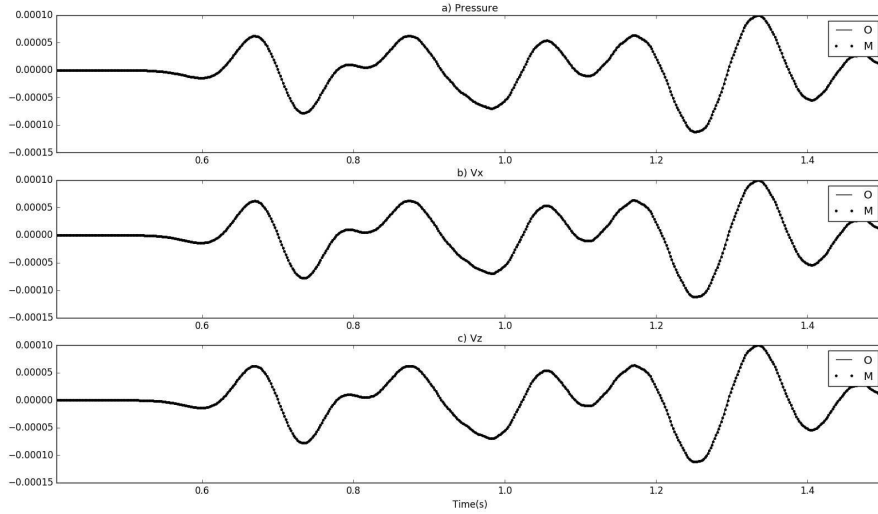
Figure 5.7: Comparison of the waveforms calculated by reduced-order and high-fidelity simulations, denoted by stars and triangles respectively. a) pressure. b) and c) x and z-components of particle velocity. They overlap with max 0.03% difference.

cost of coefficients only takes 0.04‰of the total computational cost. These results indicate suitability of time-reversal extrapolation for continuous microseismic event localization, since we only need to do the offline training once using a limited total simulation duration whose computational cost is fixed and then it can be used repeatedly to extrapolate various recordings with extremely fast speed, which eventually takes less computational time than high-fidelity simulations for longer recording time.

Also the offline training can further be sped up by reducing the number of time snapshots in matrix $\boldsymbol{A}$, equation 5.2 and 5.3 at the expense of less accurate reconstructions. For instance by including only one out of every three consecutive snapshots in time we obtain a much smaller snapshot matrix $\boldsymbol{A}$. The offline training time becomes 480s instead of 575.73s and the maximum reconstruction errors are less than 2% (Figures 5.6i and 5.6j)for the same test setup. This is permissible as long as the down-sampled snapshots matrix still actually reflects the frequency content of the complete data.

123

Table 5.1: Computation costs of 1.5s high-fidelity and reduced-order simulations

high-fidelity	Total cost	190 s
	Offline training	574 s
Reduced order	Online calculation of coefficients	0.03 s
	Wavefield construction	1.7 s

5.4.2   Continuous microseismic event localization

We simulate a microseismic monitoring setup in this example, as shown in Figure 5.3a. In the model, a vertical borehole is simulated with four receivers at depths approximately from 1000m to 2900m to record acoustic emissions from three double-couple sources. Particle velocities in the x and z direction are measured at each receiver, with a total recording time of 9s (Figure 5.8).

Figure 5.3b shows a smoothed Marmousi velocity model used for off-line training and wavefield extrapolation. The model has the same discrete size as the non-smoothed model. The smoothed velocity model is used to mimic the usual case in which a true velocity model is often not available and also to prevent secondary reflections.

Since x and z-component recordings of four receivers are to be extrapolated, eight sources corresponding to each component of the four receivers are used for simulations in the off-line training step. They are all single force sources, four in the x direction and four in the z direction and all have a simulation time of 2s. Ricker wavelets with peak frequencies of 10Hz are used in the offline training. The wavefields corresponding to the eight sources are calculated separately. To reduce memory issues in the ARQRd procedure, we only save every other snapshot in time obtained from each simulation to $\boldsymbol{A}$ using the ordering shown in equation 5.15. After applying ARQRd to matrix $\boldsymbol{A}$, a basis $\boldsymbol{Q}$ is obtained including all information of the wavefields radiated from the eight sources. The size of basis $\boldsymbol{Q}$ is [233229, 779]. The size of the new system is about 10^{-5} times of that of the original extrapolation system, whereas if only counting the non-zero elements of equation 5.1, the size of the new system becomes 0.4 times that of the original extrapolation system.

In the on-line extrapolation step, data are first segmented with a 2s temporal window N_T, denoted by AB in Figure 5.8. The window is sliding along the
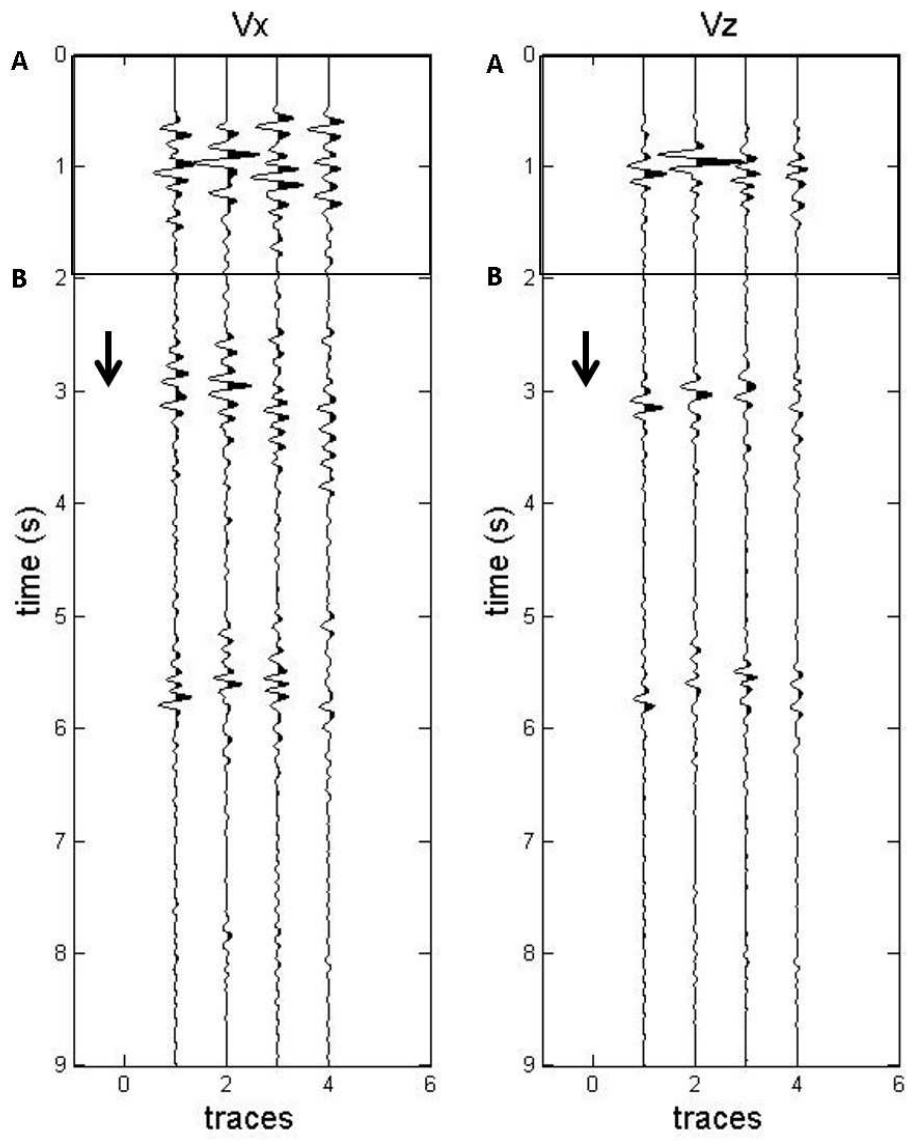
Figure 5.8: x (left panel) and z-component (right panel) recordings from simulated three microseismic events. Black box: temporal sliding window. Black arrow: temporal window sliding direction.

125

Table 5.2: Computation costs of continuous high-fidelity and reduced-order simulations

Continuous 9s recordings	high-fidelity	Total cost 1140 s	
14 overlapping 2s segments (total 9s)	high-fidelity	Total cost 3546 s	
14 overlapping 2s segments (total 9s)	Reduced order	Offline training	4146 s
		Online calculation of coefficients	0.36 s
		Wavefield construction	28 s

time axis in the direction of the black arrow in Figure 5.8, with a sliding step $N_{T_{step}}$ of 0.5s. We choose 0.5s simply to balance the number of events detected and total online extrapolation cost as for simplicity we assume there can be at most a single microseismic event in each data segment. So with the time window sliding along the recordings, the 9s data are divided into fourteen segments. Each segment is injected into the reduced system respectively to calculate coefficients $\boldsymbol{a}$. Full wavefields are reconstructed using equation 5.8. We only reconstruct wavefields within a predefined area denoted by the red boxes in Figure 5.9, assuming that microseismic events solely occur here. All maps in Figure 5.9 are absolute energy flux maps using the focusing criterion described in Li and Van der Baan (2017), for a better illustration.

We then compare the computation times in three scenarios listed in Table 5.2, namely 1) direct back-propagation of 9s recordings continuously using the high-fidelity simulation system; 2) direct back-propagation of fourteen 2s segments of recordings using the high-fidelity simulation system; 3) offline training and back-propagation of fourteen 2s segments of recordings using the reduced-order system. We can see that the time-reversal extrapolation based the reduced-order system of 9s recordings takes more total computational time than direct extrapolation using the high-fidelity simulation system. But the computational costs of calculation of coefficients and reconstruction increase much slower than that when using the high-fidelity system. We can expect a much smaller relative computational cost if much longer recordings are processed, for instance, minutes, hours, or even days of continuously recorded microseismic data.

126

Figures 5.9a, b and c display the three snapshots of normalized energy flux maps using the high-fidelity reconstructions for the three focusing maxima whose coordinates (x, z) are (2042,4950) (1898,5506) and (2100,6007) in meters. The locations of the maxima on each snapshot are almost the same as the locations of the three predefined sources (blue star in Figure 5.9), whose coordinates (x, z) are (2040,4960) (1900,5500) and (2100,6000) in meters. Those side lobes on the maps are due to the very limited number of receivers. The corresponding time of these three snapshots are 1.1s, 2.75s and 5.68s, which are close to the true origin times of 1.1s, 2.8s and 5.6s. We then compare the high-fidelity reconstructions with the ones obtained using the reduced-order systems (Figures 5.9 d, e and f) and find that the two results are essentially identical. This indicates that it is possible to do continuous microseismic monitoring using the reduced-order system real-time and obtain similar results as for the high-fidelity system but with substantially reduced online computation times.

5.5   Discussion

In this chapter, we show that proper orthogonal decomposition is a powerful tool to create a substantially reduced simulation system by removing redundant information which normally exists in traditional two-way wave equation based simulations. The reduced simulation system is significantly faster with good reconstruction quality. However, this comes at the cost of a computationally intensive offline training step, which could be even more expensive than direct high-fidelity simulations. Generally, the cost of offline training is determined by the calculations of snapshot matrix $\boldsymbol{A}$ and its left orthonormal basis $\boldsymbol{Q}$, where the size of $\boldsymbol{A}$ is directly determined by the numbers of both high-fidelity simulations corresponding to the included different sources and time slices selected from each simulation for training. A snapshot matrix $\boldsymbol{A}$ is called a complete snapshot matrix when it includes high-fidelity simulations with sources at every grid point within the model. Yet this may not be required for all applications. For instance, a sufficient snapshot matrix for time-reversal extrapolation only includes those simulations with source locations corresponding to receiver loca-
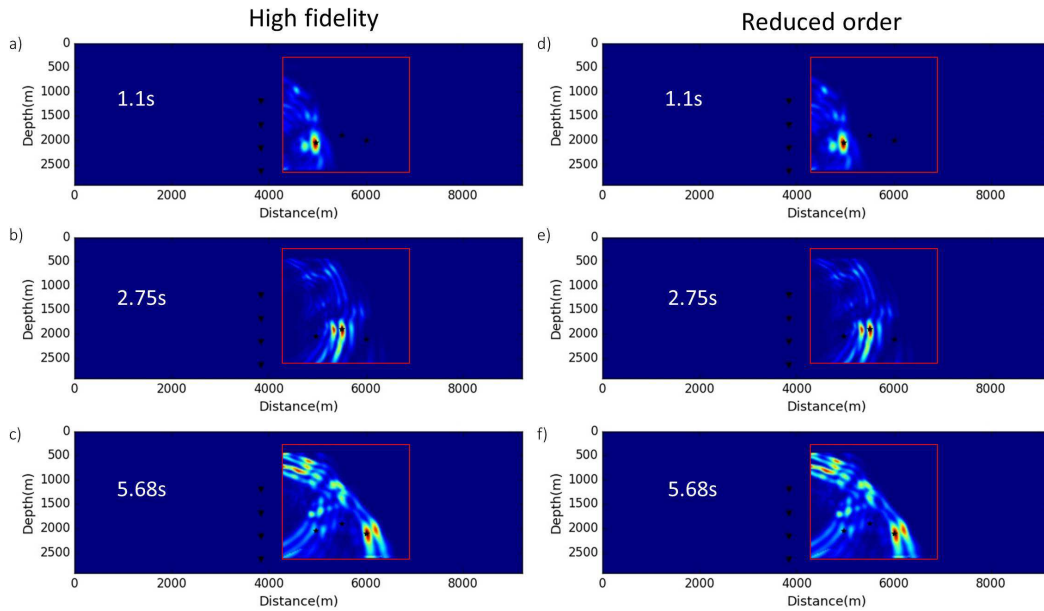
Figure 5.9: Snapshots of normalized energy flux map corresponding to the estimated origin time of three microseismic events. Left and right panels: energy flux maps corresponding to results from reduced-order and high-fidelity systems respectively. Top to bottom row: energy flux map corresponding to origin times of 1.1s, 2.75s and 5.68s. Triangles: Receivers. Stars: Microseismic events. Red box: Interested area, inside which wavefields are calculated. The snapshots are color coded. Warm color represents high energy whereas code color represents low energy.

tions in the real world, which is a small portion of a complete snapshot matrix $\boldsymbol{A}$. Conversely for fast forward modeling of waveforms due to sources at any possible position (Pereyra and Kaelin, 2008), a near-complete snapshot matrix is required. Whether it is desirable to apply the proposed method to a certain application depends on the online versus offline computation times as well as the computational resources available in the online stage.

Two characteristics of microseismic monitoring permit and encourage the creation of a reduced-order time-reversal extrapolation for real-time microseismic event localization, namely a limited number of receivers and long monitoring/recording time (usually from several hours to days). Borehole acquisitions typically use up to a dozen geophones, whereas surface acquisitions can be substantially larger (Duncan and Eisner, 2010; Van der Baan et al., 2013). Yet it is not required to simulate a source at every possible spatial position in depth, greatly reducing the number of simulations which eventually leads to a more interesting snapshot matrix $\boldsymbol{A}$. Combined with the long recording times, this ensures that the overall computational time of reduced-order time-reversal extrapolation, including both offline and online calculation, is much smaller than the time required when using a high-fidelity simulation system. Figure 5.10 shows a qualitative sketch of computation versus recording time. The starting computation time for reduced-order extrapolation (dash-dot line) is not zero because of offline training (dashed line) which could be more than direct high-fidelity extrapolation (solid line). The added computation time per reduced-order simulation is substantially smaller than that for the high-fidelity ones. Hence at some recording length the two approaches use the same total computation times and reduced-order extrapolation uses less computation time if recording time further increases.

To obtain both good performance and reasonable computation time, several items need to be addressed during the implementation of the proposed method for continuous time-reversal extrapolation. First, it is normally not necessary to include every time slice obtained from high fidelity simulations in snapshot matrix $\boldsymbol{A}$ as long as the time interval between selected two adjacent time slices satisfies the Nyquist sampling theorem. Second, the computation of the left orthonormal basis $\boldsymbol{Q}$ is controlled by the positive error tolerance ϵ. With a
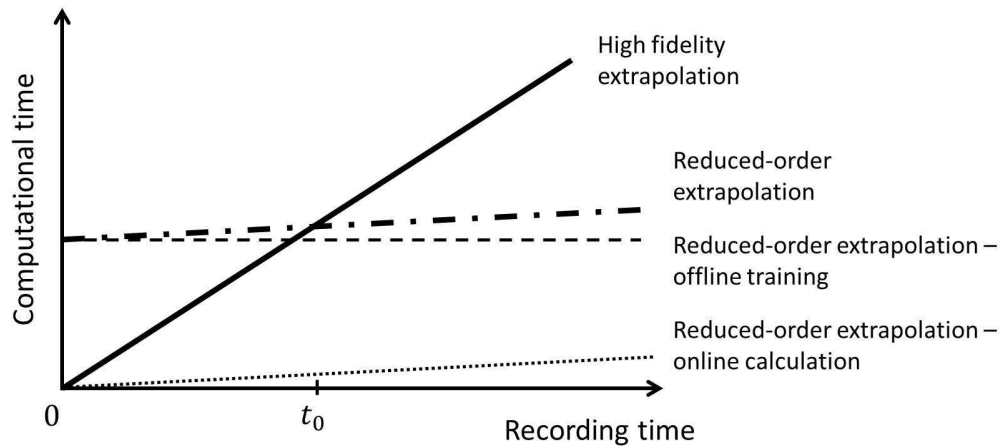
Figure 5.10: Sketch of computation versus recording time for high-fidelity and reduced-order extrapolations. Horizontal axis: recording time. Vertical axis: computational time. Both axes start from zero. Dotted line: online computational time increases slowly when using reduced-order extrapolation. Dashed line: computational time of offline training is constant with increasing recording time because simulation time for offline training is fixed. Dashed doted line: overall computational time of reduced order extrapolation is the sum of offline and online computational times. Solid line: computational time increases linearly with recording time. t_0: point when the overall computational time of reduced-order simulation become less than that of direct high-fidelity extrapolation.

lower error tolerance ϵ, the left orthonormal basis $\boldsymbol{Q}$ creates a more accurate but larger reduced-order system since it captures more information in snapshot matrix $\boldsymbol{A}$, whereas conversely, a higher error tolerance leads to a less accurate but smaller reduced-order system. Finally, real data should be divided into segments where the total time of each segment for online extrapolation is not longer than the simulation time T_H for offline training. Because no wavefield information at time over T_H is included neither in snapshot matrix $\boldsymbol{A}$ nor in the reduced-order system, the computation of coefficient vector $\boldsymbol{a}(t)$ becomes unstable when extrapolation time is longer than T_H.

5.6 Conclusion

Traditional simulation/extrapolation based on the two-wave wave equation is a high-fidelity but time-consuming process which has substantial information redundancy because discrete wavefields are similar within adjacent spatial grids and temporal slices. It also repeatedly solves the same simulation problem since only the recorded data change but the velocity field remains constant. Proper orthogonal decomposition is a promising technique to turn the high-fidelity simulation into a much smaller system by removing the redundancy, which can be used to build a fast time-reversal extrapolation scheme. A workflow using this new scheme is proposed, which may permit real-time waveform-based microseismic event localization using feasible computational resources in the field.

Chapter 6

Conclusions and suggested future research

6.1   Conclusions

In this research, we introduce rotational seismology to exploration geophysics in a systematic manner, including concepts and possible applications. Different from traditional seismology, rotational seismology is based on a combined analysis of both translational motions, such as particle displacements, velocities and/or accelerations and ground rotational for a better understanding of subsurface structures or passive source mechanisms, compared with the case when only a single type of data is analyzed. Rotational motion can provide information about the spatial gradient of translational motions which is normally not directly available in traditional seismic observations. We have seen some improvements to current techniques for both exploration and global geophysical purposes due to the involvement of spatial gradient information, which inspired us to extend the application to waveform based microseismic event localization.

Time-reversal extrapolation is one of the most popular waveform based techniques for microseismic event localization, where time-reversed recordings are injected into a medium and waveforms are expected to focus at source locations. However, we find that when using only the translational motions in the

back-propagation through a borehole array of receivers, ghost events appear on the back-propagated source images which introduce ambiguity in the selection of source locations. We propose two representation theorem based time reversal extrapolation schemes, namely acoustic and elastic, for microseismic event localization, which utilize both wavefields and their spatial gradients, provided by pressure wavefields and particle velocities in the acoustic case and particle velocities and rotational rate wavefields in the elastic case. I have shown that the proposed methods can provide better results with canceled ghost focuses and boosted energy concentrations, compared with the traditional time-reversal extrapolation of only the translational recordings.

We also propose two focusing criteria to automatically determine the locations and origin time of microseismic events, namely based on magnitude summation for acoustic case and energy flux based for elastic case. The proposed focusing criteria perform better over the traditional auto-correlation imaging condition since our proposed methods determine both the source locations and origin time during back-propagation without saving snapshots whereas the latter can only determine the source locations by saving the back-propagated snapshots followed by an application of the imaging condition.

The proposed methods are promising, but they still suffer from a high computational cost because they are two-way wave equation simulation based methods which requires to discretize a model with fine spatial and temporal grids for the purpose of computational stability. The discretization method normally has substantial information redundancy because the number of grid points is often larger than needed. We propose a proper orthogonal decomposition based workflow such that a smaller simulation system, known as a reduced-order simulation system, is built from a time-intensive offline training process. A fast extrapolation scheme based on the reduced-order system is then proposed for real-time microseismic event localization. We conclude that the method is suitable for continuous monitoring where the total computation time (offline and online) is shorter than that of traditional two-way wave equation based extrapolation.

133

6.2 Suggested future research

The research presented in this thesis can be extended to several directions.

Earthquake engineering Earthquake engineering studies the performance of structures and equipment during earthquakes, which is traditionally based on the analysis of only ground translational motion recordings and the corresponding seismic response spectra for a structure (Novak, 1974; Rayhani and Naggar, 2008). Teisseyre et al. (2006) suggests that current theory cannot explain the strong rotational motions recorded during an earthquake and the resulting failure of structures, indicating the necessity of taking into account ground rotational motions in seismic response analysis. Further research on the mechanisms of ground rotational motions and the corresponding structure responses is needed.

Source location inversion In this thesis, I suggest that the recordings of particle velocity and rotational rate should be combined through the elastic representation theorem based time-reversal extrapolation to obtain an improved source image by removing ghost focusing. One possible alternative is to use a least-square inversion scheme that incorporates both the wavefield and its spatial gradient, which may provide a source image with higher resolution compared with a time-reversal extrapolation scheme.

Two approaches can be used to build the cost functions, namely waveform inversion and Bayesian joint inversion. In the first approach, the elastic wave equations for an inhomogeneous medium should be modified to couple rotational motions, whereas in the second approach, rotational motions are treated as a priori constraints satisfying equations 2.2 or 2.3. By applying a sparsity constraint, a more focused source image should be obtained. Also further research is required to investigate the possibility of incorporating rotational motion in a moment tensor inversion scheme for better resolutions of both source locations and moment tensors.

General elastic representation theorem The derivation of the elastic representation theorem and the corresponding time-reversal extrapolation

scheme in this thesis is valid only in an isotropic homogeneous medium, even though examples in chapter 4 show that it works fine in an inhomogeneous medium. However, to understand the underlying physics, it is necessary to derive a general elastic representation theorem, which can account for both homogeneous and inhomogeneous cases.

Parametrized model order reduction   The offline training step in the tradition model order reduction scheme in this thesis requires fixed model parameters, such as a certain acquisition geometry and a pre-determined medium velocity model. Each time these parameters change, new offline training is needed to obtain the corresponding order-reduced model, making its application in seismic inverse problems extremely inefficient because those parameters, especially velocity models, are updated in each iteration.

A possible solution to the previous problem is parametrized model order reduction (pMOR), in which geometric and physical properties are parametrized so that a general order-reduced model can be used for various parameters (Sampath et al., 2009). Research needs to be done about how to apply this technique in seismology, when the degrees of freedom for those parameters are in the order of millions.

Bibliography

Ainslie, M., 2010, Principles of sonar performance modeling: Springer.

Aki, K., and P. Richards, 2002, Quantitative seismology: University Science Books.

Al-Anboori, A., V. d. B. M., and J.-M. Kendall, 2005, Approximate separation of pure-mode and converted waves in 3-c reflection seismics by tau-p transform: Geophysics, **70**, no. 3, V81–V86.

Aldridge, D. F., and R. E. Abbott, 2009, Investigating the point seismic array concept with seismic rotation measurements: Sandia National Lab Report.

Aldridge, D. F., L. C. Bartel, N. P. Symons, and N. R. Warpinski, 2003, Grid search algorithm for 3d seismic source location: SEG Technical Program Expanded Abstracts 2003, 730–733.

Allen, J. J., 2009, Micro-system inertial sensing technology overview: Sandia National Lab Report.

Artman, B., I. Podladtchikov, and B. Witten, 2010, Source location using time-reverse imaging: Geophysical Prospecting, **58**, 861–873.

Barak, O., S. Constable, K. Key, and S. Ronen, 2015, Acquiring seismic rotations with magnetometers: SEP Report, 49–76.

Barak, O., F. Herkenhoff, R. Dash, P. Jaiswal, J. Giles, S. de Ridder, R. Brune, and S. Ronen, 2014, Six-component seismic land data acquired with geophones and rotation sensors: Wave-mode selectivity by application of multi-component polarization filtering: The Leading Edge, **11**, 1224–1232.

Bath, M., 1979, Introduction to seismology 2nd edition: Birkhauser, Basel.

Baysal, E., D. D. Kosloff, and J. W. C. Sherwood, 1983, Reverse time migration: Geophysics, **48**, no. 11, 1514–1524.

Benner, P., S. Gugercin, and K. Willcox, 2015, A survey of projection-based

model reduction methods for parametric dynamical systems: SIAM Review, **57**, no. 4, 483–531.

Bernauer, F., F. Wassermann, J. Guattari, and H. Igel, 2016, Portable sensor technology for rotational ground motions: Astronomical Society of Pacific, 13345.

Bernauer, F., J. Wassermann, and H. Igel, 2012, Rotational sensors: a comparison of different sensor types: Journal of Seismology, **16**, no. 4, 595–602.

Bernauer, M., A. Fichtner, and H. Igel, 2009, Inferring earth structure from combined measurements of rotational and translational ground motions: Geophysics, **74**, no. 6, WCD41–WCD47.

———, 2014, Reducing nonuniqueness in finite source inversion using rotational ground motions: Journal of Geophysical Research: Solid Earth, **119**, no. 6, 4860–4875.

Brokevsova, J., J. Malek, and J. R. Evans, 2012, Note: Rotaphone, a new self-calibrated six-degree-of-freedom seismic sensor: Review of Science Instruments, **83**, no. 8, 086108.

Castellanos, F., and M. Van der Baan, 2013, Microseismic event locations using the double-difference algorithm: CSEG Recorder, **38**, no. 3, 26–37.

———, 2015, Waveform similarity for quality control of event locations, time picking and moment tensor solutions: Geophysics, **80**, no. 6, WC99–WC106.

Chambers, K., B. Dando, G. A. Jones, R. Velasco, and S. A. Wilson, 2014, Moment tensor migration imaging: Geophysical Prospecting, **62**, no. 4, 879–896.

Chambers, K., and J. Kendall, 2008, A practical implementation of wavefront construction for 3d isotropic media: Geophysical Journal International, **173**, no. 3, 1030–1038.

Chambers, K., J.-M. Kendall, S. Brandsberg-Dahl, and J. Rueda, 2010, Testing the ability of surface arrays to monitor microseismic activity: Geophysical Prospecting, **58**, no. 5, 821–830.

Chatterjee, A., 2000, An introduction to the proper orthogonal decomposition: Current Science, Special Section: Computer Science, **78**, no. 7, 808–817.

Cheng, J., and M. Sacchi, 2015, A fast rank-reduction algorithm for 3d deblending via randomized QR decomposition: SEG Technical Program Expanded

Abstracts 2015, 3830–3835.

Cochard, A., H. Igel, B. Schuberth, W. Suryanto, A. Velikoseltsev, U. Schreiber, J. Wassermann, F. Scherbaum, and D. Vollmer, 2006, Rotational motions in seismology: theory, observation, simulation, earthquake source asymmetry: Structural media and rotation effects: Springer.

Crampin, S., 1981, A review of wave motion in anisotropic and cracked elastic media: Wave Motion, **3**, no. 4, 343–391.

Curtis, A., and D. Halliday, 2010, Source-receiver wave field interferometry: Physical Review E, **81**, no. 4, 046601–1–046601–10.

D'ALessandro, A., and G. A'Anna, 2014, Retrieval of ocean bottom and downhole seismic sensors orientation using integrated mems gyroscope and direct rotation measurements: Advances in Geosciences, **40**, 11–17.

D'ALessandro, A., D. Luzio, and G. A'Anna, 2014, Urban mems based seismic network for post-earthquakes rapid disaster assessment: Advances in Geosciences, **40**, 1–9.

Dayley, T. M., R. Gritto, E. L. Majer, and P. West, 2003, Tube-wave suppression in single-well seismic acquisition: Geophysics, **68**, no. 3, 863–869.

De Hoop, A. T., 1988, Time-domain reciprocity theorems for acoustic wave fields in fluids with relaxation: The Journal of the Acoustical Society of America, **84**, no. 5, 1877–1882.

De Meersman, K., M. Van der Baan, and J.-M. Kendall, 2006, Signal extraction and automated polarisation analysis of multi-component array data: Bulletin of the Seismological Society of America, **96**, no. 6, 2415–2430.

Donner, S., M. Bernauer, and H. Igel, 2016, Inversion for seismic moment tensors combining translational and rotational ground motions: Geophysical Journal International, **207**, no. 1, 562–570.

Duncan, P. M., and L. Eisner, 2010, Reservoir characterization using surface microseismic monitoring: Geophysics, **75**, no. 5, 75A139–75A146.

Duncan, P. M., J. D. Lakings, and R. A. Flores, 2008, Method for passive seismic emission tomography: U. S. Patent Application Publication US2008/0068928A1.

Dunn, R. W., H. H. Mahdi, and H. J. Al-Shukri, 2009, Design of a relatively inexpensive ring laser seismic detector: Bulletin of the Seismological Society

of America, **99**, no. 2B, 1437–1442.

Eaton, D. W., M. Van der Baan, B. Birkelo, and J.-B. Tary, 2014, Scaling relations and spectral characteristics of tensile microseisms: Evidence for opening/closing cracks during hydraulic fracturing: Geophysical Journal International, **196**, no. 3, 1844–1857.

Edme, P., M. Daly, E. Muyzert, and E. Kragh, 2013, Side scattered noise attenuation using rotation data: 75th EAGE Conference and Exhibition incorporating SPE EUROPEC 2013, Extended abstract, 1–4.

Edme, P., and E. Muyzert, 2013, Rotational data measurement: 75th EAGE Conference and Exhibition incorporating SPE EUROPEC 2013, Extended abstract, 1–4.

———, 2014, Efficient land seismic acquisition sampling using rotational data: 76th EAGE Conference and Exhibition, Extended abstract, 1–4.

Egorov, E. V., I. V. Egorov, and V. M. Agafonov, 2015, Self-noise of the met angular motion seismic sensors: Journal of Sensors, 1–5.

Eyre, T. S., and M. Van der Baan, 2015, Overview of moment-tensor inversion of microseismic event: the Leading Edge, Special Section: Microseismic Source Machanisms, 882–888.

Fehler, M., 2008, Earthquake localization in handbook of signal processing in acoustics: Springer New York.

Feroz, A., and M. Van der Baan, 2013, Uncertainties in microseismic event locations for horizontal, vertical and deviated boreholes: SEG Technical Program Expanded Abstracts 2013, 592–596.

Fink, M., D. Cassereau, A. Derode, C. Prada, P. Roux, M. Tanter, J. L. Thomas, and F. Wu, 2000, Time-reversed acoustics: Reports on Progress in Physics, **63**, no. 12, 1933–1995.

Fleury, C., and I. Vasconcelos, 2013, Adjoint-state reverse time migration of 4C data: Finite-frequency map migration for marine seismic imaging: Geophysics, **78**, no. 2, WA159–WA172.

Ganzales, O., and A. M. Stuart, 2008, A first course in continuum mechanics: Cambridge University Press.

Gao, J., M. Sacchi, and X. Chen, 2011, A fast rank reduction method for the reconstruction of 5d seismic volumes: SEG Technical Program Expanded

Abstracts 2011, 3622–3627.

Gola, A., E. Chiesa, E. Lasalandra, F. Pasolini, M. Tronconi, T. Ungaretti, and A. Baschirotto, 2003, Interface for mems-based rotational accelerometer for hdd applications with 2.5 rad/s2 resolution and digital output: IEEE Sensors Journal, **3**, 383–392.

Graizer, V. M., 2005, Effect of tilt on strong motion data processing: Soil Dynamic and Earthquake Engineering, **25**, no. 3, 197–204.

Grekova, E. F., 2012, Nonlinear isotropic elastic reduced cosserat continuum as a possible model for geomedium and geomaterials; spherical prestressed state in a semilinear material: Journal of Seismology, **16**, no. 4, 695–707.

Grekova, E. F., M. A. Kulesh, and G. C. Herman, 2009, Waves in linear elastic media with microrotations, part 2: Isotropic reduced cosserat model: Bulletin of the Seismological Society of America, **99**, no. 2B, 1423–1428.

Halko, N., P. Martinsson, and J. A. Tropp, 2010, Finding structure with randomness: Probabilistic algorithms for constructing approximate matrix decomposition: SIAM Review, Survey and Review section, **53**, no. 2, 217–288.

Huang, B. S., 2003, Ground rotational motions of the 1991 chi–chi, taiwan eqrthquake as inferred from dense array observations: Geophysical Research Letters, **30**, no. 6, 1307–1310.

Igel, H., M. Bernauer, J. Wassermann, and K. U. Schreiber, 2015, Seismology, rotational, complexity: Encyclopedia of complexity and systems science: Springer Science and Business Media New York.

Igel, H., A. Cochard, J. Wassermann, A. Flaws, U. Schreiber, A. Velikoseltsev, and N. P. Dinh, 2007, Broad-band observations of earthquake-induced rotaional ground motions: Geophysical Journal International, **168**, no. 1, 182–196.

Igel, H., U. Schreiber, A. Flaws, B. Schuberth, A. Velikoseltsev, and A. Cochard, 2005, Rotational motions induced by the m8.1 tokachi-oki earthquake, september 25, 2003: Geophysical Research Letters, **32**, no. 8, L08309–1–L08309–5.

Jaroszewicz, L. R., Z. Krajewski, and K. P. Tesseyre, 2012, Usefulness of AFORS - autonomous fiber-optic rotational seismograph for investigation of rotational phenomena: Journal of Seismology, **16**, no. 4, 573–586.

Jost, M. L., and R. B. Herrmann, 1989, A student's guide to and review of moment tensors: Seismological Research Letters, **60**, no. 2, 37–57.

Kappler, K., N. Cuevas, and J. W. Rector, 2006, Response of induction coil magnetometers to perturbations in orientation: SEG Technical Program Expanded Abstracts 2006, 899–903.

Knopoff, L., 1956, Diffraction of elastic waves: The Journal of the Acoustical Society of America, **28**, no. 2, 217–229.

Knopoff, L., and A. Gangi, 1959, Seismic reciprocity: Geophysics, **24**, no. 4, 681–691.

Kocon, K., and M. Van der Baan, 2012, Quality assessment of microseismic event locations and traveltime picks using a multiplet analysis: The Leading Edge, **31**, no. 11, 1330–1337.

Kozlov, V., V. Agafonov, and J. Bindler, 2006, Small, low-power, low-cost imu for personal navigation and stabilization systems: Proceedings of the 2006 National Technical Meeting of The Institute of Navigation, Monterey, CA, 650–655.

Kulesh, M., 2009, Waves in linear elastic media with microrotations, part 1: Isotropic full cosserat model: Bulletin of the Seismological Society of America, **99**, no. 2B, 1416–1422.

Kurzych, A., L. R. Jaroszewicz, Z. Krajewski, K. P. Teisseyre, and J. K. Kowalski, 2014, Fibre optic system for monitoring rotational seismic phenomena: Sensors, **14**, no. 3, 5459–5469.

Lakes, R., 1995, Experimental methods for study of cosserat elastic solids and other generalized elastic continua: M*ü*hlhaus, h., ed., continuum models for materials with micro-structure: Wiley, New York.

Lassila, T., A. Manzoni, A. Quarteroni, and G. Rozza, 2013, A reduced computational and geometrical framework for inverse problems in hemodynamics: International Journal for Numerical Methods in Biomedical Engineering, **29**, no. 7, 741–776.

Lee, W. H. K., J. R. Evans, B. S. Huang, C. R. Hutt, C. J. Lin, C. C. Liu, and R. L. Nigbor, 2012, Measuring rotational ground motions in seismological practice: New Manual of Seismological Observatory Practice 2 (NMSOP-2), 1–27.

Lee, W. H. K., B. S. Huang, C. A. Langston, C. J. Lin, C. C. Liu, T. C. Shin, T. L. Teng, and C. F. Wu, 2009a, Review: Progress in rotational ground-motion observations from explosions and local earthquake in taiwan: Bulletin of the Seismological Society of America, **99**, no. 2B, 958–967.

Lee, W. H. K., H. Igel, and M. D. Trifunac, 2009b, Recent advances in rotational seismology: Seismological Research Letter, **80**, no. 3, 479–490.

Li, M., B. H. Kim, and A. Mourikis, 2013, Real-time motion tracking on a cellphone using inertial sensing and a rolling-shutter camera: Proceedings - IEEE International Conference on Robotics and Automation, Expanded Abstract, 4712–4719.

Li, Z., and M. Van der Baan, 2014, Acoustic representation theorem based time-reversal-extrapolation for microseismic event localization: SEG Technical Program Expanded Abstracts 2014, 2240–2244.

——, 2015, Enhanced microseismic event localization by reverse time extrapolation: SEG Technical Program Expanded Abstracts 2015, 4111–4115.

Li, Z. H., and M. Van der Baan, 2016, Microseismic event localization by acoustic time reversal extrapolation: Geophysics, **81**, no. 3, KS123–KS134.

——, 2017, Elastic passive source localization using rotational motion: Geophysical Journal International accepted.

Lieu, T., C. Farhat, and M. Lesoinne, 2006, Reduced-order fluid/structure modeling of a complete aircraft configuration: Computer Methods in Applied Mechanics and Engineering, **195**, no. 41-43, 5730–5742.

Lin, C. J., H. P. Huang, N. D. Pham, C. C. Liu, W. C. Chi, and W. H. K. Lee, 2011, Rotational motions for teleseismic surface waves: Geophysical Research Letter, **38**, no. 15, L15310–1–L15310–5.

Lin, C. J., W. G. Huang, H. P. Huang, B. S. Huang, C. S. Ku, and C. C. Liu, 2012, Investigation of array-derived rotation in taipei 101: Journal of Seismology, **16**, no. 4, 721–731.

Linden, D. A., 1959, A discussion of sampling theorems: Proceeding of the IRE, **47**, no. 7, 1219–1226.

Lucia, D. J., P. S. Beran, and W. A. Silva, 2004, Reduced-order modelling: new approaches for computational physics: Progress in Aerospace Sciences, **40**, no. 1-2, 51–117.

Maxwell, S., 2009, Assessing the impact of microseismic location uncertainties on interpreted fracture geometries: 2009 SPE Annual Technical Conference and Exhibition, SPE125121–1–SPE125121–13.

McKeighen, R. E., 1998, Design guidelines for medical ultrasonic arrays: Proceeding SPIE 3341, Medical Imaging 1998: Ultrasonic Transducer Engineering, **3314**, no. 2, 1–17.

Mcleod, D. P., G. E. Stedman, T. H. Webb, and U. Schreiber, 1998, Comparison of standard and ring laser rotational seismograms: Bulletin of the Seismological Society of America, **88**, no. 6, 1495–1503.

McMechan, G. A., 1983, Migration by extrapolation of time-dependent boundary values: Geophysical Prospecting, **31**, no. 3, 413–420.

———, 1985, Imaging of earthquake sources in long valley valdera, california, 1983: Bulletin of the Seismological Society of America, **75**, no. 4, 1005–1020.

Mizuno, J., K. Nottmeyer, T. Kobayashi, K. Minami, and M. Esashi, 1999, Silicon bulk micromachined crash detection sensor with simultanious angular and linear sensitivity: IEEE Transducers, 1302–1305.

Mora, C. B., 2002, Marmousi synthetic dataset: Stanford Exploration Project, Report DATALIB, 1–10.

Muyzert, E., A. Kashubin, E. Kragh, and P. Edme, 2012, Land seismic data acquisition using rotation sensors: 74th EAGE Conference & Exhibition incorporating SPE EUROPEC 2012, 1–5.

Nigbor, R. L., J. R. Evans, and C. R. Hutt, 2009, Laboratory and field testing of commercial rotational seismometers: Bulletin of the Seismological Society of America, **99**, no. 2B, 1215–1227.

Novak, M., 1974, Effect of soil on structural response to wind and earthquake: Earthquake Engineering and Structural Dynamics, **3**, no. 1, 79–96.

Oropeza, V., and M. D. Sacchi, 2011, Simultaneous seismic data denoising and reconstruction via multichanel singular spectrum analysis: Geophysics, **76**, no. 3, V25–V32.

Pancha, A., T. H. Webb, G. E. Stedman, D. P. McLeod, and K. U. Schreiber, 2000, Ring laser detection of rotations from teleseismic waves: Geophysical Research Letters, **27**, no. 21, 3553–3556.

Pereyra, V., and B. Kaelin, 2008, Fast wave propagation by model order re-

duction: Electronic Transactions on Numetical Analysis, **30**, 406–419.

Pham, N. D., H. Igel, J. de la Puente, M. Kaser, and M. A. Schoenberg, 2010, Rotational motions in homogeneous anisotropic elastic media: Geophysics, **75**, no. 5, D47–D56.

Pham, N. D., H. Igel, J. Wassermann, M. Kaser, J. de la Puente, and U. Schreiber, 2009, Observations and modeling of rotational signals in the p coda: constraints on crustal scattering: Bulletin of the Seismological Society of America, **99**, no. 2B, 1315–1332.

Pierson, R., D. Laughlin, and R. Brune, 2016, Advances in rotational seismic measurements: SEG Technical Program Expanded Abstracts 2016, 2263–2267.

Pitarka, A., 1999, 3D elastic finite-difference modeling of seismic motion using staggered grids with nonuniform spacing: Bulletin of the Seismological Society of America, **89**, no. 1, 54–68.

Projetti, M., O. Vancouwenberghe, H. Paulson, N. Goujon, F. Marty, and D. Aubry, 2014, Development of a MEMS rotation sensor for oilfield applications: Sensors, IEEE, 1–4.

Pujol, J., 2009, Tutorial on rotations in the theories of finite deformation and micropolar (cosserat) elasticity: Bulletin of the Seismological Society of America, **99**, no. 2B, 1011–1027.

Ravasi, M., and A. Curtis, 2013, Elastic imaging with exact wavefield extrapolation for application to ocean-bottom 4C seismic data: Geophysics, **78**, no. 6, S265–S284.

Rayhani, M. H., and M. H. Naggar, 2008, Numerical modelling of seismic response of rigid foundation on soft soil: International Journal of Geomechanics, **8**, no. 6, 336–346.

Reinwald, M., M. Bernauer, H. Igel, and S. Donner, 2016, Improved finite-source inversion through joint measurements of rotational and translational ground motions: a numerical study: Solid Earth, **7**, 1467–1477.

Richter, C. F., 1958, Elementary seismology: W. H. Freeman, San Francisco, California.

Sampath, M. K., A. Dounavis, and R. Khazaka, 2009, Parametrized model order reduction techniques for FEM based full wave analysis: IEEE Trans-

actions on Advanced Packaging, **32**, no. 1, 1–11.

Sartori, A., D. Baroli, A. Cammi, L. L., and G. Rozza, 2014, A reduced order model for multi-group time-dependent parametrized reactor spatial kinetics: Proceedings of the 2014 22nd International Conference on Nuclear Engineering (ICONE22), Prague, Czech Republic, ASME, 2014, 30707.

Schalkwijk, K., W. C.P.A., and D. J. Verschuur, 1999, Applicatio of two-step decomposition to multicomponent ocean-bottom data: Theory and case study: Journal of Seismic Exploration, **8**, no. 3, 261–278.

——, 2003, Adaptive decomposition of multicomponent ocean-bottom seismic data into downgoing and upgoing p- and s-waves: Geophysics, **68**, no. 3, 1091–1102.

Schilders, W., 2008, Introduction to model order reduction in model order reduction: Theory, research aspects and applications: Mathematics in Industry, **13**, 3–32.

Schreiber, K. U., J. N. Hautmann, A. Velikoseltsev, J. Wassermann, H. Igel, J. Otero, F. Vernon, and J.-P. R. Wells, 2009a, Ring laser measurements of ground rotations for seismology: Bulletin of the Seismological Society of America, **99**, no. 2B, 1109–1198.

Schreiber, K. U., G. E. Stedman, H. Igel, and A. Flaws, 2006, Ring laser gyroscopes as rotation sensors for seismic wave studies, in eqrthquake sourse asymmetry, structural media and rotation effects, r. teisseyre, m. takeo and e. majewski(editors): Springer New York.

Schreiber, K. U., A. Velikoseltsev, A. J. Carr, and R. Franco-Anaya, 2009b, The application of fiber optic gyroscope for the measurement of rotations in structural engineering: Bulletin of the Seismological Society of America, **99**, no. 2B, 1207–1214.

Schuster, G. T., J. Yu, J. Sheng, and J. Rickett, 2004, Interferometric/daylight seismic imaging: Geophysical Journal International, **157**, no. 2, 838–852.

Shearer, P. M., 2009, Introduction to seismology: Cambridge University Press.

Snieder, R., 2004, Extracting the green's function from the correlation of coda waves: A derivation based on stationary phase: Physics Review E, **69**, no. 4, 046610–1–046610–8.

Snieder, R., K. Wapenaar, and K. Larner, 2006, Spurious multiples in seismic

interferometry of primaries: Geophysics, **71**, no. 4, SI111–SI124.

Spudich, P., S. L. K., M. Hellweg, J. B. Fletcher, and L. M. Baker, 1995, Transient stresses at parkfield, california, produced by the m7.4 landers earthquake of june 28, 1992: Observations from the upsar dense seismograph array: Journal of Geophysical Research, **100**, no. B1, 675–690.

Stern, R. J., 2002, Subduction zones: Reviews of Geophysics, **40**, no. 4, 3–1–3–38.

Strang, G., 2006, Linear algebra and its applications, fourth edition: Cengage Learning.

Suryanto, W., J. Wassermann, H. Igel, A. Cochard, D. Vollmer, F. Scherbaum, A. Velikoseltsev, and U. Schreiber, 2006, First comparison of seismic array derived rotations with direct ring laser measurements of rotational ground motion: Bulletin of the Seismological Society of America, **96**, no. 6, 2059–2071.

Synge, J., 1995, Flux of energy for elastic waves in anisotropic media: Proceedings of the Royal Irish Academy: Section A, Mathematical and Physcial Sciences, **58**, 12–21.

Takeo, M., 1998, Ground rotational motions recorded in near-source region of earthquakes: Geophysical Research Letter, **25**, no. 6, 789–792.

Takeo, M., and H. M. Ito, 1997, What can be learned from rotational motions excited by earthquakes: Geophysical Journal International, **129**, no. 2, 319–329.

Tarantola, A., 1984, Inversion of seismic reflection data in the acoustic approximation: Geophysics, **49**, no. 8, 1259–1266.

Teisseyre, R., M. Takeo, and E. Majewski, 2006, Earthquake source asymmetry, structure media and rotation effects: Springer.

Thomsen, L., 1986, Weak elastic anisotropy: Geophysics, **51**, no. 10, 1954–1966.

Tromp, J., C. Tape, and Q. Liu, 2005, Seismic tomography, adjoint methods, time reversal and banana-doughnut kernels: Geophysical Journal International, **160**, no. 1, 195–216.

Vaezi, Y., and M. Van der Baam, 2015, Interferometric assessment of clamping quality of borehole geophones: Geophysics, **80**, no. 6, WC89–WC98.

Van der Baan, M., D. Eaton, and M. Dusseault, 2013, Microseismic monitoring developments in hydraulic fracture stimulation: in Bunger A. P., J. McLennan and R. Jeffrey, eds., Effective and sustainable hydraulic fracturing, Intech, 439–466.

Van Driel, M., J. Wassermann, M. F. Nader, B. S. A. Schuberth, and H. Igel, 2012, Strain rotation coupling and its implications on the measurement of rotational ground motions: Journal of Seismology, **16**, no. 4, 657–668.

Van Manen, D.-J., A. Curtis, and J. O. A. Robertsson, 2006, Interferometric modeling of wave propagation in inhomogeneous elastic media using time reversal and reciprocity: Geophysics, **71**, no. 4, SI47–SI60.

Vasconcelos, I., 2013, Source-receiver, reverse-time imaging of dual-source, vector-acoustic seismic data: Geophysics, **78**, no. 2, WA123–WA145.

Vassallo, M., A. Ozbek, K. Ozdemir, and K. Eggenberger, 2010, Crossline wavefield reconstruction from multicomponent streamer data: Part 1 - multichannel interpolation by matching pursuit (mimap) using pressure and its crossline gradient: Geophysics, **75**, no. 6, WB53–WB67.

Velikoseltsev, A., K. U. Schreiber, A. Yankovsky, J. R. Wells, A. Boronachin, and A. Tkachenko, 2012, On the application of fiber optic gyroscopes for detection of seismic rotations: Journal of Seismology, **16**, no. 4, 623–637.

Versteeg, R., and G. Grau, 1990, Practical aspects of seismic data inversion, the marmousi experience practical aspects of seismic data inversion, the marmousi experience: Europe Association of Exploration Geophysicist, Proceedings of 1990 EAEG Workshop, 52nd EAEG Meeting, 1–194.

——, 1991, Eage workshop report: Practical aspects of seismic data inversion: First Break, **9**, no. 2, 75–80.

Wapenaar, C., and G. Haime, 1990, Elastic extrapolation of primary seismic p- and s-waves: Geophysical Prospecting, **38**, no. 1, 23–60.

Wapenaar, K., D. Draganov, J. Van der Neut, and J. Thorbecke, 2004, Seismic interferometry: a comparison of approaches: SEG Technical Program Expanded Abstracts 2004, 2269–2272.

Wapenaar, K., and J. Fokkema, 2006, Green's function representations for seismic interferometry: Geophysics, **71**, no. 4, S133–S146.

Wassermann, J., S. Lehndorfer, H. Igel, and U. Schreiber, 2009, Performance

test of a commercial rotational motion sensor: Bulletin of the Seismological Society of America, **99**, no. 2B, 1449–1456.

Whitmore, D. N., 1983, Iterative depth imaging by back time propagation: SEG Technical Program Expanded Abstracts 1983, 382–385.

Wu, C., D. Bevc, and V. Pereyra, 2013, Model order reduction for efficient seismic modelling: SEG Technical Program Expanded Abstracts 2013, 3360–3364.

Yip, R. K. K., P. K. S. Tam, and D. N. K. Leung, 1992, Modification of hough transform for circles and ellipses detection using a 2-dimensional array: Pattern recognition, **25**, no. 9, 1007–1022.

Zaitsev, D., V. Agafonov, E. Egorov, A. Antonov, and A. Shabalina, 2015, Molecular electronic angular motion transducer broad band self-noise: Sensors, **15**, no. 11, 29378–29392.

Zeng, Y. Q., and Q. H. Liu, 2001, A staggered-grid finite-difference method with perfectly matched layers for poroelastic wave equations: the Journal of the Acoustic Society of America, **109**, no. 6, 2571–2580.

Zhang, H., and C. H. Thurber, 2003, Double-difference tomography: The method and its application to the hayward fault, california: Bulletin of the Seismological Society of America, **93**, no. 5, 1875–1889.